UNIWERSYTET ŚLĄSKI

Institute of Physics

Faculty of Science and Technology

Doctoral Thesis

Plastic scintillator applications in quality assurance of small dynamic fields in radiotherapy

Grzegorz Woźniak

Supervisor: dr hab. Beata Kozłowska

Chorzów, 2024

ACKNOWLEDGEMENTS

Dziękuję Pani promotor ***dr hab. Beacie Kozłowskiej****,*
za wieloletnią współpracę, przekazaną wiedzę merytoryczną, nieocenioną pomoc,
życzliwość i wsparcie w trakcie wykonywania pracy.

Dziękuję ***dr Alicji Surowiec*** *za udostępnienie materiałów do badań.*

Podziękowania dla ***dr Marka Szewczuka***
z Katowickiego Centrum Onkologii
za cenne uwagi i udzieloną pomoc.

Dziękuję także wszystkim ***Koleżankom i Kolegom***
z Katowickiego Centrum Onkologii
za wszelką pomoc merytoryczną, życzliwość i motywację.

Szczególne podziękowania dla ***dr Marcina Dybka***
za udostępnienie zasobów i kontaktów niezbędnych w trakcie badań.

Praca z pewnością nigdy by nie powstała, gdyby nie moja ukochana małżonka ***Kasia.***
Dziękuję Ci za wielogodzinne dyskusje i analizy, silną motywację oraz
za nieskończone pokłady cierpliwości i wyrozumiałości
zwłaszcza przy podziale obowiązków w opiece nad naszym synem – ***Wojtkiem.***
Dziękuję Ci z całego serca!

Dziękuję całej mojej ***Rodzinie*** *za wsparcie i wiarę.*

ABSTRACT

New advanced radiotherapy techniques have been delivering increasingly higher doses to volumes with smaller margins. This involves the use of higher fractional doses delivered by dynamic techniques such as VMAT or IMRT which are realised by a sequence of small fields. However, these techniques pose challenges in patient-specific quality assurance, PSQA. Radiochromic films are commonly used for planar dosimetry and high-resolution active detector matrices, but both have some drawbacks.

The main objective of the doctoral thesis was to explore the use of plastic scintillators for PSQA in radiotherapy for small dynamic high-dose fields. The objectives included characterising plastic scintillators, investigating the optimum parameters of an affordable CMOS camera as a readout system, and developing post-processing methods. The designed measurement system consisted of the following elements: a custom phantom, a plastic scintillation detector, a CMOS camera, and developed MATLAB scripts.

The research was conducted in several stages. In the first step, thorough studies allowed the characterisation of the main component of the system as a radiation detector. The plastic scintillation detector, PSD, demonstrated potential as a reliable tool for radiotherapy dosimetry with its performance consistent with publications. As a result, a custom phantom was designed and manufactured for PSQA with the previously investigated components. In the second step, a novel system for small dynamic fields planar dosimetry based on plastic scintillator material and a high-resolution CMOS camera was developed. The study presented the comprehensive analysis of designed and manufactured PSD system for radiotherapy dosimetry, comparing it with Gafchromic EBT-3 films and the SunNuclear SRS MapCHECK active detector matrix.

Statistical analysis of Gamma Index, GI, results showed that the developed PSD system yields values that are comparable to the reference methods for a GI tolerance limit of 90%. For a tolerance limit of 95%, results were aligned with results from SRS MapCHECK. GI histogram analysis showed that, in general, the GI distribution for examined fields was lower than that from other methods. Despite this, the outcome of the PSD system was free from potentially false-positive results.

The discussion of obtained results includes potential system enhancements, such as improving spatial resolution and decreasing noise by using a high-end CMOS sensor or enhancing the readout system for immediate image analysis. The objectives of the study were achieved. The developed plastic scintillator-based PSQA system demonstrated comparable results with commonly used methods. The promising results suggested considering the use of the developed system in everyday practice at the Katowice Oncology Centre and indicated the possible further development of the system.

STRESZCZENIE

Nowoczesne techniki radioterapii pozwalają na dostarczanie coraz wyższych dawek do obszarów o mniejszych marginesach. Najczęściej realizowane są one za pomocą technik dynamicznych, takich jak VMAT czy IMRT. Stawia to nowe wyzwania w zakresie indywidualnej kontroli jakości planów leczenia pacjenta (PSQA). Do dozymetrii planarnej małych pól powszechnie stosuje się filmy radiologiczne i matryce aktywnych detektorów o wysokiej rozdzielczości, jednak każda z tych metod ma swoje ograniczenia.

Głównym celem pracy doktorskiej było zbadanie możliwości zastosowania scyntylatorów plastikowych do kontroli jakości planów leczenia dla niewielkich obszarów w technikach dynamicznych. Badania obejmowały charakteryzację scyntylatorów plastikowych, badanie optymalnych parametrów komercyjnej kamery CMOS jako systemu odczytu oraz rozwijanie metod przetwarzania danych. Opracowany system pomiarowy składał się z następujących elementów: fantom, plastikowy scyntylator, kamera CMOS, układ sterujący oraz opracowane skrypty MATLAB.

Praca była przeprowadzona w kilku etapach. W pierwszym, dogłębne badania pozwoliły na charakterystykę systemu jako detektora promieniowania. Plastikowy detektor scyntylacyjny (PSD) wykazał potencjał jako niezawodne narzędzie do dozymetrii radioterapii. W rezultacie, zaprojektowano i wyprodukowano fantom do PSQA z wcześniej zbadanymi komponentami. W drugim etapie opracowano i zbudowano fantom do weryfikacji małych dynamicznych pól oparty na wcześniej badanych komponentach. Praca przedstawiła kompleksową analizę opracowanego systemu PSD do dozymetrii radioterapii, porównując go z filmami Gafchromic EBT-3 i systemem SunNuclear SRS MapCHECK.

Analiza statystyczna wyników Gamma Index (GI) pokazała, że opracowany system PSD daje wartości porównywalne z metodami referencyjnymi dla limitu tolerancji 90% oraz zgodne z wynikami z SRS MapCHECK dla limitu 95%. Analiza histogramu GI pokazała, że dystrybuanta wartości indeksu gamma dla badanych pól była wyższa niż dla innych metod. Pomimo tego, wynik systemu PSD był wolny od potencjalnie fałszywie dodatnich wyników.

Dyskusja nad uzyskanymi wynikami objęła potencjalne ulepszenia systemu, takie jak poprawa rozdzielczości przestrzennej i zmniejszenie szumów poprzez użycie sensora CMOS wyższej klasy lub ulepszenie systemu odczytu do natychmiastowej analizy obrazu.

TABLE OF CONTENTS

ACKNOWLEDGEMENTS iii

ABSTRACT v

STRESZCZENIE vii

Table of Contents ix

LIST OF TABLES xi

LIST OF FIGURES xiii

LIST OF ABBREVIATIONS xvi

1 Introduction 1

2 Objectives and Outline 5

3 Theory 6

3.1 Principles of radiotherapy 6

3.2 Physics and characteristics of conventional medical accelerator photon beam 8

3.3 Medical linear accelerator 12

3.4 IMRT and VMAT Techniques 16

3.5 Dosimetry 17

3.6 Planar dosimetry in radiotherapy 19

3.7 The treatment planning system 21

3.8 A Patient-Specific Quality Assurance 22

3.9 Gamma index 24

3.10 Plastic scintillators 26

3.11 Dosimetric characteristics of organic scintillators 33

3.12 CMOS light detectors 39

4 Materials and Methods 43

4.1 Plastic scintillator 43

4.2 Camera 44

4.3 Scintillator image processing 45
4.4 Preliminary tests 46
4.5 Phantom 50
4.6 Experimental set-up 54
4.7 Radiochromic films 56
4.8 SRS Matrix 59
4.9 Patients selection 62
4.10 Plan Quality Assurance in TPS 63
4.11 Gamma index 64
4.12 Statistical analysis 64
5 Results 67
5.1 Preliminary results 67
5.2 Number of analysed points 75
5.3 TPS vs. plastic scintillator 76
5.4 TPS vs. SRS matrix 78
5.5 TPS vs. radiochromic films 81
5.6 Outliers analysis 83
5.7 GI normal distribution verification 84
5.8 Inter method result comparison 86
5.9 GI distribution analysis 89
5.10 Potential false positive results 90
5.11 Gamma histogram analysis 91
5.12 Cost of experimental set-up 93
6 Discussion 96
7 Conclusions 104
8 References 105

LIST OF TABLES

Table 1 Gafchromic EBT-3 Film selected properties. 20

Table 2 Pentax K-x CMOS sensor physical properties [104] [105]..... 44

Table 3: Cases selected for verification. Maximum dose, area and field size are calculated in TPS at a plastic scintillator plane: SSD 98 cm and depth 2 cm. For beam size calculation threshold 10% of a maximum dose was applied. 62

Table 4 Camera ISO, the measured signal, the signal converted to the dose [cGy] and calculated ISO correction factor [108]..... 73

Table 5 MTF [mm] for a film and PSD 75

Table 6 Gamma index analysis for plastic scintillator. Different DD and DTA were tested. Threshold was set to 10%..... 77

Table 7 Gamma index analysis summary for plastic scintillator for different passing rates. .. 78

Table 8 General statistics for different gamma results for plastic scintillator. Both parametric and nonparametric statistics are presented. Q25 and Q75 stands for quantile 0.25 and 0.75 respectively..... 78

Table 9 Gamma index analyses for SunNuclear SRSMapCHECK. Different DD and DTA were tested. The threshold was set to 10%. 79

Table 10 Gamma index analysis summary for SunNuclear SRS MapCHECK for different passing rates. 80

Table 11 General statistics for different gamma results for SRS MapCHECK. Both parametric and nonparametric statistics are presented. Q25 and Q75 stands for quantile 0.25 and 0.75 respectively..... 80

Table 12 Reported by Stedem et al. [118] SRS MapCHECK median performance depended on target volume [118] 80

Table 13 Gamma index analysis for Gafchromic ETB3. Different DD and DTA were tested. The threshold was set to 10%..... 81

Table 14 Gamma index analysis summary for Gafchromic EBT-3 films for different passing rates. 82

Table 15 General statistics for different gamma results for EBT-3 films. Both parametric and nonparametric statistics are presented. Q25 and Q75 stands for quantile 0.25 and 0.75 respectively. 82

Table 16 Test of normality for gamma results for EBT-3 films. 84

Table 17 Test of normality for gamma results for SRS MapCHECK. 84

Table 18 Test of normality for gamma results for PSD films. 85

Table 19 Compiled verification output for all methods for tolerance limit 90%. 86

Table 20 Compiled verification output for all methods for tolerance limit 95%. 87

Table 21 Cochran's Q test results for different methods for different gamma parameters for gamma pass rate 90%. 87

Table 22 Cochran's Q test results for different methods for different gamma parameters for gamma pass rate 95%. 87

Table 23 Kruskal-Wallis test result summary for gamma value results between different methods. 89

Comparing the results presented in Table 24, Table 25 and Table 26, it was noticed that the GI for PSD are closely between the results obtained for EBT and SRS. On the basis of these results it was hypothesised that the absolute difference between PSD to EBT and PSD to SRS is smaller than the difference between EBT and PSD. The null hypothesis H_0 can be written as: 90

Table 27 Wilcoxon signed-rank results to verify hypothesis that GI results for PSD is between EBT and SRS. 90

Table 28 : The number of potentially false positive results for plastic scintillators. A potentially false positive event is counted when verification with two reference methods is negative while the plastic scintillator is positive. 91

Table 29 Number of potentially false negative results for plastic scintillator. Potentially false negative event is counted when verification with two reference methods is positive while plastic scintillator is negative. 91

Table 30 Median, 25^{th} and 75^{th} quantiles for gamma index for different methods for DD=2% and DTA=2 mm. 92

Table 31 Total cost of ownership, operating expense. Prices in euro. 95

LIST OF FIGURES

Figure 1 Response curves for Tumour Control Probability (TCP) and Normal Tissue Complication Probability (NTCP). Curves represent integrated linear weighting of diverse factors associated with a specific dose distribution. The units on the x-axis can be conceptualized as "equivalent dose" units [38]. 7

Figure 2 Cross section for photoelectric effect σ_f, Compton effect σ_c and pair production σ_p in function of energy and atomic number [129]. 11

Figure 3 Schematic diagram of a medical linear accelerator [130]. 13

Figure 4 Schematic representation of the gamma index method in 1D. 24

Figure 5 Jablonski diagram presenting the π-electronic atomic levels of organic molecules. [75] 27

Figure 6 Image of absorption and emission spectra (Wikipedia). 29

Figure 7 Mass energy absorption coefficients for plastic scintillator compared to water and polystyrene as a function of photon energy [86]. 32

Figure 8 Schematic view of Cerenkov light generation in a dielectric medium. When a particle of velocity v > c/n traverses a medium of refractive index n, Cerenkov radiation is emitted in a cone of half angle θ with velocity c/n. 38

Figure 9 Comparison between CCD-based and CMOS-based image sensor approach [99]. .. 40

Figure 10 Emission spectrum of BC-400(left) and one of examined BC400 sheet (right). 43

Figure 11 Applied plastic scintillator image processing. 46

Figure 12 The system setup at the linac. Main elements on left schematic view: beam (1), build-up (2), PSD (3), mirror (4) and camera (5) [108]. 47

Figure 13 Schematic cross section of experimental setup. 51

Figure 14"v-slot 20" aluminium profile cross section with dimensions [109]. 52

Figure 15 Phantom frame 3D visualization (left) and constructed phantom frame (right). 52

Figure 16 Complete phantom with covers. 53

Figure 17 Quick Release Plate (left) Tripod Head that enable adjust camera angles(middle) and complete camera mount on trolley. 54

Figure 18 Different views of the camera shielding. The triggering electronics can be seen on the right side of the camera. 55

Figure 19 Arduino nano served as IR remote trigger controlled via USB. 56

Figure 20 Plastic scintillator mounted to PMMA slab. Graff tape and black painting is visible. 56

Figure 21: Detector Array Spacing [116]. 59

Figure 22: SunNuclear SRS MapCHECK detector in StereoPHAN phantom. 60

Figure 23: Sample screen from SRSMapCHECK software. 61

Figure 24 On the left, one of the first images collected for a 5 × 5cm field in the isocentre with a white background and no black tape around the edges. Right: image collected with a matte black background and with tape on the edges. Even the irregularities on the lower and upper edges due to the alignment of the MLC collimator leaves can be seen. 67

Figure 25 Signal as mean pixel value for different exposure times at different ISO settings. The results were filtered using the median and Wiener filters. Error bars represent the standard deviations of the individual measurements [108]. 68

Figure 26 Measurement of stray radiation as a function of dose. Signal as mean pixel value vs. the delivered dose for the field 15 × 15 cm^2. Each measured value contains the electronic noise and stray radiation signal. The CMOS camera ISO was set to 100. Error bars represent the standard deviations of the individual measurements [108]. 69

Figure 27 Measurement of stray radiation in relation to field size. Signal as mean pixels value vs. different square field sizes (side of the square field). Results presented for three different ISO values. The standard deviation of each signal value is imposed on bar graph [108]..... 70

Figure 28 Repeatability measurements at ISO 200 and 400 as percentage differences to average results from all series. The standard deviation (SD) of each signal value is imposed on bar graph. The average SD for ISO 200 and 400 is 1.41% and 0.93% respectively. The lower SD for ISO 400 is due to the higher signal, while the noise is comparable for both setups [108]. 71

Figure 29. Repeatability measurements at ISO 200 and 400 as percentage differences to average results from all series. The standard deviation (SD) of each signal value is imposed on bar graph. The average SD for ISO 200 and 400 is 1.41% and 0.93% respectively. The lower SD for ISO 400 is due to the higher signal, while the noise is comparable for both setups [51]... 71

Figure 30. The signal versus normalised dose (arbitrary units). 72

Figure 31 Dose vs. the camera aperture F curve. Fit using $xa + xb$ function [108]. 74

Figure 32 Measured signal versus dose from TPS for different photon energies. Signal was converted to dose and rescaled to the absolute value. The standard deviation plotted on the bar graph [108]. 74

Figure 33 Cross section of plastic scintillator acquired raw image field "M232066-1". 83

Figure 34 Boxplot for gamma distribution of Gafchromic (EBT), SRS MapCHECK (SRS) and plastic scintillator (PSD) for different gamma setup: left to right DD 1-3%, top to bottom 1-3 mm. Passing rate 95%, threshold 10%. On each plot first result is for Gafchromic EBT-3 film (EBT), second for SMS MapCHECK (SRS) and third for experimental plastic scintillator setup (PSD). On each box, the central mark indicates the median, and the bottom and top edges of the box indicate the 25th and 75th percentiles, respectively. The whiskers extend to the most extreme data points not considered outliers, and the outliers are plotted individually using the '+' marker symbol. 86

Figure 35 Median cumulative histogram of gamma index for 41 cases analysed with 2%/2 mm. On the right site zoom in for better view on region of interest. Blue colour represents PSD, grey colour SRS MapCHECK and red EBT-3 Gafchromic films. Dashed lines represent 25^{th} and 75^{th} quantiles. 92

LIST OF ABBREVIATIONS

AAPM: American Association of Medical Physics

APS: Active Pixel Sensor

CAPEX: Capital Expenditure

CDF: Cumulative Distribution Function

CMOS: Complementary Metal-Oxide-Semiconductor

CoP: Code of Practice

DD: Dose Difference

DQA Delivery Quality Assurance

DTA: Distance-to-Agreement

EBRT: External Beam Radiotherapy

FF: Flattening Filter

FFF: Flattening Filter-Free

GH: Gamma Histogram

GI: Gamma Index

IAEA: International Atomic Energy Agency

IMRT: Intensity-Modulated Radiotherapy

KCO: Katowice Oncology Centre (Katowickie Centrum Onkologii)

LCPE: Lateral Charged Particle Equilibrium

LINAC: Linear Accelerator

MLC: Multileaf Collimator

OAR: Organ at Risk

OPEX: Operating Expenses

OSLD: Optically Stimulated Luminescent dosimeters

PDD: Percentage Depth Dose

PEF: Pentax Electronic File

PSD: Plastic Scintillator Detector

PSQA Patient-Specific Quality Assurance

QA: Quality Assurance

QI: Quality Index

ROIC: Readout Integrated Circuit

SABR: Stereotactic Ablative Radiotherapy

SBRT: Stereotactic Body Radiation Therapy

SRS: Stereotactic Radiosurgery

SSD: Source-to-Surface Distance

ST: Stereotactic techniques

TCO: Total Cost of Ownership

TLD: Thermoluminescent dosimeters

TPS: Treatment Planning System

TRS: Technical Reports Series

VMAT: Volumetric Modulated Arc Therapy

1 INTRODUCTION

In 2020, an estimated 19.3 million new cancer cases and nearly 10.0 million cancer deaths occurred globally [1]. Radiotherapy, employed in approximately 50% of cancer all cases, serves as a primary treatment or complements chemotherapy and surgery [2] [3]. Clinically, megavoltage photon beams are still cost-effective and are one of the most common treatment methods in external beam radiotherapy (EBRT) [4] [5] [6]. Over the past years, new advanced treatment modalities have emerged with the aim to deliver very high doses to small targets using classical linear accelerators (linacs). These include stereotactic radiosurgery (SRS), stereotactic radiotherapy (SRT), stereotactic body radiation therapy (SBRT) and stereotactic ablative radiotherapy (SABR). These modalities have demonstrated significant advantages, highlighting their efficacy in cancer treatment [7] [8]. One of the most distinct features of these techniques is the utilisation of small fields and beamlets for treatment.

In recent years, dynamic techniques such as intensity-modulated radiotherapy (IMRT) and volumetric modulated arc therapy (VMAT) have become the most popular methods for delivering external beam radiotherapy. They contributed to more precise dose distributions in target areas, improved protection of critical organs and reduced treatment durations. In IMRT the radiation beam's intensity is modulated either through multiple static multileaf collimator (MLC) segments using the step-and-shoot technique or by continuously moving MLC leaves during radiation delivery, known as the sliding window technique. In VMAT, the position of the multileaf collimator leaves changes dynamically during the gantry rotation around the patient. Simultaneously, the dose rate is modulated throughout the arc delivery. The VMAT technique is employed as a more efficient method to deliver highly conformal dose distributions, serving as an alternative to both sliding window and step-and-shoot IMRT. These approaches typically involve the use of numerous small fields continuously irradiated while machine geometry is changing.

Stereotactic techniques deliver high-dose radiation to a target volume. The typical dose of single-fraction radiation used in SRS ranges from 12 to 24 Gy [9], which can be up to 12 times higher than the dose for a standard single fraction. Flattening filter-free (FFF) beams offer dose rates up to four times higher than those of flattening filter (FF) beams and are commonly used in stereotactic techniques. FFF beams are commonly used to speed up therapy and avoid unintended patient movements and changes in geometry. Nevertheless, the use of FFF beams

introduces additional challenges for dosimetry due to beam heterogeneity, sharp penumbra, and the crucial positioning of detectors.

The use of IMRT, VMAT, and FFF beams exemplifies a significant stride in optimising the therapeutic outcome in stereotactic techniques, emphasising improved accuracy, targeted treatment, and patient comfort. However, these advanced techniques pose new challenges in the determination of dosimetric parameters, especially in patient specific quality assurance (PSQA).

The accurate dosimetry of small fields used in modern treatment techniques makes the measurement difficult due to the steep dose gradient, loss of lateral charge particle equilibrium, volume averaging, detector material artefacts, the partial occlusion of the radiation source, and detector position-orientation effects [10] [11]. Furthermore, the directional and energy response of detectors influence the measurements in small field dosimetry [12] [13]. In addition, the volume averaging and perturbation occur due to the finite size of the active volume of the detector and the presence of non-water equivalence materials [14] [15]. The directional response of a detector during beam characteristics measurement is crucial because angular distribution of electrons and scattered photons changes with depth and distance from the beam centre [16]. No ideal detectors exist in small field radiation dosimetry since they perturb the radiation field and introduce systematic errors affecting measurement results. Commonly used detectors in the dosimetry of photon fields include ionisation chambers, diodes, diamonds, thermoluminescent dosimeters (TLD), optically stimulated luminescent dosimeters (OSLD) and radiochromic film dosimeters [17] [18] [19] [20] [21] [22] [23] [24].

Radiochromic films are widely recognised in the field of radiation therapy for their use in dosimetry, including beam geometry measurements [25]. While it may not be explicitly stated as the “golden standard” for planar dose distribution, their widespread use and the research conducted on them suggest their significant role in this field. Nowadays, modern high resolution matrix detectors, often referred as SRS matrices, gradually replace radiochromic films for small films which have been traditionally used for small field geometry measurements [26]. The transition towards SRS matrix detectors is driven by several factors. Firstly, SRS matrix detectors offer real-time data acquisition, which is a significant advantage over radiochromic films, which require post-exposure processing. This real-time capability allows for immediate feedback and adjustments during treatment delivery, therefore enhancing the efficiency and accuracy of the process. Secondly, SRS matrix detectors are reusable, unlike radiochromic films which are single-use. This reusability makes SRS matrix detectors a more sustainable and cost-

effective option for small field geometry measurements in the long run. However, the transition to SRS matrix detectors is a gradual process. Radiochromic films have been the standard for many years and have a well-established role in radiotherapy. They are known for their high spatial resolution and tissue-equivalent response, making them highly reliable for dosimetry measurements. Therefore, while SRS matrix detectors offer promising advantages, the shift towards their widespread use in place of radiochromic films is happening slowly as the technology continues to be validated and adopted in clinical practice.

Patient-specific quality assurance (PSQA) of stereotactic treatment faces challenges attributed to dosimetry in small fields and dynamic techniques. To address these complexities, it is recommended to perform QA by comparing the dose distribution from the treatment planning system (TPS) with that measured using a planar detector during plan delivery [27]. The Gamma Index (GI,γ) serves as a quantitative metric to evaluate the agreement between the TPS-calculated dose and the measured dose [28]. It's particularly useful for comparing two-dimensional (2D) and three-dimensional (3D) dose data, especially when direct measurement is challenging [29].

The most popular technique for measuring planar dose distribution measurement in small fields has been radiochromic film [30]. Unfortunately, this technique has its drawbacks. It is complex to handle, requires proper processing and is single-use which means a new film is required for each measurement. This can lead to increased costs over time, especially in settings where frequent measurements are required.

Recently, high resolution active detector matrices dedicated to stereotactic fields have emerged [31] [32] [33]. While they offer the advantage of being reusable, their initial cost can be a barrier. They have a lower resolution compared to radiochromic films. This means that while they can provide a general overview of the dose distribution, they might not capture the fine details that can be detected with radiochromic films.

Given the challenges associated with both radiochromic films and detector matrices, it is worthwhile to investigate alternative methods for dose distribution measurement in small fields. One promising alternative is the Plastic Scintillator Detector (PSD). PSDs offer several potential advantages that could address the limitations of the current techniques. Firstly, PSDs are reusable, like detector matrices, which make them a cost-effective solution in the long run. Secondly, PSDs have been reported to offer high spatial resolution, potentially comparable to Gafchromic films which could allow for detailed dose distribution measurements.

Moreover, PSDs are known for their tissue-equivalent response, which is crucial for accurate dosimetry in radiotherapy. They also offer real-time data acquisition, which can provide immediate feedback and allow for adjustments during treatment delivery. However, while PSDs are promising, it is important to note that their application in small field dosimetry is still an area of ongoing research. As a result, higher availability and improved accuracy and efficiency of these detectors can be achieved.

In this context, the research presented in this dissertation investigated the use of a thin scintillation sheet as a detector for patient-specific pre-treatment verification of small fields. Together with the commercially available Complementary Metal-Oxide-Semiconductor (CMOS) camera, commonly available computer software and self-developed scripts in the MATLAB (The MathWorks, USA) and ImageJ [34] were used for PSQA. This study aimed to prove that simple and cost-effective setup can enhance the precision of treatment verification and, therefore, ensure optimal patient outcomes.

2 OBJECTIVES AND OUTLINE

While dosimetry films have been a widely accepted and recognised method in radiotherapy facilities for a long time, the use of modern high-resolution dosimetry arrays dedicated to stereotactic radiotherapy verification has become more common. Unfortunately, both methods have drawbacks. The first method is complex and time-consuming while the second method has lower resolution compared to films and can be prohibitively expensive.

The primary objective of this doctoral thesis was to investigate the feasibility of using plastic scintillators for PSQA in a radiotherapy department by comparing them to referenced methods – Gafchromic films and high-resolution planar matrix detectors. The study aimed to validate treatment plans by employing a custom phantom designed and constructed by the author, a plastic scintillation detector and a CMOS camera.

The study systematically examined the characteristics of plastic scintillators, including the entire setup involving the CMOS camera. Various tests were conducted, including background checks, noise analysis, image correction, dose response, dose rate dependence, repeatability, and energy dependence.

A novel system for small dynamic fields has been developed with the consideration of the resulting characteristics. This system is based on the tissue equivalent plastic scintillator material, where radiation dose is converted to light and CMOS high resolution camera to capture and store images of the light distribution. Subsequently, the captured images are processed resulting dose distribution.

Finally, a comprehensive system evaluation was performed. PSQA beams were delivered to the developed system, radiochromic films and a commercial SRS active detector matrix to evaluate the reliability of the new system. Data analysis was carried out including field-to-field and method-to-method comparisons. The study was performed at the Katowice Oncology Centre, with subsequent analysis conducted at the August Chełkowski Institute of Physics, the Faculty of Science and Technology, the University of Silesia in Katowice.

The specific objectives of this study were as follows:

- to characterise plastic scintillators for dosimetry purposes,
- to investigate camera settings and post-processing parameters impact the obtained results.
- to perform PSQA for clinical treatment plans in small fields using plastic scintillators, Gafchromic films and SRS 2D matrix detectors, along with a detailed analysis.

3 THEORY

3.1 PRINCIPLES OF RADIOTHERAPY

Radiation therapy is a widely used approach in cancer treatment [3] [35] [36]. In clinical practice, it is often combined with chemotherapy and surgical procedures [37]. This technique involves administering high-energy ionising radiation to the patient, aiming to eliminate or inhibit the proliferation of neoplastic cells while sparing normal tissue from radiation-induced damage.

On a cell level, when the body is exposed to ionising radiation, part of the energy can lead to DNA damage and disrupt the biological function of the cells. Depending on the extent of the damage, the affected cell may fully recover, undergo mutation transmission or ultimately die. Typically, if only one strand of the DNA chain is harmed, the other strand acts as a template for repair, given that the nucleotides of the two strands are complementary. Conversely, in the event of a double-strand break, the cell either succumbs to death or, more infrequently, undergoes mutation, transmitting the mutation to its progeny.

Radiosensitivity is inextricably linked to the rate of proliferation – a higher proliferation rate causes higher susceptibility to ionised radiation. Cancer cells exhibit a distinctly higher proliferation rate compared to healthy cells. Consequently, healthy cells show reduced sensitivity to radiation damage, allowing the treatment to be more selectively targeted toward the intended tissue. Radiotherapy is employed when the likelihood of causing radiation damage to tumour significantly offsets the probability of damaging normal tissue. Figure 1 illustrates the dose-response curves for tumour tissue and normal tissue, characterised as Tumour Control Probability (TCP) and Normal Tissue Complication Probability (NTCP), respectively. Although both curves exhibit sigmoidal shapes, the NTCP curve is typically steeper than the TCP curve, reflecting the greater sensitivity of normal cells to radiation-induced damage. Striking a balance between side effects and efficacy is crucial when planning treatments.

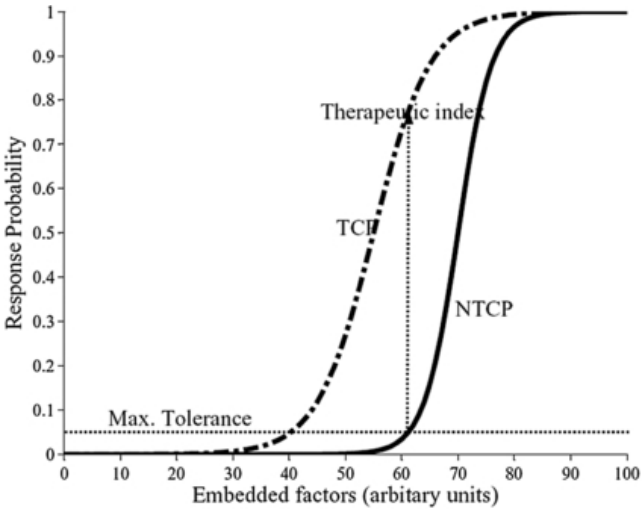

Figure 1 Response curves for Tumour Control Probability (TCP) and Normal Tissue Complication Probability (NTCP). Curves represent integrated linear weighting of diverse factors associated with a specific dose distribution. The units on the x-axis can be conceptualized as "equivalent dose" units [38].

Radiation therapy is applied in various scenarios, such as when complete destruction of tumour cells is necessary for recovery (sometimes in conjunction with chemotherapy cycles), post-surgery to prevent potential residual cell proliferation, or to alleviate symptoms in terminal patients who cannot recover.

Numerous types of radiotherapy exist, including external beam radiotherapy, brachytherapy, metabolic radiation therapy, and intra-operative radiation therapy. In this work, we will focus on external beam radiation therapy, where the body is irradiated from the radiation source that is external to a patient. To be more specific – using a linear accelerator.

Over the years, various strategies have been developed to enhance treatment efficiency:

- Limiting the Total Irradiated Dose: Even if tumour tissue is underexposed, limiting the total dose helps to minimise side effects.
- Fractionation: Dividing the total dose into separate daily sessions allows normal cells to recover between sessions, thereby reducing damage to healthy tissue surrounding the target.
- Multi-Directional Irradiation: Targeting the tumour from different directions improves treatment precision.

Upon initiating treatment, in classic radiotherapy, a preliminary CT (Computed Tomography) scan is conducted to precisely pinpoint the target. To ensure consistency across different sessions, the patient must maintain the exact same position. Small reference points are permanently marked on the skin to mitigate errors and various immobilising tools are employed during target delineation. Additionally, there are tattoo-less techniques that usually involve surface-guided methods [39]. Moreover, in image guided radiotherapy (IGRT) before each session, additional imaging is performed to compare it with the reference, identifying any potential movements of the target.

Typically, standard fractionation involves daily sessions for five to thirty-five consecutive workdays. However, exceptions exist: higher dose irradiations may be planned with sessions separated by two or more days, or lower dose irradiations may be administered on the same day with a minimum six-hour break between them. The typical dose delivered during treatment session is about 2 Gy.

Stereotactic techniques (ST) in radiotherapy, SRT, SRS, SBRT and SART, are techniques which precisely target tumours with a high dose of radiation. They differ in the number of treatments required and the area of the body treated. With ST, patients receive radiation throughout the body in one to five treatment sessions to tumours. A fractional dose can be up to 24 Gy per session.

3.2 PHYSICS AND CHARACTERISTICS OF CONVENTIONAL MEDICAL ACCELERATOR PHOTON BEAM

Most radiotherapy treatments are performed using megavoltage photons [3]. In external beam radiotherapy, radiation is emitted from a machine situated at a distance from the patient's skin. X-rays are generated exclusively when the 'beam is on'. The collisions of accelerated electrons with a target material, create bremsstrahlung radiation. Most photons have less energy than this maximum and the energy spectrum of an X-ray source exhibits a peak at approximately one-third of the maximum.

The photon energy spectrum in the X-ray beam at a selected acceleration potential is influenced by factors such as the target material, beam filtration, and the design of the linac head. The depth of beam penetration is associated with the maximum accelerating potential. That’s why linear accelerators are intended for treating tumours in the body’s midsection.

While the term ‘megavoltage’ technically applies to any beam over 1 MV, in practical radiotherapy applications beams typically range from 4 MV to 25 MV. The most common combination for a standard accelerator delivering intensity-modulated radiotherapy (IMRT) and volumetric-modulated arc therapy (VMAT) involves energy of 6 MV and 10 MV.

Photon radiation interaction with matter

When a photon traverses matter, it undergoes various interaction reactions. The probability of a specific interaction depends on two main factors: the energy of the photon and the mass number of the medium with which the photon interacts. As a consequence, the beam is attenuated. In some of these interactions, the photon’s energy is transferred to matter, mainly to electrons belonging to atoms or molecules within the matter. Due to their short range, these electrons dissipate their energy locally around the point of interaction. The locally absorbed energy becomes the cause of radiative effects or tissue damage. If a photon enters and exits the medium with its entire undisturbed energy or if it only changes its direction due to interaction with the medium, there is no delivery of dose to the medium.

The attenuation of a monoenergetic beam of photons passing through an absorber is proportional to the number of incident photons (N) and the thickness of the absorber (dx):

$$dN \propto Ndx. \tag{1}$$

The constant of proportionality is called the linear attenuation coefficient, μ. This yields to the following equation for the beam:

$$I(x) = I_0 e^{-\mu x}, \tag{2}$$

where $I(x)$ is the beam intensity in a function of depth x.

In the range of energies used in radiotherapy, most processes occur with very low probability and only four fundamental processes are significant, with three of them leading to the transfer of energy to the medium. Those are coherent scattering, photoelectric effect, Compton effect, and pair production. Thus, the attenuation coefficient is given by the sum of four coefficients:

$$\frac{\mu}{\rho} = \frac{\sigma_s}{\rho} + \frac{\sigma_f}{\rho} + \frac{\sigma_c}{\rho} + \frac{\sigma_p}{\rho}, \tag{3}$$

where σ_s, σ_f, σ_c and σ_p are the attenuation coefficients for coherent scattering, photoelectric effect, Compton effect, pair production, respectively, while ρ is the density of the absorber.

Coherent scattering

When the incident photon comes across an electron, it sets it into oscillation. Then, the electron irradiates the energy it has absorbed in the form of another photon with the same frequency as the first one. No energy is absorbed by the atom due to this process. Scattering is the only effect.

The probability for coherent scattering to take place is high only for high atomic number materials and low energy photons. As a consequence, this is not a process of interest for the purpose of radiotherapy.

Photoelectric effect

The photoelectric effect occurs when the interaction between the incident photon and the atom of the absorber leads to the ejection of an orbital electron from the atom. The energy of the electron E_e equals the difference between the energy of the photon $h\upsilon$ and the binding energy of the electron E_B:

$$E_e = h\upsilon - E_B. \quad (4)$$

A vacancy is formed bringing the atom to an excited state. The electron gap in the inner shell is filled by an electron of another shell and thus an X-ray photon is emitted. Then, the atom can return to its ground state. Also, the emission of Auger electrons is possible within this process.

As for biological absorbers, the energy of characteristic X-rays is sufficiently low to assume that all the energy is deposited within the atom. The cross section for photoelectric will be denoted as σ_f .

The Compton effect

In this case the incident photon interacts with an orbital electron that is approximately free, in the sense that the energy of the photon is much higher than the binding energy of the electron. As a result, both the electron and the photon are scattered. This phenomenon is different from coherent scattering because of the energy transfer between the photon and the electron.

The cross section for the Compton effect will be denoted as σ_c .

Pair production

When the energy of the photon is at least 1.02 MeV, pair production can occur. In this case, the photon releases all its energy due to the interaction with the electromagnetic field of the atomic nucleus and creates an electron and a positron.

The threshold energy is set at 1.02 MeV because the rest mass energy of the electron is 0.511 MeV. The cross section for photoelectric effect will be denoted as σ_p .

The cross section for each of the phenomena described above is not constant. In fact a dependence exists between the probability for each process to occur and the energy and atomic number of the photon and the absorber respectively.

Graph in Figure 2 present predominant effect in relation to effective atomic number Z_{eff} and photon energy.

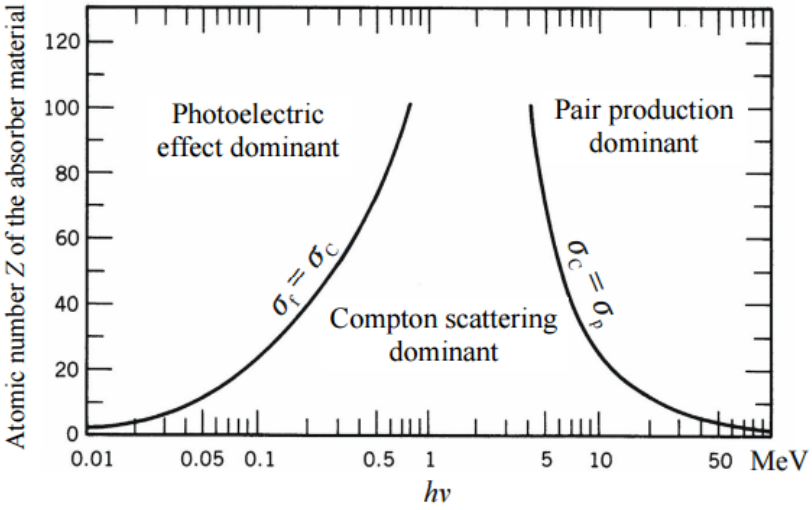

Interaction with tissue

The effective atomic number Z_{eff} depends on the atomic composition of the mixture as well as on the type and quality of the radiation beam. For megavoltage photon and electron beams Z_{eff} of a mixture is defined by [40]

$$Z_{eff} = \frac{\sum_i a_i \frac{Z_i^2}{A_i}}{\sum_i a_i \frac{Z_i}{A_i}}, \quad (5)$$

where:

- a_i is the mass fraction of constituent element *i*,
- Z_i is the atomic number of constituent element *i*,
- A_i is the atomic mass of constituent element *i*.

Average soft tissues are mainly composed of low-atomic number (Z) such as H, C, N, O, and so on [41]. ICRU report 44 [42] describes various types of tissue substitutes for human organs and tissues.

Z_{eff} for soft tissues is 7.42 while Z_{eff} for bones is in the range 11.6–13.8 [43]. Z_{eff} of 7.8 for air and 7.5 for water. The energy range in radiotherapy treatments is between 1 MeV and 25 MeV. Combining all this information and referencing to Figure 2, it is visible that the predominant effect of megavoltage photons in tissue is the Compton effect.

Beam parameters

The phenomena presented above illustrate the reactions of a single photon in contact with matter. In the case of a three-dimensional beam of X-ray radiation impinging on the environment, parameters describing the spatial distribution of the dose resulting from the reactions described above play a significant role.

The fundamental functions describing the megavoltage photon beam include the percentage depth dose (PDD), which depicts the change in dose percentage with depth in the irradiated medium, the relative dose distribution across the radiation beam concerning the dose value on the beam axis referred to as the radiation beam profile, and the quality index (QI) of high-energy radiation.

These functions are typically determined based on measurements with appropriate radiation detectors in a tissue-equivalent phantom. The dose or dose rate at a reference point is specified in the phantom under strictly defined reference conditions, such as depth, field size, and source-to-surface distance (SSD).

3.3 MEDICAL LINEAR ACCELERATOR

The quest for generating high-energy X-ray beams commenced in the 1930s, lead to the construction of large accelerators utilising high-voltage potentials to yield more penetrating radiation. This innovation aimed to deliver doses deeper into the patient's tissues. Subsequently, in the 1950s, high-energy photon beam production underwent a revolutionary transformation with the introduction of radio waves, giving rise to the modern medical linear accelerator. In contemporary times, the technological landscape is exceptionally impressive, enabling the electrical generation of a diverse array of ionising radiation beams.

Megavoltage radiotherapy beams typically used in clinics span energies from 4 to 25 MV for photons and 4 to 25 MeV for electrons, constituting the primary modality for radiation treatment.

A medical linear accelerator customises high energy X-rays or electrons to conform to a tumour's shape and destroy cancer cells while sparing surrounding normal tissue. It features several built-in safety measures to ensure that it will deliver the dose as prescribed and is routinely checked by a medical physicist to ensure its proper operation.

Prior to the start of treatment and the implementation of quality assurance procedures, the created treatment plan is checked to ensure that each treatment is performed in the same way.

A medical linear accelerator is the device most used for external beam radiation treatments for patients with cancer. The linacs are used to treat all body sites, using a number of techniques like 3D conformal radiotherapy, Intensity-Modulated Radiation Therapy, Volumetric Modulated Arc Therapy, Image Guided Radiation Therapy, Stereotactic Radiosurgery and Stereotactic Body Radio Therapy.

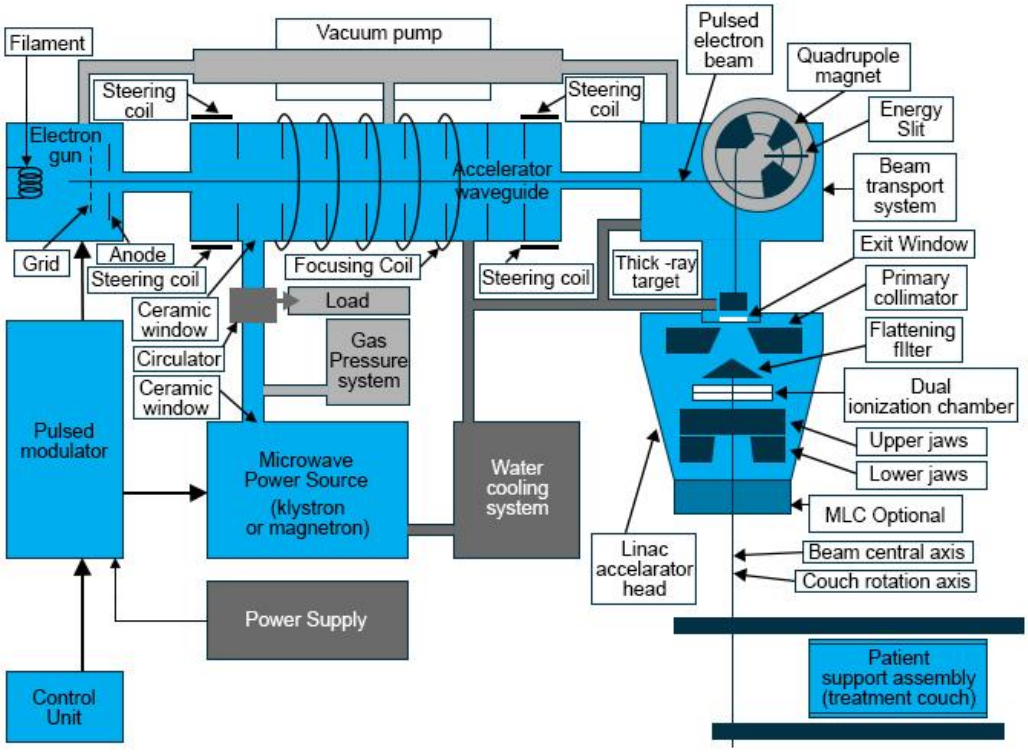

Figure 3 Schematic diagram of a medical linear accelerator [130].

The linear accelerator uses microwave technology to accelerate electrons in a part of the accelerator called the "wave guide". It then allows these electrons to collide with a heavy metal target like tungsten to produce high-energy X-rays. These high energy X-rays are shaped as they exit the machine to conform to the shape of the patient's tumour and the customised beam is directed to the patient's tumour. The common name for all kinds of devices that shape a primary beam is called a Beam Limiting Device (BLD). The beam is usually shaped by a multileaf collimator that is incorporated into the head of the machine. The patient lies on a moveable treatment couch and the correct position is secured by lasers. The treatment couch can move in several directions including up, down, right, left, in and out. The beam comes out from a part of the accelerator called a gantry which can be rotated around the patient. Radiation can be delivered to the tumour from many angles by rotating the gantry and moving the treatment couch. A schematic block diagram of a linac is presented in Figure 3.

The main operating components of a medical linac are usually grouped into 6 sections shortly described below.

- *Injection system*

The first section is called the electron gun where electrons are produced by thermionic emission from a heated cathode.

Two basic types of the electron gun exist:

*The Diode Type:*In the diode gun the voltage applied to the cathode is pulsed, therefore producing bunches of electrons rather than a continuous stream.

The Triode Type: In the triode gun, discrete bunches of electrons are produced by introducing a grid between cathode and anode.

The process of electron injection into the accelerating waveguide is controlled by voltage pulses. These pulses, applied to the grid or directly to the electron gun, need to be in sync with the pulses directed towards the microwave generator.

- *RF system*

The electrons are accelerated in the accelerating waveguide using high power RF fields which are set up by microwave radiation. This radiation is produced by microwave generators that are either magnetrons or klystrons. Magnetrons produce microwaves required for electron acceleration while Klystrons act as an RF power amplifier.

- *Accelerating waveguide*

The third section, waveguides, are vacuum- or gas-filled metallic structures of rectangular or circular cross-section that are used to transmit microwaves. Two types of waveguides are used in linacs: RF power transmission waveguides and accelerating waveguides. The power transmission waveguides transmit the RF power from the power source to the accelerating waveguide where the electrons are accelerated.

- *Auxiliary system*

The linac auxiliary system (class four) consists of a number of services that are not directly involved in electron acceleration, but which make acceleration possible and the linac viable for clinical use.

- *Beam transport system*

In the fifth class, the beam transport system consists of the evacuated drift tubes and bending magnets, which are used to transport, focus, and position the electron beam from the accelerating waveguide to the X-ray target or to the exit window for electron beam therapy.

- *Beam collimation and monitoring systems*

In a typical modern medical linac, photon beam collimation is achieved with two or three collimator devices:

- Primary collimator - defines the largest available circular field size and is a conical aperture machined into a tungsten shielding block with the sides of the conical aperture projecting onto the edges of the target at one end of the block and onto the flattening filter at the other end.
- Secondary movable beam-defining collimators - consisting of four blocks, two forming the upper and two forming the lower jaws of the collimator.
- Multileaf collimator (MLC) - the idea behind the MLC is simple, but building a reliable MLC system is a significant technological challenge.

The treatment head is one of the most important parts of a linear accelerator. It consists of a thick shell of high-density shielding material (i.e. lead, tungsten, or alloys) and contains several components.

Linac Calibration

In the context of medical linear accelerators used for radiotherapy, the unit of dose delivered is the monitor unit (MU). The MU is typically defined so that the delivery of 1 MU is equivalent to a dose of 1 cGy under certain reference conditions. These conditions are defined by a specific field size, source-to-surface distance and depth in water. For a photon beam in conventional linacs, the reference conditions typically include a field size of 10 cm × 10 cm, an SSD of 90 cm and a depth in water of 10 cm as specified by the Technical Reports Series No. 398 "Absorbed Dose Determination in External Beam Radiotherapy", the International Code of Practice for Dosimetry Based on Standards of Absorbed Dose to Water published by the International Atomic Energy Agency [IAEA] in 2000 [44].

3.4 IMRT AND VMAT TECHNIQUES

Volumetric modulated arc therapy (VMAT), originally proposed in 1995 as intensity modulated arc therapy (IMAT), is a radiotherapy technique involving the delivery of a rotating cone beam characterised by variable shape and intensity [45]. During a VMAT session, the gantry undergoes continuous motion and the arc experiences fluctuations in MLC sheets and dose rate. This method has demonstrated improved efficacy in terms of treatment duration and dose distribution efficiency. In particular, it achieves a reduced dose to organs at risk (OARs) compared to older techniques such as IMRT or 3D conformal radiotherapy.

The reduced dose to OARs is a notable advance and benefit, especially for patients at risk of secondary malignancies due to life expectancy considerations. In paediatric cases where risk is a significant concern, VMAT serves as a valuable alternative to IMRT or in situations where proton therapy is not an option. In addition, the shorter overall treatment time associated with VMAT offers several advantages, primarily in minimising patient movement during treatment [46].

In advanced techniques such as IMRT and VMAT, the dose distributions are intricately shaped to closely match the target volumes. This design results in sharp dose gradients, particularly in the transition region between the target and adjacent healthy normal tissue. This increases the potential for missing the target due to factors such as patient positioning errors, organ motion, or even slight variations in treatment delivery:

Determining Margins

Precise margins around the target volumes must be determined to account for uncertainties related to patient positioning, organ motion, and other variables. Appropriate definition of these margins is critical to ensure effective target coverage while minimising the risk of irradiating adjacent healthy tissue.

Reproducing Treatment Setup

Consistency in treatment setup is paramount. Accurately reproducing the treatment setup at each of the many visits a patient makes during the course of treatment is critical to maintaining the intended dose distribution and optimising treatment outcomes.

Verification of Dose Administration

Rigorous verification procedures are required to ensure that the dose is delivered according to the intended plan. This involves regular checks and validations to confirm that the dose delivered is consistent with the prescribed dose and the planned distribution.

Given the complexity of these advanced radiotherapy techniques, addressing these considerations is fundamental to achieving treatment goals while minimising the risk of inadvertently affecting healthy tissue.

The evaluation of IMRT and VMAT plans in specific clinical settings has been based primarily on studies comparing various treatment planning parameters. These parameters include, but are not limited to, dose-volume histograms, dose statistics, normal tissue complication probabilities, and tumour control probabilities. These comparisons are made with those calculated using conventional or alternative conformal techniques. The aim is to systematically analyse and evaluate the performance of IMRT and VMAT compared to established techniques, taking into account factors such as dose distribution, normal tissue impact, and tumour control probability.

3.5 DOSIMETRY

Dosimetry is the science of measuring, calculating, and assessing doses of radiation absorbed. In the context of radiotherapy, it plays a crucial role in ensuring patient safety and treatment accuracy. The ultimate goal of dosimetry is to determine the absorbed dose in organs or

tumours. Absorbed dose refers to the amount of energy deposited by ionising radiation per unit mass of tissue. Dosimetry ensures that radiation therapy machines are accurately calibrated and deliver the intended dose to the target area while minimising exposure to healthy tissues. It helps optimise treatment plans, monitor patient response, and prevent over- or under-dosing.

While dosimetry is essential, it also faces challenges. A few of them are described below.

Small field dosimetry

In the domain of small field dosimetry, numerous intricate factors contribute to the complexity and challenge inherent in this discipline. These factors encompass a range of issues, including the steep gradient of radiation dose, the occurrence of lateral charged particle equilibrium (LCPE), the partial occlusion of the radiation source, challenges in beam alignment, and the inability to employ a reference dosimeter [23].

Moreover, the presence of heterogeneous media, such as bone and lung tissue, necessitates additional considerations due to the perturbation of the beam. The interaction of the radiation beam with these heterogeneous media can significantly alter the distribution of the dose, thereby complicating the task of accurate dosimetry.

LCPE happens when the radiation field size is too small or the density of irradiated material is too low to provide sufficient electrons going into the dose volume. When considering small fields, the phenomenon of lateral disequilibrium presents a significant challenge. This disequilibrium arises due to the secondary electron track lengths and the source size projected through the collimating system being comparable to the treatment field size.

These complexities underscore the need for advanced techniques and methodologies in small field dosimetry, as well as a comprehensive understanding of the underlying physics and biology involved in radiation therapy.

The complex beam delivery techniques for patient treatment using a clinical linear accelerator (linac) may result in variations in the photon spectra, which can lead to dosimetric differences in patients that cannot be accounted for by current treatment planning systems (TPSs).

The Code of Practice (CoP) for dosimetry of small static fields in external megavoltage photon beam radiotherapy was jointly developed by the IAEA and the American Association of Medical Physics (AAPM) and released as Technical Reports Series. This CoP is known as TRS-483 and was published by the IAEA in 2018. It provides guidelines and reference dosimetry procedures specifically tailored for small fields.

Dynamic techniques dosimetry

The latest generation of IMRT and VMAT techniques has recently become widely available. In comparison to static-beam in IMRT, rotating VMAT is designed to reduce treatment time while maintaining or improving plan quality [47] [48]. The development of irradiation techniques: IMRT and VMAT, effected in changing dosimetric verification techniques. These advanced techniques raise various challenges in accurately measuring commissioning data and ensuring quality assurance (QA) of radiation dose distributions. Comprehensive description on VMAT and IMRT dosimetry in contained in AAPM Report No. 120 – "Dosimetry tools and techniques for IMRT" [49] and guidelines for the verification of IMRT published by ESTRO in booklet 9 from 2008 [50] .

Film dosimetry is adequate for measurements of small and complicated apertures but nowadays is commonly replaced with flat and cylindrical multidetector arrays. The methods and the principles of quality control of individual dynamic treatment have been described in the international documents AAPM and ESTRO [51].

3.6 PLANAR DOSIMETRY IN RADIOTHERAPY

Radiochromic Films

At the beginning of IMRT, most medical physicists were restricted to the use of point detectors and radiographic film. Radiochromic films stand out as one of the most versatile types of 2D dosimeters in the medical field, particularly for conducting patient-specific dose verification and routine quality assurance tests in the realm of radiotherapy [52] [53].

Radiochromic films offer numerous advantages over the limitations of conventional dosimeters. Their immediate colorimetric response to radiation, coupled with high spatial resolution and ease of application, positions them as a standard dosimetry tool in the field of radiotherapy. [54].

The primary benefit of radiographic film used to be high spatial resolution. However, it was challenging to use radiographic film for comprehensive measurements because of the need for adequate mixing of chemicals, time considerations [55] [49], and required supplemental measurements with an ion chamber.

Currently, the most frequently used radiochromic film products for dose verification in external beam therapy are EBT-2, EBT-3 and EBT-4, originally manufactured by the International Specialty Products (ISP, Wayne, NJ), which is now the part of Ashland (Bridgewater, NJ) [56].

Gafchromic EBT-3 and EBT-4 are designed for measurements of absorbed doses of ionising radiation. It is particularly suited for high-energy photons. The dynamic range of this film is from 0.1 to 20 Gy but it performs best in the 0.2 to 10 Gy dose range making it suitable for many applications in IMRT, VMAT and brachytherapy [57].

The film is comprised of an active layer, nominally 28 μm thick, sandwiched between two 125 μm matte-polyester substrates. The active layer contains the active component, a marker dye, stabilisers, and other components giving the film its near energy-independent response. The thickness of the active layer will vary slightly between different production lots.

The specification of the film used is as follows (Table 1):

Table 1 Gafchromic EBT-3 Film selected properties.

Dynamic Dose Range	0.1 to 20 Gy
Energy dependency	<5% difference in net optical density when exposed at 100 keV and 18 MeV
Dose rate response	<5% difference in net optical density for 10 Gy exposures at rates of 3.4 Gy/min. and 0.034 Gy/min.
Uniformity	Better than ±3% in sensitometry response from mean

Electronic Arrays

Various options exist for 2D used in external beam dosimetry, chosen for their user-friendly nature, instant readout, and analytical capabilities. The two primary classes are diode arrays and ionisation chamber arrays, both designed to be positioned within a solid phantom for dose measurement and verification.

2D ion chamber detectors are widely used in radiotherapy dosimetry because of superior dosimetric characteristics and convenience of data readout, but they suffer from low spatial resolution. The high cost limits the number, size, and arrangement of detectors [58] [59]. An insufficient spatial resolution may affect the penumbra of the measured profiles in wider photon fields, and it can also affect a narrower photon field's centre dose. This can lead to limited sampling of the radiation beam in regions of high dose gradients. Under-sampling negatively influences the measurement precision and, subsequently, the accuracy of the reconstructed volumetric dose.

Diode arrays are favoured for point measurements, offering localised dose assessments, but they may have limitations in spatial resolution. On the other hand, ionisation chamber arrays

provide a volumetric perspective with the volume-averaging effect leading to a blurred dose measurement. However, this effect also means that more of the radiation fluence pattern is sampled during the measurement.

When evaluating dose distributions, a combination of measurement types, often involving both array measurements and ion-chamber point measurements, is frequently employed due to the advantages and disadvantages inherent in each type

A critical consideration for all measurement arrays is the detector response's variation with irradiation angle. Virtually all these devices exhibit some degree of angular dependence. In the case of 2D systems, the detector array can be irradiated either perpendicularly (e.g., with the detector on the couch top or mounted to the gantry), or an angular correction can be applied if the measurement results can be correlated with the gantry angle. The necessity for an angular correction factor should always be assessed, especially if the measurement geometry involves beams with non-perpendicular incidence, as emphasised by studies [60] [61] . This assessment ensures accurate and reliable dosimetry in diverse clinical scenarios.

In the field of radiotherapy, the advent of novel Stereotactic Radiosurgery (SRS) arrays has marked a significant advancement. These high-resolution arrays have been designed to address the complex challenges associated with small field dosimetry. These novel SRS arrays are poised to revolutionise the field of radiotherapy, offering unprecedented precision and accuracy in dose delivery, thereby enhancing the efficacy of treatment and patient outcomes. This next-generation SRS arrays are mainly utilised by radiation therapy department for patient-specific quality assurance stereotactic radiosurgery and stereotactic radiotherapy [62].

3.7 THE TREATMENT PLANNING SYSTEM

The treatment planning system is software dedicated to dose computation relative to target volumes and OARs. The optimisation process is a crucial step when delivering a modulated treatment plan such as IMRT or VMAT. Dose computation is based on a set of dose values to be delivered for each delineated volume on the reference CT scan. This involves the specification of dose values for target volumes as well as the maximum dose limit for OARs. The software then iteratively modifies the beam intensities to achieve the expected result.

The dynamic plan dose is calculated by dividing the geometry into a number of discrete sets called control points. To produce a satisfactory dose plan, it is necessary to optimise the field shapes and beam intensities from a large number of gantry angles. However, the field shapes

are limited in that the MLC leaves must be able to move to their new positions within the time required for the gantry to rotate between control points. On the other hand, the greater the number of gantry angles sampled, the more difficult it is for the TPS to optimise within the MLC leaf motion constraints. Sometimes, for highly modulated plans, the optimised plan cannot meet the initial dose constraints. In this case, the physicist and the physician decide whether the plan is still acceptable or whether some constraints need to be modified. If important OARs are involved, such as the spinal cord, it is at times necessary to lower the total dose of the treatment to prevent radiation damage from occurring. The TPS software we used for the computation of the calculated treatment plans is Elekta Monaco, installed at the radiotherapy division at Katowice Oncology Centre (Katowice, Poland). Monaco's VMAT functionality can optimise single or multiple non-coplanar arcs simultaneously, providing the flexibility and control needed for complex treatment plans such as VMATs. Monaco offers the XVMC Monte Carlo dose engine, for electron and photon, for a continuous arc calculation as a single beam, rather than just dose approximations that occur with many discrete (control point) gantry angle positions.

When the optimisation process finishes, the validated plan is exported to the accelerator's control software, Mosaiq, and can be delivered.

3.8 A PATIENT-SPECIFIC QUALITY ASSURANCE

In recent times, the intricacy and sophistication of clinical treatment planning and treatment planning systems have notably advanced, especially with the incorporation of three-dimensional treatment planning systems, the adoption of conformal treatment planning, and delivery techniques. Consequently, there is a growing demand for a comprehensive set of quality assurance (QA) guidelines applicable to clinical treatment planning. Since each treatment plan is individual for each patient it is often referred to as patient-specific quality assurance.

Assessing the quality of a treatment plan is a crucial step in the radiotherapy treatment workflow. It is essential to understand the plan quality and to be aware of the parameters influencing it. In the context of radiotherapy, plan quality refers to the clinical suitability of the delivered dose distribution realistically anticipated from a treatment plan. Plan quality is typically evaluated by examining the dose distribution calculated by the treatment planning system. However, assessing the 3D dose distribution is challenging, given the difficulty in fully

evaluating its spatial characteristics and the current limitations in personalising predictions of clinical outcomes based on individual patient characteristics.

Moreover, the calculated dose distribution may not precisely represent the dose delivered to the patient due to uncertainties in dose calculation and treatment delivery, including machine performance and variations in patient setup and anatomy. Consequently, plan quality is also influenced by the robustness and complexity of the treatment plan. The scope of the QA requirements for treatment planning is quite broad, encompassing an image-based definition of patient anatomy, 3D beam descriptions for complex beams including multileaf collimator apertures, 3D dose calculation algorithms and complex plan evaluation tools including dose volume histograms.

Examining the calculated dose distribution is a foundational aspect of plan evaluation, ensuring the attainment of high plan quality throughout the treatment planning process and upon treatment approval. However, this evaluation is inherently complex due to the various factors that typically contribute to the assessment of plan quality. These factors encompass protocols, local requirements, historical practice, and personal preferences, collectively influencing the ultimate decision-making process.

Several reports have been written regarding recommendations on QA for IMRT and VMAT plans [63] [64]

In VMAT, the number of parameters can be varied to achieve intensity modulation volumetrically. These include: (i) the MLC aperture shape, (ii) the dose rate and (iii) the gantry rotation speed. This increased complexity of clinical treatments raises the need for more accurate dose verification systems and procedures.

Conventional pre-treatment verification typically encompasses point dose measurements with ionisation chambers and fluence measurements utilising films or 2D array detectors. This process typically involves creating a verification plan in the TPS with beam parameters identical to those in the patient's plan, which is then administered in a phantom geometry. The measured dose plane in the phantom is subsequently compared to the calculated dose using gamma evaluation, initially introduced by Low et al. [28] [65].

IMRT and especially VMAT treatments are far more complex than those of traditional radiotherapy, thus periodical checks on the accelerator and other equipment are no longer sufficient to assure a reliable QA. Medical physicists are then required to carry out pretreatment measures to make sure that eventual dose discrepancies between the prescribed plan from the TPS and measurements are clinically acceptable.

3.9 GAMMA INDEX

The Gamma Index (γ, GI) is a mathematical equation used in radiotherapy for comparing two dose distributions. It combines two key parameters: the dose difference (DD) and the distance-to-agreement (DTA). The Gamma Index is calculated for each point in the dose distribution. The global Gamma Index analysis calculates the DDs relative to the maximum dose (or prescription dose), while the local Gamma Index analysis calculates the DDs relative to the doses at each evaluated point.

The equation to calculate Gamma Index is as follows:

$$\gamma = \sqrt{\left(\frac{\Delta D}{DD}\right)^2 + \left(\frac{\Delta r}{DTA}\right)^2}, \tag{6}$$

where *ΔD* is the dose difference at a specific point, *DD* is the dose difference criterion, *Δr* is the distance between the evaluated point and the point in the reference distribution with the same dose and *DTA* is the distance-to-agreement criterion.

The Gamma Index is typically represented graphically with an ellipse or ellipsoid around a point in the measured distribution, where the principal axes are defined by the gamma criteria [28]. The interpretation of the Gamma Index results is based on the value of GI. The value of 1 or less is generally considered acceptable, indicating that the measured dose distribution is within the predefined DD and DTA criteria of the calculated dose distribution.

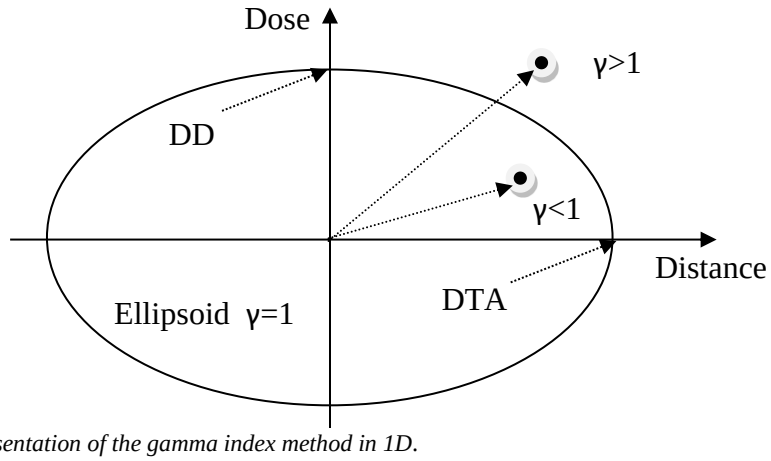

Figure 4 Schematic representation of the gamma index method in 1D.

Gamma Index can be also calculated in reference to a local dose value instead of a dose maximum. The local Gamma Index indicates percentage dose differences with reference to the local dose at each point. This method is very useful for highlighting dose differences throughout the distribution, although it has the potential disadvantage of over-emphasising large percentage dose differences at comparatively low dose points [66].

The Gamma Index is a fundamental concept in the field of radiotherapy, playing a pivotal role in patient-specific quality assurance. It is defined as a quantitative measure that combines two key parameters: the dose difference and the distance-to-agreement. This combination allows for a comprehensive evaluation of the agreement between calculated and measured dose distributions. In the context of 2D measurements, the Gamma Index becomes particularly significant. It effectively maps the spatial dose distribution on a plane, thereby providing a detailed overview of the treatment plan's accuracy. This is especially crucial in complex treatment plans such as intensity-modulated radiation therapy and volumetric modulated arc therapy (VMAT), where precision is paramount. Thus, the Gamma Index serves as an indispensable tool in ensuring the efficacy and safety of radiotherapy treatments.

In the realm of radiotherapy, the Gamma Index serves as a quantitative metric that assesses the congruence between the planned and actual delivered dose distributions. The interpretation of the Gamma Index results is as follows:

- A Gamma Index value that is equal to or less than 1 is typically deemed acceptable. This indicates that the measured dose distribution aligns with the calculated dose distribution within the predefined dose difference and distance-to-agreement criteria.
- A Gamma Index value exceeding 1 signifies a deviation between the measured and calculated dose distributions beyond the acceptable threshold. Such discrepancies could be attributed to a multitude of factors, including machine error, patient movement or inaccuracies in calculation.
- The percentage of points with a Gamma Index value of 1 or less, often reported as the "% of points passing," is another commonly used metric to evaluate the quality of a treatment plan. A higher percentage suggests a better agreement between the measured and calculated dose distributions.

It is crucial to note that the interpretation of Gamma Index results may depend on the specific clinical context and the standards set by individual clinics. Therefore, any Gamma Index analysis should be interpreted in conjunction with other QA measures and clinical judgment.

Gamma index passing criteria is a subject of discussion. In Japan the most popular is 3%/3mm, threshold 10% and passing rate 95% [67]. Commonly used criteria are in range analysis of 5-3%/3-2mm, threshold 10% with passing rate 90-95% [68] [69] [70] - typically 3%/3mm with threshold 10% and passing rate 95% [71]. Extensive discussion of this parameter is enclosed in AAPM TG 218 report [72] where on pages 67-68 there is a literature summary of 22 publications containing IMRT QA measurement results reported in the literature. Depending on the test parameters adopted, the tools available and the techniques used in the various radiotherapy centres, around 90% of the plans pass the test [70]. However, some publications recommend narrowed Gamma Index evaluation criteria for VMAT due to better error detection [73] [74].

The AAPM Task Group No. 218 (TG-218) report among all recommendations provides for patient-specific intensity-modulated radiation therapy (IMRT) quality assurance (QA). Here are the two limits:

- Tolerance Limits:

The tolerance limits define the acceptable range for IMRT QA processes. They indicate when the process is considered stable and unchanged. TG-218 proposes a 3%/2 mm gamma analysis threshold for evaluating discrepancies between calculated and delivered doses in QA. The universal tolerance limit for the gamma pass rate is 95%.

- Action Limit:

The action limit sets a minimum level of process performance. If IMRT QA measurements fall outside this limit, it could negatively impact the patient. TG-218 specifies an action limit of 90% for the gamma pass rate.

3.10 PLASTIC SCINTILLATORS

Scintillating materials which include organic, inorganic, and organometallic types, emit visible light upon excitation—a phenomenon known as luminescence. Photoluminescence, induced by visible photons, leads to fluorescence and phosphorescence. Fluorescence arises from directly photoexcited states, while phosphorescence involves forbidden transitions from other excited states.

When scintillating materials are excited, various phenomena occur. Quenching, non-radiative de-excitation competes with light emission. Excitation methods vary: photoluminescence (visible photons), triboluminescence (friction and electrostatic forces), sonoluminescence

(ultrasound), and thermoluminescence (heating). In dosimetric applications, ionising radiation-induced luminescence is called radioluminescence or scintillation.

Organic fluors, such as Anthracene, Naphthalene, and 3-Hydroxyflavone, emit light due to their distinctive electronic structure. Organic scintillators fall into three categories: unitary (pure crystals), binary (scintillator in a solvent), and ternary (primary scintillator with a wavelength shifter).

At the molecular level, luminescence involves π-electrons. These less tightly bound electrons transition within the π-electronic absorption band, requiring less energy than σ-electrons.

When molecules receive sufficient excitation energy, they transition to π-electronic singlet states. Each state corresponds to multiple vibrational levels, differing in energy by approximately 0.15 eV. Although a molecule can be excited to any of these levels, a significant proportion tends to occupy the S10 state (where 1 represents the first excited state and 0 denotes the ground vibrational energy level for this state). This preference arises because states with excess vibrational energy rapidly dissipate it within approximately 10^-12 seconds to achieve thermal equilibrium. Refer to Figure 5 for a schematic representation of the energy levels in the Jablonski diagram.

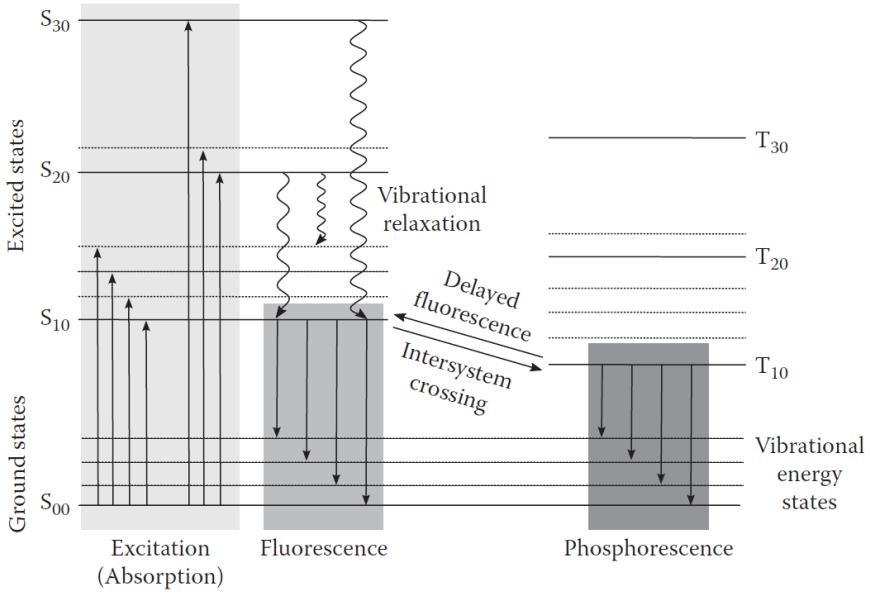

Figure 5 Jablonski diagram presenting the π-electronic atomic levels of organic molecules. [75]

While other excitation processes exist, their contribution to fluorescence emission remains minimal. Excitation can lead to the ionisation of π-electrons, with subsequent ion recombination primarily observed in triplet states, contributing to a slower component of scintillation light

(75%). Some molecules also undergo ion recombination from singlet π-states, making a smaller contribution (12%) to scintillation [76]. It is theoretically possible to excite other electron-excited states (such as the σ-electron of carbon 1s electron), but the absorbed energy dissipates thermally, preventing fluorescence. Additionally, ionisation of electrons beyond π-electrons may result in temporary or permanent damage.

Primary de-excitation processes in unitary systems (consisting of a single type of molecule) include:

- Fluorescence: Arises from a singlet-singlet transition (S_{10} to S_{0x}), where x represents the vibrational level number.
- Internal conversion: A nonradiative transition between two energy levels of the same multiplicity.
- Non-radiative migration: The energy of the first singlet state migrates nonradiatively through exciton diffusion from one molecule to another before emission.
- Internal quenching: Occurs when the energy of the first excited singlet state dissipates nonradiatively via quenching transitions (toward S_{0x} or intersystem crossing toward T_{1x}).
- Intersystem crossing (ISC): Leads to phosphorescence or delayed fluorescence. ISC involves radiationless transitions facilitated by spin-orbit coupling
- Radiative migration: Fluorescence photons are absorbed by other molecules
- Vibrational energy conversion: Rapid (10^{-12} s) compared to S_1 to S_0 transition (10^{-9} s), concluding with vibrational relaxation to the first singlet state level (e.g., $S_{13} \rightarrow S_{11} \rightarrow S_{10}$).
- Phosphorescence: Electron transitions from absorption singlet band to triplet state (T_1), de-exciting into vibrational levels of the singlet ground state and emitting visible photons. Reversion from T_1 to S_1 produces delayed fluorescence if energy difference is small and T_1 level has a sufficiently long lifetime (10^{-6} s or longer).

Self-absorption

Both absorption and emission processes exhibit spectra reflecting the vibrational spacing in the associated singlet state. The S_1 level's spacing corresponds to the absorption spectrum, while the S_0 spacing relates to the emission spectrum. Typically, these spectra mirror each other due

to the similar distribution of vibrational levels in both ground and excited states (see Figure 6). The initial absorption band's maximum and the fluorescence spectrum's peak for the same electronic transition are separated by the Stokes shift— the distance measured in terms of wave numbers, wavelength, frequency, or energy between the peaks.

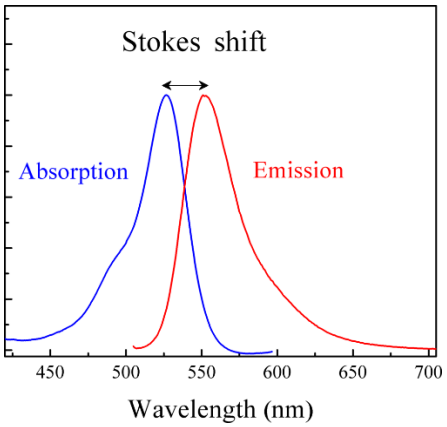

Figure 6 Image of absorption and emission spectra (Wikipedia).

An intriguing feature of organic scintillators is that nearly all fluorescent transitions have lower energy (longer wavelength) than the excitation energy, rendering the scintillator mostly transparent to its own emission spectrum. However, overlap between absorption and emission spectra can occur due to molecular thermal motion, providing additional energy for alignment. Minimising this overlap is crucial, and observing fluorescence at cryogenic temperatures can help mitigate it. Ideally, well-distinguished spectra with a large Stokes shift are preferred to minimise self-absorption, as discussed earlier in the context of radiative migration.

Light emission

The light emission from organic scintillators depends on various factors related to the scintillator's nature. When examining the properties of organic scintillating materials, a range of spectral bands and response times can be observed. Each material exhibits its distinct exponential decay of fluorescence intensity over time. The response of organic molecules to excitation depends on the scintillator's nature, the type of ionising particles (whether directly or indirectly ionising) and the energy of the incident particles. These dependencies can be strategically utilised in applications such as pulse shape discrimination.

Furthermore, the scintillator's light response is impacted by the extent of damage it incurs. This damage can result from prolonged exposure to ionising radiation, exposure to light and oxygen (leading to polymer degradation in the case of plastics), or surface cracking that compromises internal total reflection—a phenomenon crucial for the transmission of scintillation light.

Organic solution scintillators require a finite time (τ_R) to reach their peak scintillation response, approximately on the order of $10^{\wedge-9}$ seconds. Both types of scintillators exhibit a signal falloff characterised by the decay time (τ), typically in the range of 10^{-8} to 10^{-9} seconds [77]. This decay time represents the duration for a relative loss of 1/e, depicting an exponential decay in light intensity for fluorescence. The general formula expressing intensity over time is described by the equation:

$$n(t) = \frac{N}{(\tau - \tau_R)}\left[e^{-t/\tau} - e^{-t/\tau_R}\right], \tag{7}$$

where *n(t)* is in photons per second, and *N* represents the number of excited states.

In the case of plastic scintillators, assuming that the rise time is much faster than the decay time, we simplify the expression to:

$$n(t) = N \cdot f(\sigma, t) \cdot e^{-t/\tau}, \tag{8}$$

where $f(\sigma,t)$ is the Gaussian function with a standard deviation σ.

Light yield

When a scintillator absorbs energy, only a small portion of it is converted into light, while the majority dissipates nonradiatively. The efficiency of this conversion process is quantified by the absolute scintillation efficiency. Specifically, the absolute scintillation efficiency represents the fraction of the initially deposited energy in a material that contributes to scintillation light. Anthracene, with a scintillation efficiency of 5% in the blue region of the visible spectrum, serves as a calibration reference for other organic scintillators due to its practical effectiveness.

Typical plastic scintillators exhibit light yield values ranging from 40% to 65% of anthracene, while liquid scintillators achieve even higher light efficiency, exceeding 60% and reaching almost 80% of anthracene [78] [79].

Scintillation efficiency can also be expressed in terms of the number of photons produced per unit of absorbed energy (MeV). For example, the datasheet for the BCF-12 scintillating fibre indicates the emission of 8000 photons in the range of 400–575 nm (average of 432 nm) per MeV. This corresponds to a W/e equivalent value of 125 eV per photon (according to the Saint-

Gobain Scintillation Brochure). Additionally, scintillation efficiency varies based on the particle type and energy. Electrons tend to elicit a stronger response compared to heavier particles like protons and alpha particles at equivalent energies [80].

Regarding quenching effects, discussions have highlighted their impact on reducing scintillation efficiency. Quenching occurs when energy is dissipated non-radiatively, resulting in a high ionisation density along the particle's track within the scintillator. The relationship between the fluorescent energy emitted per unit path length (*dL/dx*) and the specific energy loss for the charged particle (*dE/dx*) is described by the scintillation efficiency (S):

$$\frac{dL}{dx} = S\frac{dE}{dx}. \tag{9}$$

Theoretically, organic scintillators exhibit linear responses for particle energies above 100 keV [81]. However, in practice, deviations from ideal linearity occur, especially at lower energies. These deviations are attributed to quenching effects. Birks proposed a modified expression that accounts for the density of damaged molecules (proportional to ionisation density) and a proportionality constant (*B*). In the presence of quenching, the expression for fluorescence emission becomes:

$$\frac{dL}{dx} = S\frac{\frac{dE}{dx}}{1+kB\frac{dE}{dx}}, \tag{10}$$

where *k* represents the fraction of molecules undergoing quenching. This equation is commonly known as the Birks formula.

Quenching

Accurate dosimetry requires the understanding of the relationship between the energy deposited in a medium by a radiation source and the resulting signal detected. In scintillators, the conversion of radiation energy into visible light depends on the interaction mechanism of the radiation and the radiation quality (as defined by ICRU 1970).

The response of organic scintillators is influenced by the ionisation density of incident radiation, often expressed as linear energy transfer (LET). In therapeutic photon beams, where ionisation density is generally uniform, scintillation light emission correlates directly with the radiation dose at any given location. However, in proton and heavy ion beams, increasing ionisation density with depth leads to reduced scintillation response—a phenomenon known as quenching. Other detector types, such as films, silicon diodes, thermoluminescent and optically stimulated luminescent detectors, alanine, diamond, and polymer gel detectors, also exhibit LET-dependent quenching [82, 83].

Quenching in proton and heavy ion beams, reducing the efficacy of scintillator detectors for dose distribution measurements, and despite their potential benefits, the development of LET-independent scintillator materials is still a challenge due to limited knowledge of the quenching processes.

Interestingly, the impact of the quenching process in plastic scintillators for MV photon beams is negligible [84] [85].

Plastic scintillator properties

The pursuit of water equivalence drives the use of Plastic Scintillator Detectors (PSDs) in radiation detection. An ideal dosimeter should closely resemble the medium where absorbed doses are measured, allowing charged particles to interact within the detector similarly to their interactions within the medium. This alignment ensures accurate recording of energy deposited by ionising radiation, making water-equivalent detectors highly desirable.

Achieving water equivalence involves matching the constituent materials in a detector to the absorption and scattering properties of water across a clinically relevant energy range. A typical PSD consists of a radiation-sensitive material surrounded by a protective wall.

Scintillator parameters related to Compton scattering, mass energy absorption coefficients, mass collision stopping powers, and mass angular scattering powers, exhibit good water equivalence, especially for energies above 100 keV. Figure 7 illustrates the mass energy absorption coefficients, mass collision stopping powers, and mass angular scattering powers for incident photons and electrons, highlighting the well-matched physical characteristics among these three materials.

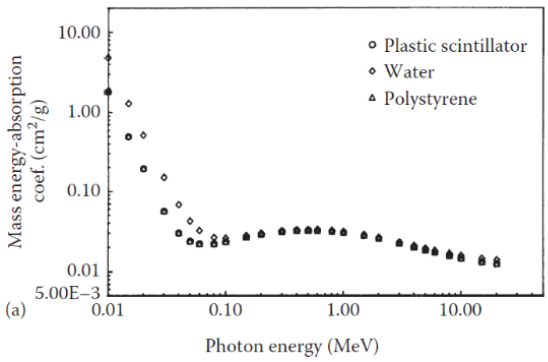

Figure 7 Mass energy absorption coefficients for plastic scintillator compared to water and polystyrene as a function of photon energy [86].

The polarisation or density effect, related to the density states of detector constituents, significantly influences radiation interactions. Plastic scintillators, which maintain the same density state for both the wall and detector volume, exhibit homogeneous polarisation. This property ensures water equivalence without disturbing the radiation field.

3.11 DOSIMETRIC CHARACTERISTICS OF ORGANIC SCINTILLATORS

Essential physical parameters relevant to dosimeter materials in radiotherapy are [75]:

- Water Equivalence: This parameter considers how the dosimeter material responds to radiation compared to water. It also accounts for the dosimeter's presence in a homogeneous water medium and its impact on radiation fluence.
- Energy Dependence: This assesses how variations in the energy spectrum of the radiation beam influence dosimeter measurements.
- Temperature Dependence: We examine how changes in ambient temperature affect the dosimeter's response.
- Resistance to Radiation-Induced Damage: This parameter reveals how the dosimeter material's sensitivity or output degrades with absorbed dose.
- Angular Dependence: Understanding this parameter helps account for variations in orientation between the dosimeter and the radiation beam, ensuring accurate and reliable dosimeter performance in radiotherapy applications.

Water equivalence

In the field of medical dosimetry, water has consistently served as the preferred reference material and surrogate for living human tissue. As a result, routine quality assurance measurements are commonly performed in homogeneous water environments. The degree to which a dosimeter is water-equivalent becomes crucial in minimising the perturbation of radiation fluence caused by the dosimeter's presence in a water tank during these measurements.

Several physical parameters come into play when quantifying the water or tissue equivalence of a dosimeter material, depending on the characteristics of the radiation field. For low-energy X-rays typically used in diagnostic applications, the effective atomic number (Z_{eff}) emerges as a key parameter for describing the water equivalence of a compound material. Z_{eff} is defined as a critical factor in evaluating how well a dosimeter material replicates the radiation interactions

observed in water or living tissue. This consideration is fundamental for ensuring the accuracy and reliability of dosimetry measurements in medical applications.

$$Z_{eff} = \sqrt[m]{a_1 Z_1^m + a_2 Z_2^m}, \tag{11}$$

where the exponent *m* represents an energy-dependent parameter. Its value varies from 3 to 4 for kilovoltage range X-rays and reduces to 1 for megavoltage range X-rays. The atomic number "*Z*" corresponds to a specific element, while "*a*" signifies the element-specific ratio of electrons to the total number of electrons [87].

Another quantifiable factor governing the water equivalence of a dosimeter material is the mass-energy absorption coefficient (μ_{en}/ρ). This coefficient describes the material's ability to absorb energy per unit mass when exposed to photon irradiation of a specific energy.

$$\frac{\mu_{en}}{\rho} = \frac{\mu_{en}}{\rho}\frac{\bar{E}_{ab}}{h\nu}. \tag{12}$$

In the case of megavoltage X-rays delivered during radiotherapy, Compton scattering serves as the predominant interaction mechanism between indirectly ionising radiation and the absorbing medium. In this energy range, the mass-energy absorption coefficient (μ_{en}/ρ) emerges as a potentially more representative measure of water equivalence than the effective atomic number (Z_{eff}). This preference is attributed to the fact that the cross section for Compton scattering exhibits less dependence on the atomic number compared to photoelectric absorption, which dominates at diagnostic energies.

According to ICRU (1984), favourable agreement between polystyrene and water is found when comparing mass-collision stopping powers for monoenergetic electrons in the 1-50 MeV range.

Energy dependence

The dosimetric response of organic scintillators is influenced by the energy of the incident ionising radiation. The energy of the incident radiation affects the efficiency of the scintillation process in the organic scintillator. Different types and energies of ionising radiation may lead to variations in the scintillation efficiency, impacting the amount of emitted light in response to radiation interactions within the scintillator material. The energy of the incident radiation also plays a role in determining how well the organic scintillator mimics the dose absorption characteristics of a reference material, typically water. This aspect is crucial for accurately

measuring and quantifying absorbed doses, especially in medical dosimetry applications where water is often used as a reference medium.

Scintillation efficiency

For various commercial organic scintillators based on polystyrene and polyvinyl toluene the results indicated that the sensitivity of all scintillators remained nearly energy-independent within a 5% tolerance for electron energies exceeding 100 keV and photon energies above 200-250 keV [88] [89].

Organic scintillators exhibit reduced sensitivity to low-energy ionising radiation, a phenomenon commonly known as “quenching”. This effect arises due to the high ionising density associated with low-energy charged particles or photons. When radiation energy is deposited within a small volume, the scintillator matrix experiences quenching effects.

While quenching is less significant in the primary radiation field, it becomes relevant for measurements outside the field. In such scenarios, contributions from low-energy scattered photon radiation play a substantial role. Understanding and accounting for quenching effects are critical for accurate dosimetry, particularly when dealing with low-energy ionising radiation.

Dose absorption

The response of polyvinyl toluene-based organic scintillators to higher-energy photons has been investigated using Burlin cavity theory [86] [90] and Monte Carlo simulations [91]. According to the Burlin cavity studies, there was a 0.8% change in the ratio between absorbed dose to the scintillator and absorbed dose to water for photon energies ranging from 200 keV to 20 MeV. Similarly, the Monte Carlo study found a change within 1.0% for energies spanning from 500 keV to 20 MeV.

These investigations, combining theoretical models and computational simulations, provide valuable insights into how polyvinyl toluene-based organic scintillators behave when exposed to photons across a wide energy spectrum. Understanding these responses is essential for accurate dosimetry applications involving higher-energy photons, such as those used in medical and industrial contexts.

Temperature dependence

The temperature dependence of polyvinyl toluene-based organic scintillators was investigated by researchers [86] [92]. The results showed that with temperatures ranging from 0 to 50°C the scintillator exposed to megavoltage X-rays shows no or low (of 0.1%/°C) difference from overall measurement uncertainty. Consequently, it was concluded that the scintillator probe under examination could be considered temperature-independent within a clinically relevant temperature range.

Resistance to radiation-induced damage

Radiation-induced damage is characterised by a decrease in scintillator light output with absorbed dose. This effect can be either permanent or non-permanent. Publications show a decrease in sensitivity for the polyvinyl toluene-based scintillator which were studied when exposed to substantial doses [86]. After a total delivered dose of 10 kGy, a sensitivity reduction of 2.8% was measured. It can be explained that the decrease in scintillator sensitivity is attributed to the non-permanent formation of absorption centres in the polystyrene [93]. These centres appeared to form primarily in the visible blue area, with a significant overlap between the resulting absorption spectrum and the emission spectrum of the scintillator.

Angular dependence

An ideal dosimeter should exhibit ±0.5% independence [94]. However, in practice, most detectors lack isotropic response. To mitigate this, dosimeters are typically used in the same geometry as their calibration, aligning the dosimeter axis parallel to the gantry rotation axis.

Reported angular dependence of BC-400 scintillator during high dose rate dosimetry varied by no more than 2% for measurements not corrected for the stem signal [95] and 0.6% after correcting for the stem signal [96].

Steam effect

When a plastic like optical fibre or plastic scintillator is exposed to ionising radiation, it generates light within the material itself. This phenomenon, known as the stem effect or stem signal, results in an amplified light signal from both the fibre and the scintillator probe. The term ‘stem’ refers to the supplementary light signal superimposed on the scintillator signal. Distinguishing the scintillator signal from the parasitic signal becomes challenging due to the

stem effect. Consequently, using organic scintillators in radiotherapy dosimetry faces a significant challenge, primarily due to a reduction in the signal-to-noise ratio.

Furthermore, the amount of light emitted by the plastic depends on the quantity present in the radiation field. This dependency introduces systematic errors, especially when there are substantial changes in field size or scintillator positioning relative to the radiation field. Managing the stem effect is crucial for accurate and reliable dosimetry measurements, particularly in the dynamic and varied environments of radiotherapy applications.

The stem effect arises from two main physical processes: fluorescence and Cerenkov radiation. Fluorescence, akin to scintillation, occurs due to impurities within the plastic. These impurity molecules absorb energy from charged particles and photons, subsequently emitting photons with a shifted wavelength (Stokes shift) during the de-excitation process

Cerenkov radiation occurs when a charged particle moves through a medium at a velocity exceeding the speed of light in that medium [97]. This phenomenon can occur for both charged particles and photon irradiation, with the latter resulting from secondary electron generation. When a charged particle passes through a dielectric material, it momentarily alters the electromagnetic field in the vicinity of its track. This interaction polarises the atoms within the medium. As the atomic electrons return to equilibrium and the atoms depolarise, radiation is emitted. Typically, the radiation wave fronts are out of phase, leading to destructive interference and cancelling out the net radiation, but if the particle's velocity exceeds the phase velocity of light in the medium (expressed as $v = c/n$) or ($n\beta > 1$), where (n) is the refractive index and β constructive interference occurs.

Cerenkov radiation is only produced for particles with energies surpassing a specific threshold, denoted as $E_{threshold}$:

$$E_{threshold}(keV) = \frac{511keV}{\sqrt{1-\left(\frac{v}{c}\right)^2}} - 511keV. \quad (13)$$

For most commercial plastic scintillators, this corresponds to an $E_{threshold}$ of approximately 180-190 keV. The Cerenkov radiation is dominant in the UV and visible blue wavelength areas, exhibiting a distinct $1/\lambda^3$ dependence. There is a Cerenkov cut-off in the X-ray wavelength area, since here n < 1. The radiation is emitted in a cone of angle$\theta = arcos(1/n\beta)$ relative to the propagation direction of the charged particle, as seen in Figure 8.

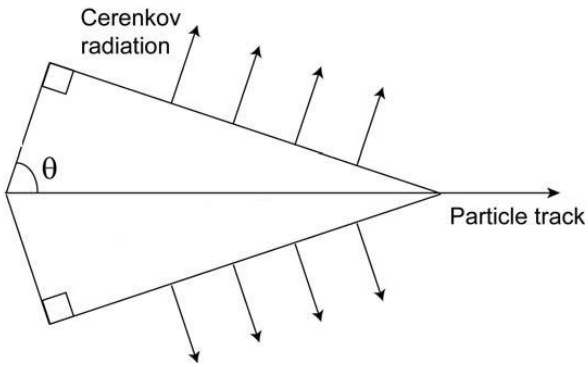

Figure 8 Schematic view of Cerenkov light generation in a dielectric medium. When a particle of velocity v > c/n traverses a medium of refractive index n, Cerenkov radiation is emitted in a cone of half angle θ with velocity c/n.

Cerenkov radiation was the dominant cause of the stem effect when using MeV electron beams, fibre fluorescence being negligible in comparison [75]. Significant research efforts have been dedicated to reducing or correcting the stem effect in fibre-coupled PSDs.

Cerenkov light removal

Several approaches have been explored, including:

Background Subtraction Fibre:

The use of a background subtraction fibre has been proposed as a method to mitigate the stem effect [86]. This technique involves subtracting the background signal introduced by the fibre from the overall signal, aiming to isolate the scintillator response.

Low-Pass Filtering of Violet-Peaked Cerenkov Light

Low-pass filtering of the violet-peaked Cerenkov light has been investigated as a means to reduce the stem effect [98]. This method involves selectively filtering out undesired components of the light signal, particularly those associated with Cerenkov radiation.

Temporal and Spectral Discrimination Methods

Temporal and spectral discrimination methods for Cerenkov removal have been explored with varying degrees of success [90]. These methods aim to distinguish and eliminate the unwanted Cerenkov contributions over time or based on their spectral characteristics.

Air-Core Light Guides

The use of air-core light guides as a replacement for traditional optical fibres has been proposed. This approach has proven to be promising, particularly in small-field external beam applications [92]. Air-core light guides offer potential advantages in minimising the stem effect and improving the overall performance of fibre-coupled PSDs.

These diverse strategies represent ongoing efforts to enhance the accuracy and reliability of dosimetry measurements in situations where the stem effect poses challenges.

The usage of mirrors and cameras is similar to air-core light guides. It eliminates the stem effect completely since there is no light guide used.

3.12 CMOS LIGHT DETECTORS

Charge-coupled devices, or CCDs, have traditionally been the main technology used in image sensors. However, recent improvements in the design of image sensors using complementary metal-oxide semiconductor (CMOS) technologies have led to their use in many popular products. This makes CMOS-based sensors a strong alternative to CCDs.

CMOS sensors are commonly found in commercial digital cameras. These sensors have become the go-to choice in the industry because they work well and are cost-effective. As digital cameras have gotten better over time, so have CMOS sensors. They now perform better, make less noise, and come with more features.

CMOS image sensors use the advanced integrated circuit technology found in microprocessors and memory chips. This shared technology enables the implementation of diverse circuits, offering virtually limitless possibilities for the functionality and complexity of CMOS sensors. However, despite this flexibility, many imagers adhere to a fundamental concept and possess a comparable architecture [99].

At the heart of the sensing component in a CMOS detector lies the photosensitive element, which can take the form of photogates, phototransistors, or photodiodes. A photodiode, which is most commonly used, is essentially a junction between a p-type and an n-type semiconductor, commonly referred to as a p-n junction. While a simple p-n junction suffices for light detection, a more sophisticated approach involves the use of a p-i-n junction with an intrinsic region positioned between the p-type and n-type regions, enhancing device efficiency [100]. CMOS

technology employs both P-channel and N-channel MOS transistors on the same silicon substrate.

The primary objective of any image sensor is to efficiently detect light. Both CCDs and CMOS-based imagers utilise the photoelectric effect of a semiconductor to convert photons into electrical charges. Unlike CCDs, CMOS sensors aren't restricted to using silicon as the detector material. Instead, various materials can be integrated with a CMOS readout integrated circuit (ROIC) to impart sensitivity to ultraviolet, visible, or infrared light [99]. Figure 9 compares the principle of CMOS sensors to that of CCDs. Both detector technologies use a photodiode to generate and separate the charges in the pixel.

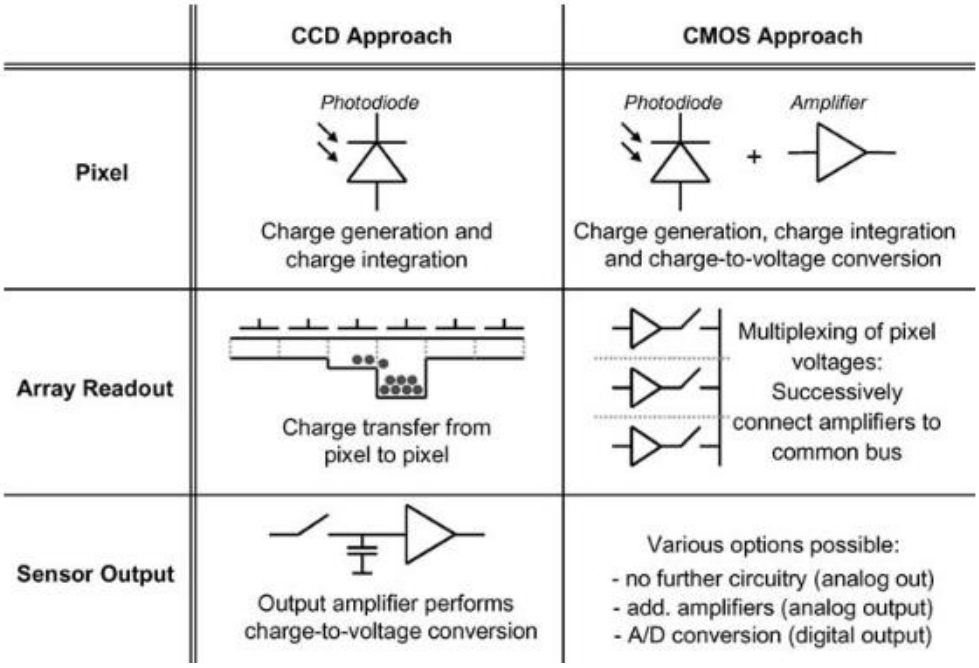

Figure 9 Comparison between CCD-based and CMOS-based image sensor approach [99].

In the readout process, CCDs transfer accumulated charge from pixel to pixel, progressing towards the perimeter. Ultimately, all charges are sequentially directed to a shared location (floating diffusion), where a single amplifier produces the corresponding output voltages. In contrast, CMOS detectors feature an individual amplifier in each pixel, known as an active pixel sensor (APS). This amplifier transforms the integrated charge into a voltage, eliminating the necessity for charge transfer between pixels. Instead, the voltages are multiplexed onto a common bus line using integrated CMOS switches.

The photoelectric effect is the foundation for creating an electronic image from a CMOS sensor. This effect happens when photons interact with p-n junction and create charged particles called hole-electron pairs.

Photons follow a pattern called Poisson statistics, which means there's an average number of photons collected over time, but the actual number can vary. This variation is the source of photon shot noise, which leads to uncertainty in measurements due to the discrete nature of photons.

A CMOS image sensor has many important parts that work together to create clear and accurate pictures. This sensor is made up of photosites, or individual pixels, that catch light. Each of these photosites has a pattern of red, green, and blue colour filters over it. This is called a colour filter array.

Noise

In CMOS sensors, the presence of noise, which can affect image quality, is inevitable. Various types of noise, such as shot noise, read noise, and dark current noise, can influence the performance of these sensors. The integration of noise reduction strategies is crucial to optimise sensor performance, once these noise sources are identified.

From a practical perspective among all sources of noise in CMOS sensor the only components that cannot be removed from an image with non-saturated pixels are the read noise, the image shot noise, and the dark shot noise.

The variability in the number of photons reaching the sensor's photodiodes gives rise to shot noise. This noise has a square root relationship with the signal, implying that shot noise becomes more noticeable as the signal increases [101]. By increasing the exposure time, which allows for the collection of more photons, the relative impact of this noise can be reduced.

Read noise, another factor to consider, is introduced during the charge-to-voltage conversion process or through the CMOS sensor's readout circuits. On-chip correlated double sampling, a common technique for mitigating read noise, is implemented. This measures the noise from the readout circuit and subtracts it from the actual signal, thereby improving the signal-to-noise ratio [102].

Dark current, an inherent characteristic of CMOS sensors, generates noise due to the thermal generation of electrons within the pixels. This noise increases with the duration of the exposure and the temperature of the sensor. To minimise dark current noise, temperature control methods can be used, such as cooling the sensor during long exposures, or employing dark frame subtraction. This involves capturing a dark frame (with no signal) and subtracting it from the actual image to compensate the effect of dark current.

Dark signal is closely related to temperature. At a certain temperature, it builds up at a constant rate. For instance, if the temperature remains stable, the dark signal will double if the exposure time is doubled. If the exposure time remains stable, a temperature change of about 5-6 °C can double the dark signal. When it comes to noise, the noise that comes from the dark signal has two parts: dark shot noise and dark fixed pattern noise. Dark shot noise, like the shot noise that comes with light, is calculated as the square root of the number of electrons generated by heat during the exposure period.

4 MATERIALS AND METHODS

4.1 PLASTIC SCINTILLATOR

The BC-400 plastic scintillator was chosen as radiation detector. BC-400 is general purpose and commonly used for detecting alpha, beta, and gamma rays, as well as fast neutrons. Scintillator was shaped in 100 mm × 100 mm with polished edges. Two usage of two thickness were initially investigated: 1 and 3 mm but after preliminary tests signal from 1 mm sample was sufficient so for all subsequent tests a one-millimetre thick sheet was used.

BC-400 properties [103] are presented below:

- Light Output: Approximately 65% of anthracene (for BC-400).
- Rise Time: Around 0.9 ns.
- Decay Time: Approximately 2.4 ns.
- Pulse Width (FWHM): About 2.7 ns.
- Wavelength of Max. Emission: 423 nm.
- Light Attenuation Length: Approximately 160 cm^2.
- Atomic Composition:
    - Hydrogen (H) atoms per cc: 5.23×10^{22}.
    - Carbon atoms per cc: 4.74×10^{22}.
- H:C atom ratio: 1.103.
- Electron density per cc: 3.37×10^{23}.
- Base Material: Polyvinyltoluene.
- Refractive Index: 1.58.
- Density 1.023 g/cm^3.

Spectral emission of BC-400 is depicted in Figure 10.

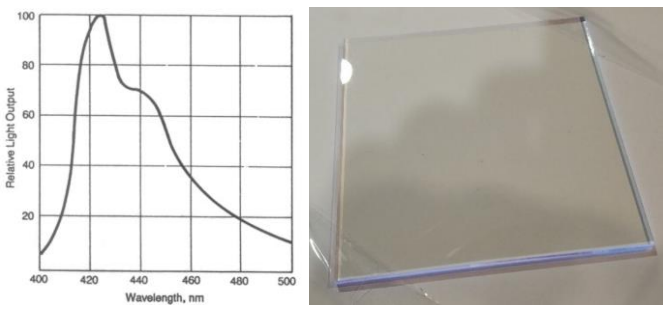

Figure 10 Emission spectrum of BC-400(left) and one of examined BC400 sheet (right).

This material is cost effective and represents a balance between performance and wavelength. A distinctive feature is the designation to detect >5MeV photon beams.

BC400 scintillator can be ordered directly from manufacturer or via distributors. During experiment setup assemble price was approximately 1000 € for 10 pieces of 100 mm × 100 mm.

4.2 CAMERA

The Pentax K-x CMOS camera was used for the experiment. This is an amateur digital SLR camera with the APS-C format sensor measuring 23.6 mm × 15.8 mm, manufactured by the Japanese company Pentax. The camera sensor is CMOS with 12.9 megapixels (effective resolution 12.4 megapixels), capable of storing 12 bits. Images are saved in RAW format at 4288 × 2848 pixels.

Table 2 Pentax K-x CMOS sensor physical properties [104] [105].

Pixel pitch	5.49 µm
Pixel area	30.14 µm²
Pixel density	3.32 MP/cm²
Sensor size	23.6 × 15.8 mm
Sensor resolution	4299 × 2885
Max. image resolution	4288 × 2428
Resolution	40- 50 lines per mm for *F* 16-5.6

According to expert reviews, this model has low noise compared to competitors for a similar value. [106].

The K-x interferes with RAW files during long exposures. Even when noise reduction is turned off, it automatically activates for exposures longer than 30 seconds. After each such exposure, the camera pauses for a period comparable to the exposure time to capture a dark frame and subtract it from the original. [106] [107].

The SMC-DA L 1:3.5-5.6 18-55 mm AL lens was used. The lens was set to a maximum focus of 55mm, giving a minimum aperture of *F* 5.6.

Captured images were stored on SDHC card in Pentax Electronic File (PEF) format. The K-x does not have a cable release socket, but it does work with an IR remote control.

4.3 SCINTILLATOR IMAGE PROCESSING

Images taken with the CMOS camera are stored in RAW format, specifically PEF. A PEF file is an uncompressed and unedited photo taken with a Pentax digital camera. It represents all the raw data captured by the camera, with each pixel storing 12 bits of RGB colour information.

For image processing with software such as MATLAB and ImageJ, the images had to be converted or developed into a commonly used format. The 16-bit TIFF format was chosen to avoid any loss of image quality. Digital Camera Utility Studio 5 (Pentax, Japan) was used to convert all the collected images into TIFF format.

The first step in image processing was to divide the images into three colour channels: red, green and blue. For each channel, outlier pixels were removed. The images were then denoised using a median filter and a Gaussian filter.

The median filter is a non-linear digital filtering technique often used to remove noise from an image or signal. It preserves the edges of the image while reducing the noise. The Gaussian filter, on the other hand, is a method used to blur images and reduce noise. It uses a Gaussian function, which is a natural choice for a blurring function because of its properties such as having no sharp edges. The combination of these two techniques helps to significantly reduce the noise in the images while preserving the important details, thereby improving the quality of the images for further analysis.

As the distance from the image's centre increased, vignetting led to a reduction in the signal value. Function $\frac{fl^4}{(fl^2+r^2)^2}$ where *fl* is the focal length and *r* is the radius from the image centre, was applied for correction of acquired images for vignetting.

During gamma analysis, the data were resized to match the TPS dose planes generated at maximum resolution, i.e. 1 mm × 1 mm. Bilinear interpolation was used, where the output pixel value is a weighted average of the pixels in the nearest 2 by 2 neighbourhood. Bicubic interpolation was not used, although it is a weighted average of pixels in the nearest 4-by-4 neighbourhood, because it can produce pixel values outside the original range.

Images for further analysis were registered to the corresponding dose plane generated by the treatment planning system. Multi-step monomodal registration was used. In the first step, rigid registration was used. In the second step, a non-reflective similarity transformation consisting of translation, rotation and scaling was applied. To avoid the influence of regions consisting

only of background during registration, a threshold equal to 2% of the maximum image value was used.

Schematic image preprocessing is shown in Figure 11.

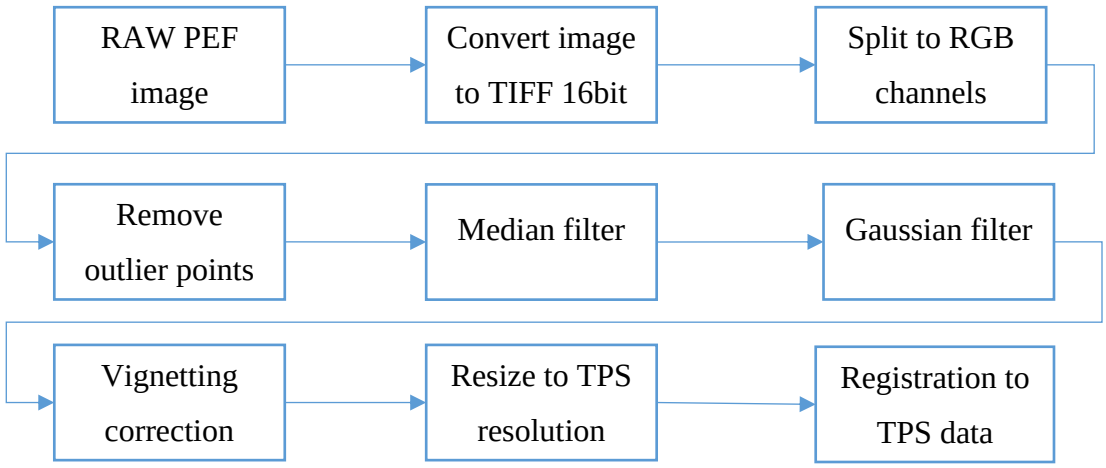

Figure 11 Applied plastic scintillator image processing.

4.4 PRELIMINARY TESTS

Despite efforts, the experimental setup has many variables and requires making numerous decisions during the construction phase. Some of these decisions have straightforward justifications, while others necessitate conducting a series of experiments to optimize the specified parameter. A significant portion of considerations on this topic can be found in the publication [108] which was published in June 2023 in the Polish Journal of Medical Physics and Engineering. The study aimed to validate whether the proposed measurement system could serve as a treatment plan verification tool for patients at the Radiotherapy Department of the Katowice Oncology Centre. Moreover, it lays the groundwork, indicating that a plastic scintillator sheet could serve as an inexpensive, high-resolution 2D detector for use in radiotherapy.

Various measurements have been made in relation to the use of plastic scintillators for dosimetry, including accuracy, precision, linearity, dose rate dependence, energy dependence, spatial resolution, physical size and readout convenience. In addition, parameters related to other parts of the system were investigated: the choice of image processing method, camera background measurements, optimal channel selection, measurements of scattered radiation and

shield selection. Additionally, the study allowed for the optimization of parameters such as camera sensitivity and aperture value. Another stage of the work involved verifying the independence of the detector's response with respect to dose rate and photon radiation energy. Ultimately, measurements were conducted to determine the relationship between the detector's response and the amount of radiation applied.

The experiments were conducted using the Saint Gobain BC-400 general-purpose plastic scintillator, which was shaped into 10 cm square sheets with a nominal thickness of 1 mm. Micrometre measurements indicated an actual thickness of 0.97 mm with a variation of ±0.01 mm, consistent with the tool resolution. The plastic scintillators were exposed to 6, 10, and 15 MV flattening-filtered (FF) and 6 and 10 MV flattening-filter-free (FFF) photon beams from the Elekta Versa HD linear accelerator.

The experimental setup involved placing the plastic scintillator at the isocentre on a table plane. PMMA build-up plates were added using the table extension frame. An acrylic mirror, chosen for safety and low UV absorption compared to mineral glass, was positioned directly beneath the detector. The camera, shielded with steel blocks, was placed perpendicular to the beam axis approximately 1 meter from the mirror. Linac laser adjustments ensured precise alignment with the scintillator center. The telephoto setting covered twice the detector size. All ambient light sources in the bunker were either turned off or covered. The source-to-surface distance was set to 98 cm and PMMA build-up was 2 cm. The measurement setup is shown in Figure 12.

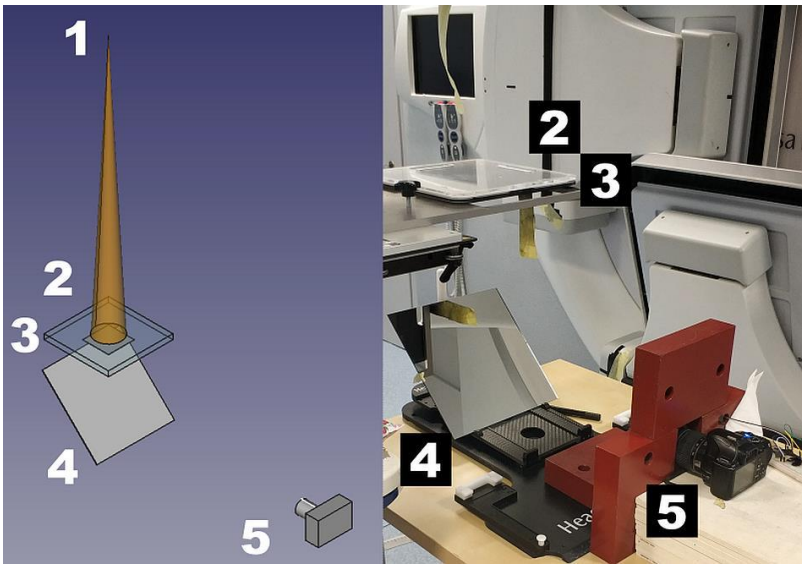

Figure 12 The system setup at the linac. Main elements on left schematic view: beam (1), build-up (2), PSD (3), mirror (4) and camera (5) [108].

In the experiments, the number of monitor units (MU) was utilized as a relative measure of dose rather than expressing the dose in Gray. The linear accelerator photon energies were calibrated such that the delivery of 1 MU corresponded to the dose of 1 cGy for the 10 × 10 cm^2 field size in water at the depth of 10 cm with the source-to-surface distance equal to 90 cm.

Data Processing and Signal Measurements

Each individual exposure was saved as a separate image in the Pentax Digital Camera Raw Image format (PEF), which is owned by the camera manufacturer Pentax. The images underwent batch conversion using the Digital Camera Utility 5 software (Ricoh Imaging Company, Japan). To preserve image quality, the uncompressed 48-bit TIFF format for further processing was chosen. The post-processing steps were carried out using the MATLAB environment.

Since the images had varying exposure times, the proportionally corrected background for time differences was applied. A selected region of interest (ROI) was consistently copied across all measurements within a series. To minimize human bias, the batch processing for data analysis was employed. Specifically, the mean and standard deviation of the ROI was calculated.

Signal and Background Measurements

The camera stores the measured signal in a single image across three colour channels. The BC-400 plastic scintillator used for measurements emits light primarily at 423 nm (blue light). The signal and background measurements to determine the optimal colour channel(s) for further analysis was conducted. Additionally, it was evaluated whether electronic noise is channel-independent and whether the camera sensor uniformly registers the background signal across all channels.

Lens-Derived Correction

The camera's built-in software performed lens-derived correction. Stray radiation artifacts, colloquially known as 'salt and pepper,' were effectively reduced using a median filter. The in-house automated script addressed vignetting, tilt and rotation, while also filtering and removing average background signal due to electronic noise and stray radiation before subsequent analysis.

Data Collection and Artefacts

Collected images contain background signal and artifacts, with sensor-derived artifacts encompassing background signal originating from ambient light, unshielded light sources, stray radiation and electronic noise from the camera sensor. Other artifacts can be categorized as lens-derived or scintillator-derived.

Background Signal and Electronic Noise Measurement

To prevent the collection of extraneous light, all light sources in the bunker were turned off or covered, allowing only scintillation-induced light. Electronic noise related to the camera sensor and exposure time was measured across various exposure times (10 to 90 seconds) and ISO settings (100, 200, and 400), with measurements conducted in the same bunker geometry as subsequent measurements to account for any residual background signal or light.

Stray Radiation

Stray radiation directly affects the camera sensor and contributes to additional noise, while the dependence of stray radiation signal on the delivered dose was measured using a scintillator detector removed from the setup, with doses of 10 to 1000 MU delivered using a 6 MV photon beam and a 15 × 15 cm² field size.

Linac Output Factor and Field Size Dependence

The linac output factor, influenced by phantom and head scatter components, was evaluated for different field sizes (3 × 3, 5 × 5, 10 × 10, 15 × 15, and 20 × 20 cm²), with camera settings (ISO 100, 200, and 400) and aperture (F = 4.5) adjusted accordingly.

Lens-Derived Artefacts

Lens distortion and vignetting are known artifacts. The camera's built-in firmware corrected distortion but did not handle vignetting properly. To mitigate vignetting, signal measurements were taken from a homogeneous light field and a correction function was fitted based on focal length and radius from the image centre.

Scintillator-Derived Artefacts

Scintillator-derived artifacts cause image blur and can be described by the point spread function (PSF). Modulation transfer function (MTF) calculations were performed at the edge of a 5 × 5 cm² field in the 'Y' direction, considering both penumbra size and detector blur.

4.5 PHANTOM

For doctoral research, a phantom was designed and built for PSD measurements. The following requirements and assumptions were taken into account when designing the phantom:

- **Mobility** The ability to place the phantom in the working position and fold it should not be complicated or take too much time.
- **Ability to place the phantom in the isocentre position** The distance from the radiation source to the PSD should be at least 100 cm within the possible range of table movement.
- **Ability to adjust geometry** Due to the experimental nature of the phantom, its construction must allow for adjustments of the PSD, CMOS camera, mutual distances, and angles. After adjustment, the positions should prevent accidental and unintended changes in position.
- **Radiation shielding** Minimizing scattered radiation reaching the CMOS matrix has a significant impact on image noise and matrix lifespan. The construction of the phantom must allow for the radiation shielding.
- **Cover from light** The construction of the phantom ensures the isolation of the camera from external light sources during exposure so that the measurement is independent of the lighting in the room.
- **Simple construction** The phantom cannot be overly complicated so that its construction and adjustment do not prolong experiments on the clinically used accelerator.

Cross section of the schematic phantom is shown in Figure 13.

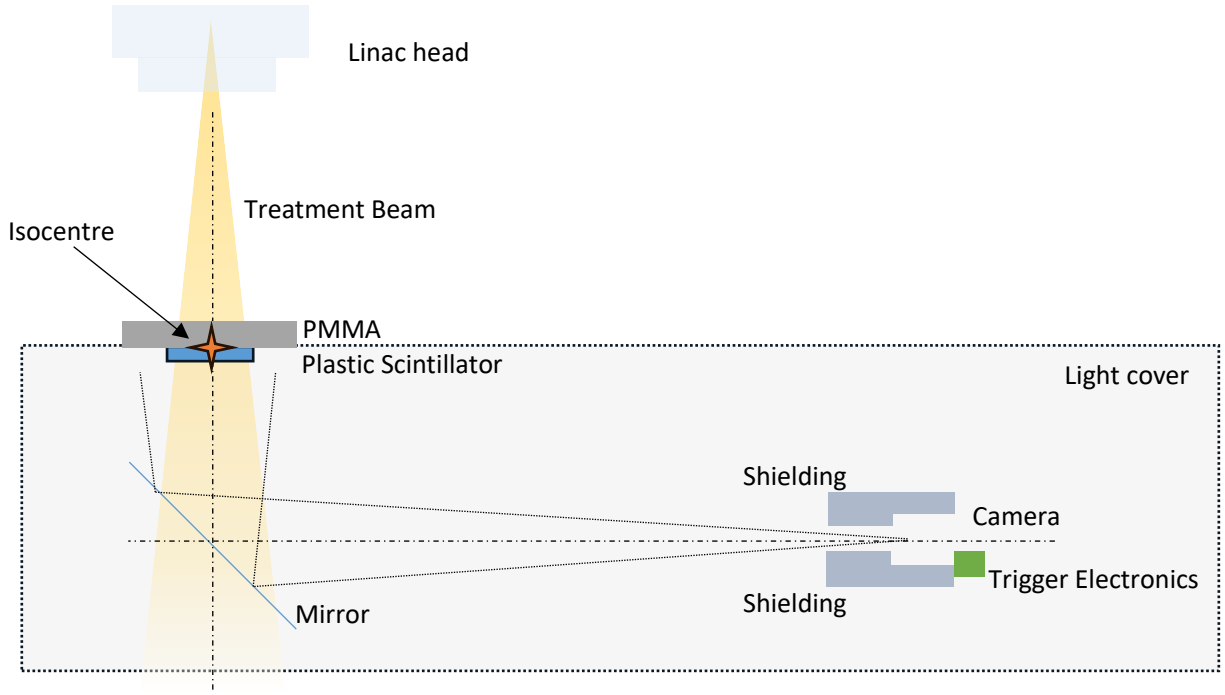

Figure 13 Schematic cross section of experimental setup.

The PMMA material is arranged in the form of slabs stacked at the centre of the radiation axis above the measurement plane. These plates act both as a mounting material and as a cover to block ambient light. Below, tissue-equivalent plastic scintillators have been place. A mirror placed under the scintillator at an angle of 45° reflected this light, allowing the camera to be positioned away from the treatment beam. The camera was positioned at such a distance that it was not within the primary beam from the accelerator. The surrounding shielding blocked stray radiation reducing background noise and protects camera and trigger electronics. Behind the shielding, the electronics for triggering the camera acquisition. All elements, except the PMMA blocks, were enclosed in a non-transparent cover to prevent interference from ambient light.

Among the available tools and materials for the phantom construction, the ‘v-slot 20’ technology was chosen. This is a system of square and rectangular profiles with slots of 6 mm width for every 20 mm side of the profile. The depth of the V groove is 5.5 mm. At both ends of the profile, there is a 5.5 mm hole, in which one can place the M6 screw after previously using a tap. Anodized aluminium profiles were used. . Cross-section of ‘v-slot’ 2020 profile was shown in Figure 14

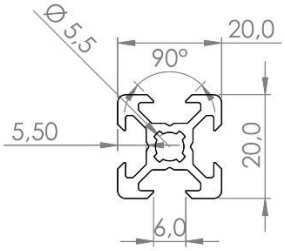

Figure 14"v-slot 20" aluminium profile cross section with dimensions [109].

The system design was carefully prepared using FreeCAD (FreeCAD, www.freecad.org), an open source and highly versatile 3D CAD modelling software. This software allows parametric design, which means that the design can be modified by going back into the history of the model and changing its parameters. FreeCAD was instrumental in creating the system design due to its robust features and user-friendly interface. It enabled the designers to visualise the system in 3D space, take accurate measurements and make changes in real time. The use of FreeCAD ensured a high level of accuracy and efficiency in the design process, contributing significantly to the overall quality of the system design. The ability to easily manipulate and modify designs in FreeCAD provided the flexibility needed for this project, where iterative design and continuous improvement were critical. FreeCAD was therefore an essential tool in the preparation of the system design. The 3D visualization of the phantom and the finished phantom frame are shown Figure 15.

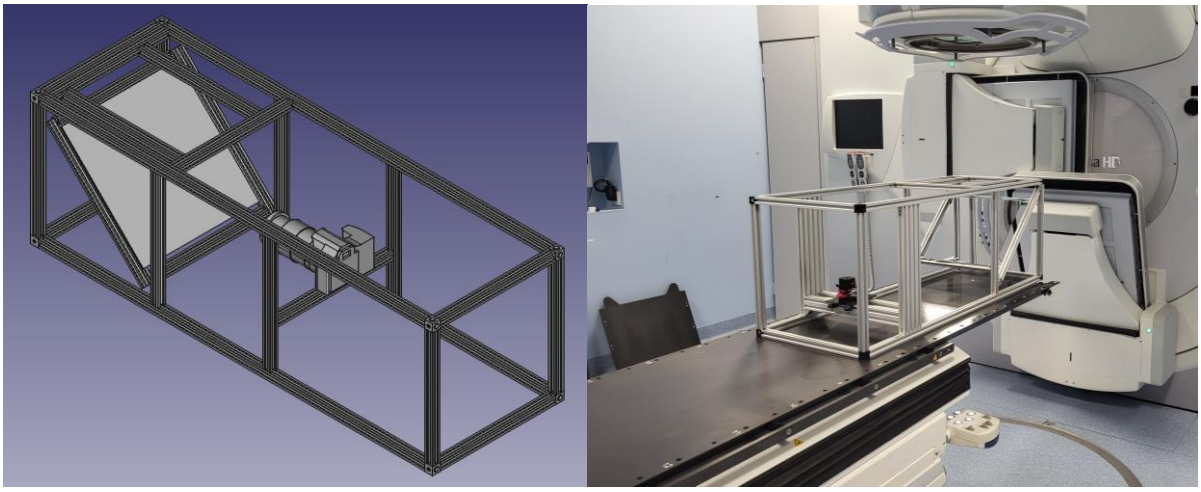

Figure 15 Phantom frame 3D visualization (left) and constructed phantom frame (right).

A complete PVC foam enclosure was constructed for the Phantom. The PVC foam used to

make the cover provided a lightweight but solid structure for the phantom. The openings allowed for the necessary placement of the PSD and camera manipulations, ensuring the functionality of the system. The phantom was coated with multiple layers of matte black paint on both the inside and outside. The purpose of this coating is to minimize light reflection and interference to ensure accurate measurements and observations during the research study. In particular, the use of matte black paint helps to reduce shine and unwanted light reflections that could potentially affect readings from the PSD. Complete phantom with covers is presented in Figure 16.

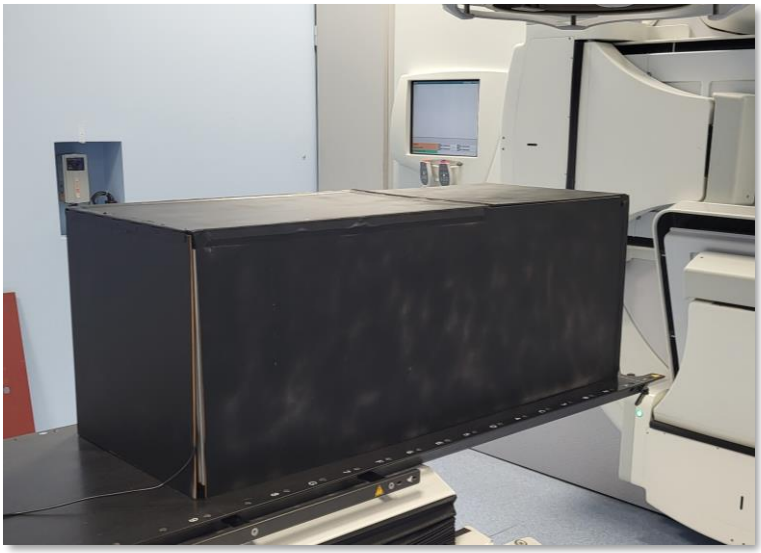

Figure 16 Complete phantom with covers.

The phantom consists of two sections. The front section (left of Figure 13) shows the position where the PSD and mirror are located. On the right side of Figure 13 is the section containing the camera. Both sections can be adjusted independently within the frame in terms of distance, height and angle.

A camera trolley was placed in the light centre, which can move along the axis. Thanks to the V-shaped grooves, appropriately profiled wheels, and the possibility of locking, the trolley could be precisely placed in a selected location. An aluminium tripod head was placed on top of the trolley, with the ability to precisely adjust the tilt angle in any plane up to 5 degrees. An aluminium alloy Quick Release Plate Tripod QR Plate camera mount adapter for DSLR

cameras was placed on top using a ⅜” to ¼” inch adapter. Both parts are presented and complete camera trolley were presented in Figure 17.

Figure 17 Quick Release Plate (left) Tripod Head that enable adjust camera angles(middle) and complete camera mount on trolley.

In front of the phantom, the PSD was placed and held by the top aluminium profiles. Below the PSD, a mirror was placed at a 45-degree angle to reflect light from the PSD. This setup allows for efficient capture and reflection of light, crucial for the functioning of the system. The use of aluminium profiles provides a sturdy and reliable structure to hold the PSD, ensuring its stability during operation. The strategic placement of the mirror enhances the system’s ability to accurately measure and analyse the light from the PSD. This design consideration contributes to the overall effectiveness and accuracy of the phantom in the research study.

4.6 EXPERIMENTAL SET-UP

The Elekta Versa HD linear accelerator at the Katowice Oncology Centre (KCO) was used as a radiation source. The phantom was placed so that the isocentre of the accelerator was in the centre of the PSD sheet. The distance between the PSD radiation source was 100 cm. On top of PSD, two 1 cm thick slabs of PMMA were placed. For precise PSD placement in relation to the isocentre, the phantom was set to hold PSD in a fixed position with the use of the external laser system.

Tenth value layer (TVL) for scattered 6 MV radiation from the polystyrene phantom is equal 0.94 cm of lead [110]. Assuming the worst-case scenario in which the average amount of the scattered photons is the same as in the primary beam, one can use NCRP report #151 (2005) and calculate TVL ratio between lead (5.7 cm) to steel (11cm) as 1.9. Based on this pessimistic assumption, TVL for scattered 6 MV beam for steel is 1.8cm. In front and side of the CMOS

camera 8 cm steel slabs were placed to reduce scatted radiation. Additional 5 cm metal plates were placed above and below the camera. The only unshielded part of the camera was the back to ensure free access to the camera and adjustment of its position. The camera shielding is shown in Figure 18. Since the shields were close to the camera, the initial positioning of the camera in the light axis had to be done without shields. Only after setting the camera in the appropriate position and securing this position could the position of the shields be selected. The position security and quick assembly mechanism of the camera allowed for the removal and reinstallation of the camera without disturbing the geometry.

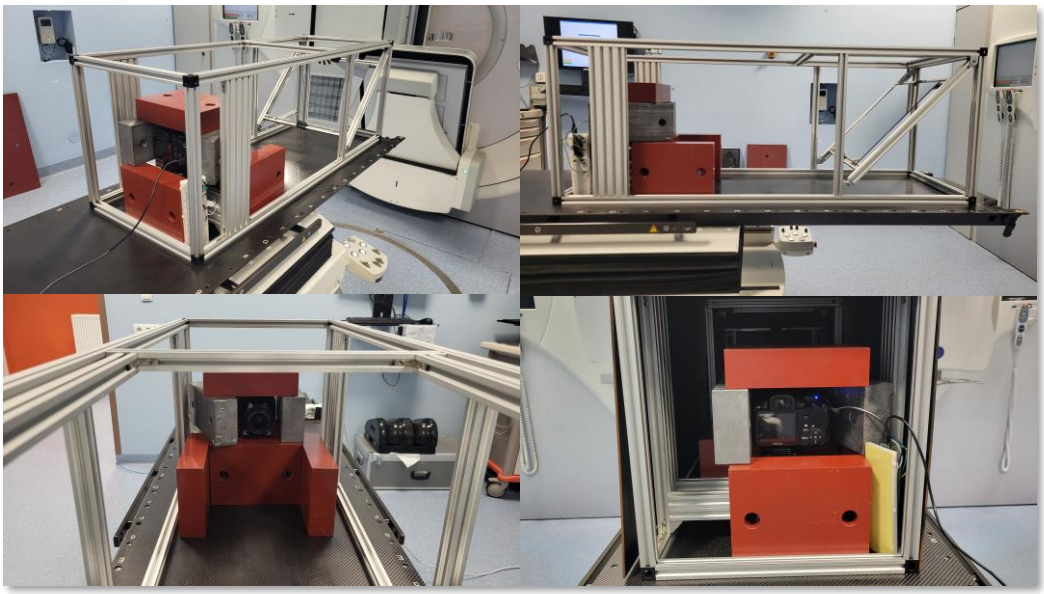

Figure 18 Different views of the camera shielding. The triggering electronics can be seen on the right side of the camera.

This design consideration ensures the flexibility and adaptability of the system, allowing for easy adjustments and modifications as needed during the research study. It also ensures the integrity of the system geometry, contributing to the accuracy and reliability of the measurements. Light sources in the bunker were turned off or covered during experiment.

The Pentax K-x can be remotely triggered using infrared light. However, it is not possible to control IR from the outside of the bunker, so a circuit was built using the Arduino embedded software platform, a prototype board and an IR diode, which, when connected to a PC via a USB cable, is able to transmit a signal to the camera. Due to the distance of approximately 25 meters between the control room and the measurement system in the bunker, the connection

between the Arduino board and PC was made using an active USB cable with a power supply on the receiver side. Figure 19 shows prototyping bord with Arduino and IR diode.

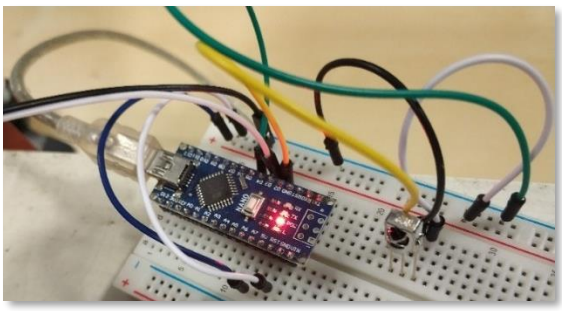

Figure 19 Arduino nano served as IR remote trigger controlled via USB.

PSD setup

The plastic scintillator sheet was placed in the centre of the PMMA blocks using the Gaffer-type tape from the underside of the blocks. A 260 µm thick matte black tape made of polyethylene covered approximately 3 mm of the PSD sheet on each side. In this way, scattering at the edge of the scintillation sheet was eliminated at the expense of a slight reduction in visible area.

The bottom side of the PMMA sheets was painted with a multilayer matte black paint.

Plastic scintillator prepared to test is depicted in Figure 20.

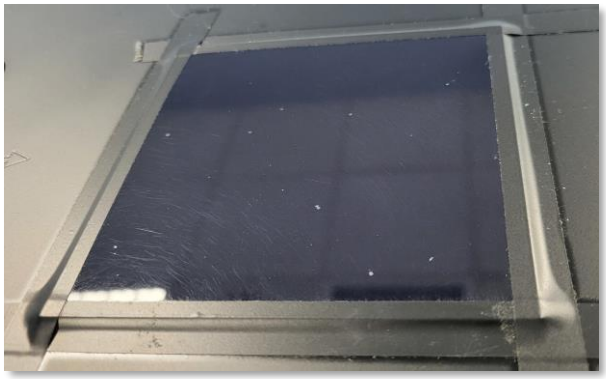

Figure 20 Plastic scintillator mounted to PMMA slab. Graff tape and black painting is visible.

4.7 RADIOCHROMIC FILMS

In the course of this study, Gafchromic EBT-3 dosimetry film was employed as the primary investigative tool. Each sheet, measuring 8" × 10" (20.3 cm × 25.4 cm) was meticulously

segmented into smaller, approximately 10 cm × 10 cm pieces, with each sheet yielding four such pieces. Each piece was then individually numbered for ease of reference. The residual portion of each sheet was utilised for the calibration of individual dose measurements.

Throughout the study, the usage of dosimetry films adhered strictly to the procedural guidelines delineated in the AAPM report TG-55 [111], as well as the guidelines for reference dosimetry pertaining to small and non-standard fields [112].

Subsequent to exposure, the films were scanned with the use of the Epson 10000XL flatbed scanner, a process conducted 24 hours post-exposure. The scanning was executed in a 48-bit RGB format at a resolution of 72 dpi, with no colour profile applied during the process. This ensured the preservation of the raw, unaltered data from the films.

The scanning response of EBT-3 radiochromic film is dependent by its orientation on the scanner. The result for different orientation may vary by 10% [113]. Therefore, the orientation of each film was carefully documented during the subsequent measurement and analysis. In addition, it is known that the scanner output is affected by the position of the film relative to the scan axis. This position-dependent lateral artefact becomes significant the further the film is positioned from the centre of the scanner. For a distance of less than 5 cm from the scanner's central axis, the error is less than 2% [113]. To counteract the lateral artifact, films were strategically positioned along the central axis during scanning. During the experiment 10 cm × 10 cm films were used along with three channel analysis method that significantly reduced the lateral artifact [114]. Consequently, no additional correction for the lateral artifact was deemed necessary.

Image processing

Images were processed with the MATLAB software using developed scripts. In the first step, acquired images were aligned with calculated dose plane using flip and rotate operation. Next, average background was calculated for each colour channel. The Gafchromic films generate colour images upon exposure to radiation, particularly in the red spectrum. Multichannel flatbed scanners are preferred for radiochromic film scanning due to their ability to select the red colour channel which enhances sensitivity at lower doses. Additionally, these scanners extend the film's dynamic range to higher doses by utilising the signal from the green or blue channels. Pixel value $P_{R|G|B}$ were in range 0-65535 (2^{16}) determined by scanner colour depth. Conversion from pixel value to optical density *OD* was performed with the formula:

$$OD_{R|G|B} = -log\left(\frac{P_{R|G|B}}{65535}\right). \quad (15)$$

Data conversion from scanner space to dose space was performed in the MATLAB software.

Film dose calibration

The response of the Gafchromic EBT-3 for all three channels was measured for signal to dose calibration. Twenty films irradiated with doses ranging from 0 to 1900 MU were scanned with the use of the Epson. Films were irradiated in 10 × 10 cm^2 with SSD 98 cm and 2 cm build-up made of PMMA. Films response was measured in a small area at the centre. The calibration of the film response, measured as optical density OD vs. administered dose, was performed for the red, green, and blue channels (indicated by the index *R|G|B*). In terms of optical density *OD* and dose *D* for each channel, these functions take the form:

$$D_r = \frac{c_{R|G|B} * 10^{(-OD_{R|G|B})} - a_{R|G|B}}{b_{R|G|B} - 10^{(-OD_{R|G|B})}}, \quad (14)$$

where *a,b,c* are curve fit parameters and *OD* is optical density.

Dose calculation

Dose evaluation was conducted using a triple-channel dosimetry method described in literature [113] [114] [115]. According to the Beer-Lambert law, the scanned optical density $OD_{R|G|B}$ at any point is inversely proportional to a dimensionless measure representing the thickness of the films active layer τ which is channel and dose independent. Therefore τ influences optical density results in each channel in the same way. Furthermore, τ can be normalised with average value $\bar{\tau}$. Then, optical density can be expressed as:

$$OD_{R|G|B} = ODI_{R|G|B} * \Delta\tau, \quad (16)$$

where $\Delta\tau = \frac{\tau}{\bar{\tau}}$ and $ODI_{R|G|B}$ is optical density independent of relative thickness and varies only with the exposure *D*. Since the dose is the colour channel independent the function $\Omega(\Delta\tau)$ can be considered and we can minimise the differences in the dose results from the individual colour channels i.e.:

$$\Omega(\Delta\tau) = (D_R - D_G)^2 + (D_R - D_B)^2 + (D_G - D_B)^2 \rightarrow \min_{\Delta\tau}, \quad (17)$$

Resulting map $\Omega(\Delta\tau)$ is used as a correction map for any channel and dose calculation formula looks as follows:

$$D_r = \frac{c_{R|G|B} * 10^{(-ODI_{R|G|B}*\Delta\tau)} - a_{R|G|B}}{b_{R|G|B} - 10^{(-ODI_{R|G|B}*\Delta\tau)}}. \quad (18)$$

Scripts that perform three-channel dosimetry were created in the MATLAB environment. Numerical methods were used to calculate $\Delta\tau$ for each pixel on the film.

4.8 SRS MATRIX

The SRS MapCHECK (Sun Nuclear, USA) was selected as one of the reference methods. It is an innovative tool for patient-specific quality assurance in stereotactic radiosurgery and stereotactic body radiotherapy. It replaces the traditional use of use of a radiochromic film and offers a streamlined, digital approach for improved patient safety [116].

The SRS MapCHECK is equipped with 1,013 diode dose measurements, providing high-density detection and unmatched diode detector resolution. The 2.47 mm detector spacing allows for measurements as small as 5 mm which is the smallest clinically used field size at most sites. This feature, combined with an unmatched 0.48 mm detector resolution and patented angular dependence correction, supports robust QA and task group requirements [116]. Detailed detector spacing is shown in Figure 21.

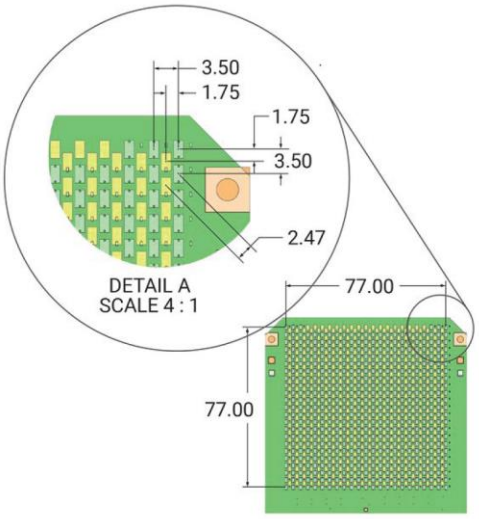

Figure 21: Detector Array Spacing [116].

The system was placed in Sun Nuclear's StereoPHAN phantom, which allows for rotational delivery and supports both conventional linacs and CyberKnife systems. This compatibility

accelerates the workflow for time-sensitive patient QA, making the process more efficient. A sample system setup for SRS MapCHECK is shown in Figure 22.

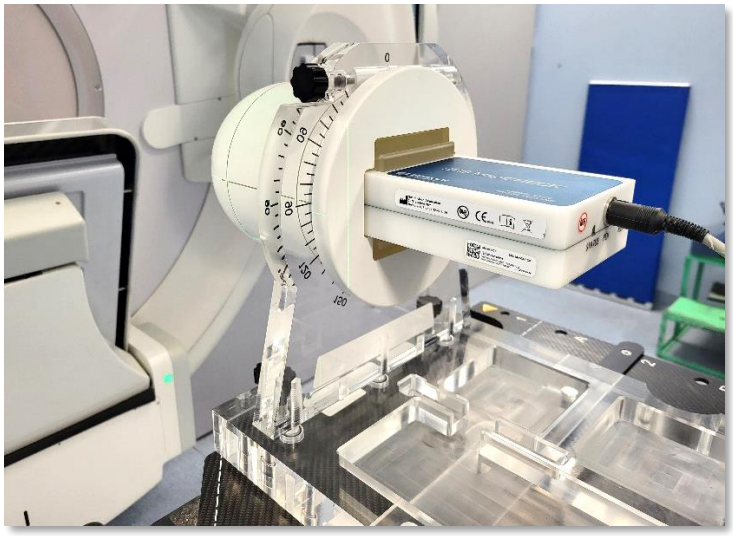

Figure 22: SunNuclear SRS MapCHECK detector in StereoPHAN phantom.

A limitation of the SRS MapCHECK is the size of the activated part of the detector matrix, which is 77 × 77 mm². This limits the effective size of the measured fields to these dimensions. For larger fields, a part of delivered dose is not registered by the device. There is also a risk of irradiating electronics and damaging equipment

Before performing PSQA with the SRS MapCHECK, two types of calibration measurements are required: array calibration and dose calibration. Array calibration is necessary to determine the differences between the SRS MapCHECK detectors and to introduce a correction factor for each of them. The SRS MapCHECK full array calibration procedure involves multiple shifts and rotations of the instrument with respect to the radiation field. The measurement was taken using the Elekta Versa HD accelerator in KCO. Calibration was performed according to the manufacturer's guidelines. The first part of the calibration related to matrix geometry and response calibration while the second part was dedicated to dose calibration. Four measurements were performed with the array without the StereoPHAN positioned directly on the treatment couch at the beam isocentre, using a 10 × 10 cm^2 AP field (6MVWFF, 200 MU). A further four measurements were conducted with a 10 × 10 cm^2 PA field. Two measurements were conducted with a 5 × 5 cm^2 MLC field (6 MV FFF, 200 MU) using the SRS MapCHECK in the StereoPHAN: one measurement was recorded with the array in the AP position and the other with the array reversed to the PA position. After all measurements, the relative sensitivity

of all the detectors was determined and the information required for the diode angle correction was obtained. Absolute dose calibration was required for used beam energy. Plans delivered to SRS MapCHECK were verified against TPS calculations using SRSMapCHECK software version 8.5.1.9. Comparison of the following parameters was performed: threshold 10%, dose difference 1-3%, distance-to-agreement 1-3 mm and analysis set to global. Before each calculation the optimum image registration was applied by the built-in function that calculates the spatial offset and rotation between data sets. A screenshot of sample analysis is shown in Figure 23.

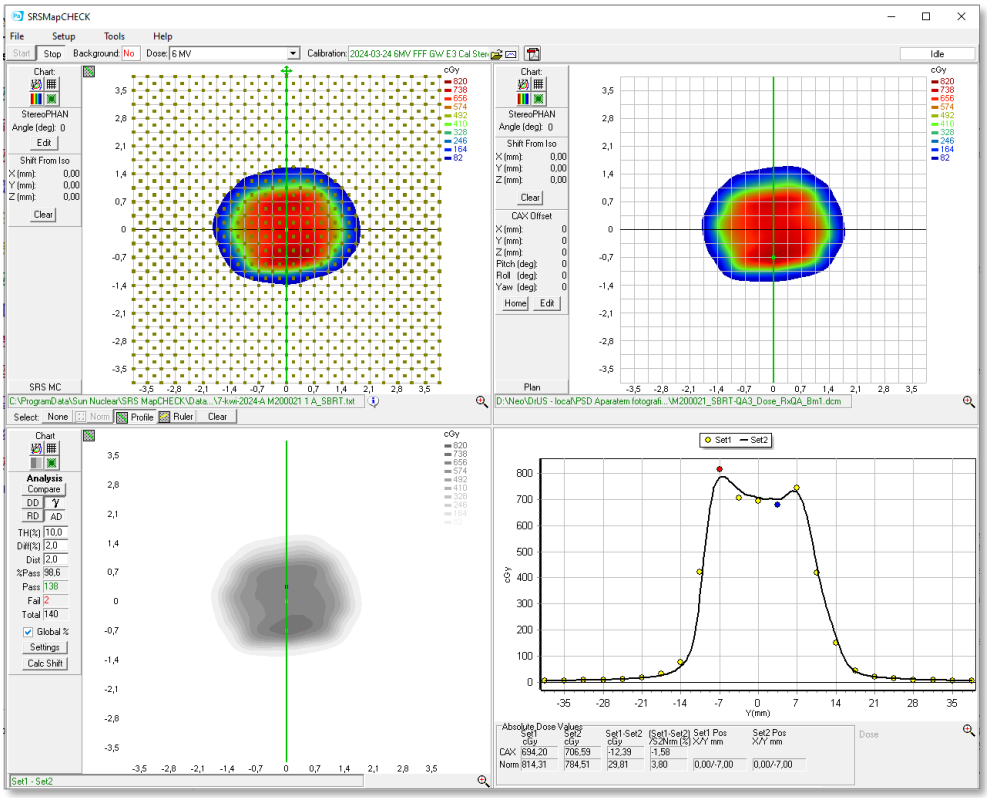

Figure 23: Sample screen from SRSMapCHECK software.

In the upper raw, the left figure presented measured dose distribution and the right picture the dose plane imported from TPS. In the lower raw, starting from the left site panel, the analysis present type analysis criteria, and GI pass evaluation results. The next picture shows the dose difference between datasets and the last picture presents a cross-section profile along selected axis marked as green line on previous picture.

4.9 PATIENTS SELECTION

To validate the clinical application of PSD, a data set comprising 42 treatment plans was used. These plans, treated with a target diameter less than 10 cm to accommodate the size of the PSD, were administered in 2023-2024 at the KCO using the Elekta VersaHD machines. All patients were clinical and subjected to a standard workflow. Simulations were conducted using a Siemens BigBore CT scanner with a step size of 1 mm. Radiation oncologists employed the Monaco TPS (Elekta, Sweden) version 6.1.2.0 to contour PTV and OARs, adhering to standard contouring protocols. The treatment plan was devised by a medical physicist and subsequently verified by a second medical physicist. Ultimately, the plans were approved by a radiation oncologist. Prior to treatment, all plans underwent verification through independent calculations or measurements. The primary characteristics of the selected cases are presented in Table 3.

Table 3: Cases selected for verification. Maximum dose, area and field size are calculated in TPS at a plastic scintillator plane: SSD 98 cm and depth 2 cm. For beam size calculation threshold 10% of a maximum dose was applied.

Patient ID	Field ID	Max dose from TPS [cGy]	Area [mm^2]	Field size [mm × mm]	Planned MU	Planned Dose [cGy]	Beam type
A081451	3.1	1765.8	2297	61x47	1200	2238.0	6
M172343	4.1	434.9	2594	53x66	250	480.7	6
M172343	4.2	310.2	2585	51x67	250	369.9	6
M172525	1.1	1866.9	2577	63x46	1200	1788.9	6
M191092	2.1	528.1	2087	66x39	300	781.9	6
M191092	2.2	1138.1	2903	65x52	600	1831.2	6
M191395	1	1642.1	747	30x29	900	1427.3	6FFF
M200021	1	1074.7	813	35x28	400	1037.4	6FFF
M200021	2	576.8	834	36x28	500	478.1	6
M200349	1.1	598.3	3991	60x76	400	719.7	6
M200349	1.2	690.7	3981	58x82	400	1197.4	6
M212554	3.1	295.6	3535	77x56	250	392.8	6
M212554	3.2	402.1	3322	76x55	250	766.4	6
M230270	2.1	1063.3	1144	42x33	620	944.0	6FFF
M230270	2.2	646.6	1035	37x33	380	556.8	6FFF
M230418	2.1	321.6	3206	61x65	250	346.7	6
M230418	2.2	350	3720	69x65	250	447.2	6
M230520	1.1	622.8	2851	63x52	261	530.9	6
M230520	1.3	778.7	3019	64x53	327	721.9	6
M230520	1.4	682.9	2164	60x43	1141.7	473.0	6
M230520	1.5	800	2263	59x46	903.2	400.0	6
M230520	1.6	492.2	2331	58x47	1092.1	400.0	6
M230520	1.2	927.5	2494	59x48	539	1400.9	6
M230541	1.1	1088	1317	45x35	800	899.4	6FFF
M230688	1.1	675.7	2565	64x47	376	739.4	6
M230688	1.2	899.3	2713	63x49	524	1390.0	6
M230704	1.1	1081.6	1088	39x34	545	1415.2	6

M230704	1.2	576.6	1035	37x35	255	1061.2	6
M231052	1.1	831.6	2067	49x50	600	950.5	6FFF
M231118	1.1	439.1	3012	67x57	270	555.8	6
M231118	1.2	313.5	3488	75x57	230	410.5	6
M231118	1.3	265.9	990	36x31	200	401.1	6
M231118	1.4	592.9	1270	34x48	400	965.1	6
M231213	1.1	814.1	3675	76x55	364	1082.2	6
M231213	1.2	1108.1	3652	57x73	536	1688.3	6
M231248	1.1	453.3	2248	53x53	300	623.2	6
M231248	1.2	332.7	2403	58x54	200	416.6	6
M232066	1	3410.6	2482	55x57	1800	3883.0	6FFF
M232191	1	494.4	1761	49x46	400	839.9	6
M232191	2	413.5	1721	47x45	200	428.2	6
M232213	1.1	611.7	2242	60x45	400	840.9	6
M232213	1.2	496.4	1980	54x45	400	555.2	6

On average, the filed size was $55 \times 49\ mm^2$. The median plan dose was 752.9 (IQR 474.3-1077.0) cGy.

4.10 PLAN QUALITY ASSURANCE IN TPS

The TPS software used for the computation of the calculated treatment plans was Elekta Monaco, installed at the radiotherapy division at KCO Monaco's VMAT functionality can optimise single or multiple non-coplanar arcs simultaneously, providing the flexibility and control needed for complex treatment plans such as VMATs. Monaco offers the XVMC Monte Carlo dose engine, for electrons and photons, for a continuous arc calculation as a single beam, rather than just dose approximations that occur with many discrete gantry angle positions.

Once the optimisation process is complete, the validated plan is exported to the accelerator's control software.

In the next step, QA plans were prepared. CT scans were taken of the SRS MapCHECK inside the StereoPHAN and the PMMA with PSD plates. The CT was imported into Monaco TPS. The isocentre of the plan was set at the centre of the detector array for the MapCHECK and at the centre of the PSD for the PMMA phantom. For each patient, two QA plans were generated by superimposing the clinical plan on the CT images of the StereoPHAN and the PMMA phantom with PSD geometry.

All plans were calculated using the Monte Carlo algorithm of Monaco TPS version 6.1.2.0. To minimise the influence of the accelerator gantry performance and to avoid influencing the angular response for both the SRS matrix and the PSD, the gantry angle was set to 0 for all

plans. The highest available dose grid resolution of 1 mm was used. A statistical uncertainty of 0.3% per plan was applied to the calculation. The average calculation time was 25 minutes per beam for StereoPHAN and 60 minutes per beam for the PMMA phantom. For each calculation, the dose plane in the plastic scintillator plane was exported in DICOM format for each field. The same dose plane was used for EBT-3 films and plastic scintillator Gamma Index analysist.

4.11 GAMMA INDEX

Treatment plans in QA mode were delivered three times to two different phantoms to measure dose distribution in all three methods – PSD, SRS MapCHECK and Gafchromic EBT-3 films. Measured dose distributions were compared with those calculated in the TPS using Gamma Index analysis. For SRS MapCHECK, the analysis was performed in SunNuclear SNC Patient, (module SRS MapCHECK) software. PSD and film measurements were compared in the Matlab software with the use of the developed scripts. Gamma Index parameters commonly used for film analysis were 3-2%/3-2 mm [113] [26] and 2-3%/1 mm for radiosurgery [62]. For SRS MapCHECK, reported values were in a range 1-3% for dose difference and 1-3 mm for distance-to-agreement [117] [118] [119]. Values suggested by the Report of AAPM TG 135 [120] for PSQA gamma index analysis were 2% dose difference, distance-to-agreement equal 2 mm and the dose threshold of 10%.

To comprehensively examine the results for the tested system with PSD in relation to ETB-3 and SRS MapCHECK the following parameters were applied for the calculation of GI: DD in a range 1-3%, DTA in a range 1-3 mm, the threshold set to 10% and gamma tolerance limit of 90% and 95%.

For the deeper evaluation using gamma histogram of the analysed system the following gamma analysis parameters were used: 2%/2 mm, threshold 10% and pass rate 95%.

4.12 STATISTICAL ANALYSIS

Acquired Gamma Index results were analysed with the Matlab software. The significance level used for the analysis was 0.05. Results were arranged in ordered groups for each method: EBT-3, SRS MapCHECK and PSD. For clarity, three-letter abbreviations for each method were used: EBT, SRS and PSD, respectively. The results were analysed for different Gamma Index parameters: DTA 1-3 mm, DD 1-3% and tolerance limit 90 and 95%. Not all combinations

of DTA and DD were clinically meaningful but gave a better understanding of each method and scope and limitations of PSD in relation to reference methods.

Cochran's Q test was used to test for statistically significant differences between EBT-3, SRS MapCHECK and PSD in terms of gamma analysis successes and failures. The Shapiro-Wilk test was used to assess the normality of the data. Based on the non-parametric Kruskal-Wallis test, gamma index value analyses were selected. Wilcoxon signed rank test, also known as Mann-Whitney U test, was performed to check whether a GI result for each gamma setting for PSD was between the GI results for EBT and SRS. Kolmogorov-Smirnov test was used to determine whether the gamma index histograms are statistically different.

Shapiro-Wilk test

The Shapiro-Wilk test was used to check Gamma Index normality for each group [121]. The test is designed to determine if the null hypothesis of composite normality is a reasonable assumption regarding the population distribution of a random sample at a given significance level [122]. The result of this test determines whether parametric or non-parametric methods would be used for the analysis.

It should be noted that the Gamma Index value can vary from 0 to infinity. In practice, the expected values are between 0 and 1. Therefore, the distribution of gamma values should not, by nature, follow a normal distribution. The test result for a given field, i.e. the percentage of points that have a value less than or equal to 1 for a given gamma parameter, is always between 0 and 1. This corresponds to the extreme situation where none of the points in the compared dose maps has GI value less than or equal to 1, or, where all points have values less than or equal to 1 [123].

Cochran's Q test

Cochran's Q Test is for dichotomous data for k-related samples. Cochran’s Q test is specifically designed for binary responses and can be applied to compare treatment effects or results between methods [123]. The test performs the non-parametric Cochran's Q test on the hypothesis that the K columns of N-by-K matrix have the same number of successes and failures. It is used to verify the hypothesis of symmetry between the results of multiple measurements [122].

Null hypothesis H_0 is that all “discordant” observed counts are equal while alternative hypothesis H_1 where not all “discordant” observed counts are equal. "Discordant" counts are calculated when the value of the trait under study is different in successive measurements. This test is an extension of the McNemar test for more than two dependent groups.

Wilcoxon signed rank test

The Wilcoxon signed rank test is a nonparametric test for two populations when the observations are paired [122]. In this case, the test statistic, W, is the sum of the ranks of positive differences between the observations in the two samples. When you use the test for one sample, then W is the sum of the ranks of positive differences between the observations and the hypothesized median value. For large samples, or when method is approximate, the function calculates the p-value using the z-statistic [123].

Kolmogorov-Smirnov test

The two-sample Kolmogorov-Smirnov test, a non-parametric method, is utilized to ascertain whether two independent samples have been drawn from the same continuous distribution [121].

The null hypothesis (H_0) of the test is formulated such that the two samples are derived from the same distribution. The maximum absolute difference between the cumulative distribution functions (CDFs) of the two samples is defined as the test statistic, D [123].

The null hypothesis is rejected if the test statistic, D, exceeds the critical value at a given significance level.

In the context of a two-sided test, the alternative hypothesis is formulated such that the distributions of the two samples differ. The null hypothesis is rejected if the test statistic is significantly large, suggesting that the two samples likely originate from different distributions.

It is crucial to note that the sensitivity of the two-sample Kolmogorov-Smirnov test extends to differences in both location and shape of the empirical cumulative distribution functions of the two samples. This characteristic renders it a powerful tool for comparing two samples. However, it also implies that the test can be sensitive to trivial differences and may lead to frequent rejection of the null hypothesis if the sample size is large [122].

5 RESULTS

5.1 PRELIMINARY RESULTS

Edge light and background colour

A sheet painted with layers of black matte paint reduced the amount of light collected by the camera compared to the white matte background but simultaneously sharpened the edges of the captured shape. Covering the edges with black matte tape resolved the issue of matrix saturation, as the brightest region of the image was the edge of the PSD sheet. Figure 24 presents the acquired imaged for 6 MV 5 cm × 5 cm field without (left) and with those improvements.

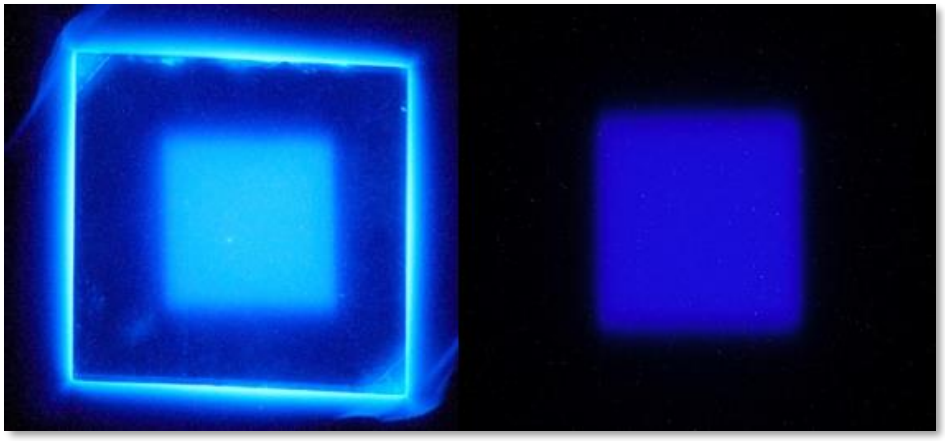

Figure 24 On the left, one of the first images collected for a 5 × 5cm field in the isocentre with a white background and no black tape around the edges. Right: image collected with a matte black background and with tape on the edges. Even the irregularities on the lower and upper edges due to the alignment of the MLC collimator leaves can be seen.

A side-effect of these adjustments was less light reaching the camera, necessitating an increase in sensitivity and/or a smaller aperture.

Colour channel selection

The camera CMOS sensor captures the signal in three colours (red, green, and blue), with 99% of the signal captured in the blue channel within the scintillator area. The remaining two channels showed no statistically significant differences in signal between the scintillator and outside the scintillator area. To minimise noise, only the blue component of the acquired images was used for further data processing.

Background Noise

Electronic noise measurements revealed that the background signal independent of exposure time at the level 0.3% of the maximum sensor signal for ISO 100 and 200, and 0.7% for ISO 400. The mean background signal across exposure times (10 s to 90 s) for ISO 100, 200, and 400 is presented in Figure 25. ISO 100 (an extended mode) and ISO 200 (regular mode) exhibited similar results. Reduced noise observed at 60 seconds remains unexplained, attributed to the camera's firmware processing.

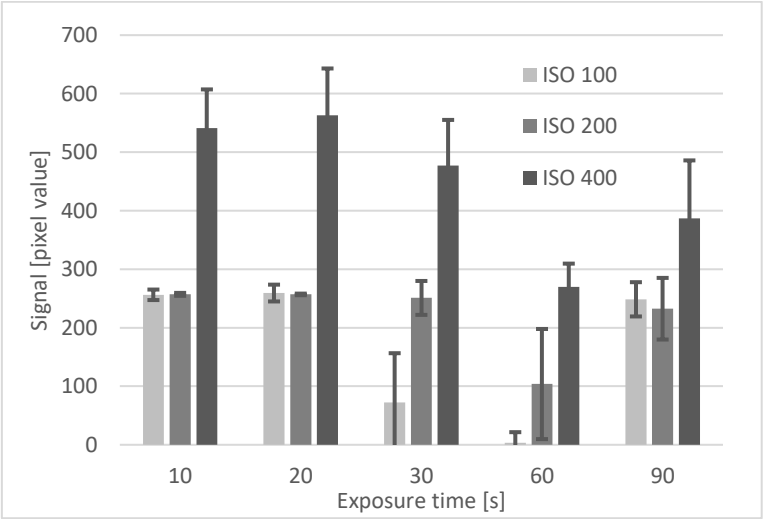

Figure 25 Signal as mean pixel value for different exposure times at different ISO settings. The results were filtered using the median and Wiener filters. Error bars represent the standard deviations of the individual measurements [108].

It was noticed that for exposure time equal and above 30 s there is a significant drop in background signal. It was found that this was due to the camera firmware which, despite disabling all noise reduction functions, automatically took a second exposure at the same time but with the shutter closed. The resulting image was then subtracted from the original image. The camera had no option of disabling this function.

Stray radiation

Measurements were performed with a 6 MV beam and a 15 × 15 cm² field size, with the plastic scintillator removed. For doses below 500 MU, the signal was dose-independent (mean value = 259), while an increase in signal occurred for doses equal to and above 500 MU. A two-parameter linear function ($ax + b$) with parameters a = 1.2476 and b = 167 described these results.

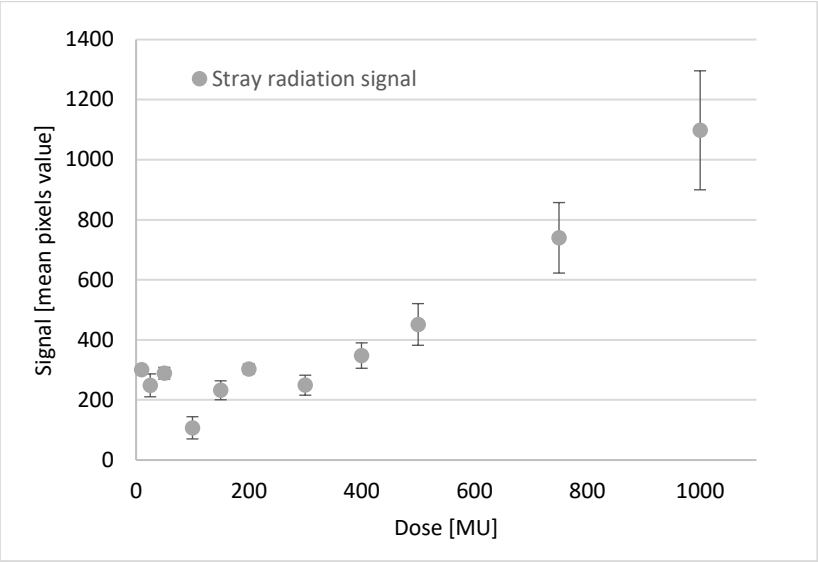

Figure 26 Measurement of stray radiation as a function of dose. Signal as mean pixel value vs. the delivered dose for the field 15 × 15 cm². Each measured value contains the electronic noise and stray radiation signal. The CMOS camera ISO was set to 100. Error bars represent the standard deviations of the individual measurements [108].

There was no significant difference between the signal below 500 MU and the background. For doses of 500 MU and above, a clear correlation between the administered dose and the signal value was observed. The linear fit coefficient (R^2) between dose and signal above 500 MU was 0.997. Additionally, the standard deviation increased, indicating more collected noise.

Measurements for dependency between stray radiation and field size was investigated using 100 MU and five different field sizes (ranging from 3 × 3 cm² to 20 × 20 cm²) at ISO 100, 200, and 400. Signal increase from stray radiation was observed for field sizes above 10 × 10 cm², while a constant response was observed for smaller fields.

The amount of stray radiation depends on the field size and ISO settings shown in Figure 27.

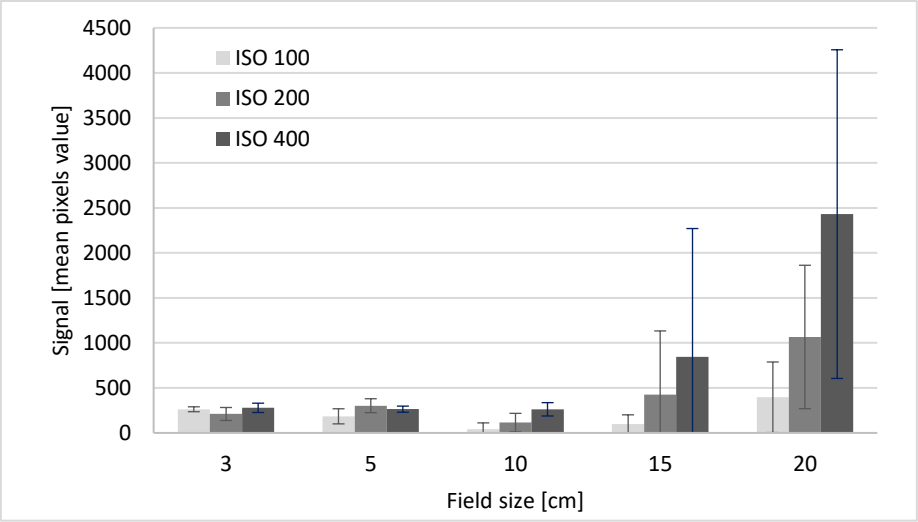

Figure 27 Measurement of stray radiation in relation to field size. Signal as mean pixels value vs. different square field sizes (side of the square field). Results presented for three different ISO values. The standard deviation of each signal value is imposed on bar graph [108].

This experiment showed that for doses below 400 MU, the stray radiation signal was mainly background noise for the studied setup. For doses above 400 MU, an increase in noise of 1.2% of the maximum signal for every 1000 MU given can be expected. In Figure 27 rapid increase of the stray radiation noise was observed for fields larger than 10×10 cm^2.

System repeatability

System repeatability was assessed through ten measurements at ISO 200 and 400, with mean signal values of 33144 and 21096, respectively. The standard deviation of the mean was 0.43% for ISO 400 and 0.13% for ISO 200, while the average standard deviation for single measurements was 0.93% for ISO 400 and 1.41% for ISO 200. Results are shown in Figure 28.

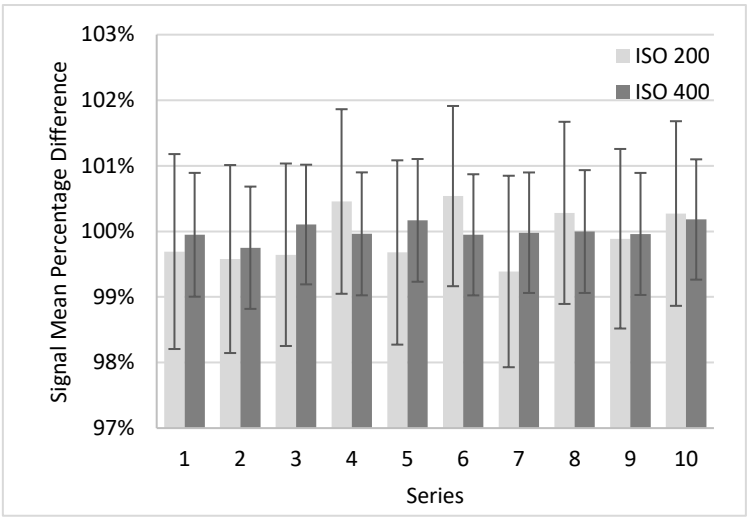

Figure 28 Repeatability measurements at ISO 200 and 400 as percentage differences to average results from all series. The standard deviation (SD) of each signal value is imposed on bar graph. The average SD for ISO 200 and 400 is 1.41% and 0.93% respectively. The lower SD for ISO 400 is due to the higher signal, while the noise is comparable for both setups [108].

Dose Rate dependency

The measured 6 MV FF and 10 MV FFF beams were calibrated to deliver 1 cGy/MU at 10 cm depth at a source-surface distance (SSD) of 90 cm for the 10 × 10 cm² field. The experiments were conducted across various setups: 6 MV beams were delivered with a smaller mirror-camera distance and a 5 × 5 cm² field size, achieving approximately 78% of the maximum sensor signal, while 10 MV FFF beams were delivered with a 15 × 15 cm² field size and had 48% of the maximum sensor signal. To compare signals for different energies, the data was normalised to the average signal for each energy, as shown in Figure 29

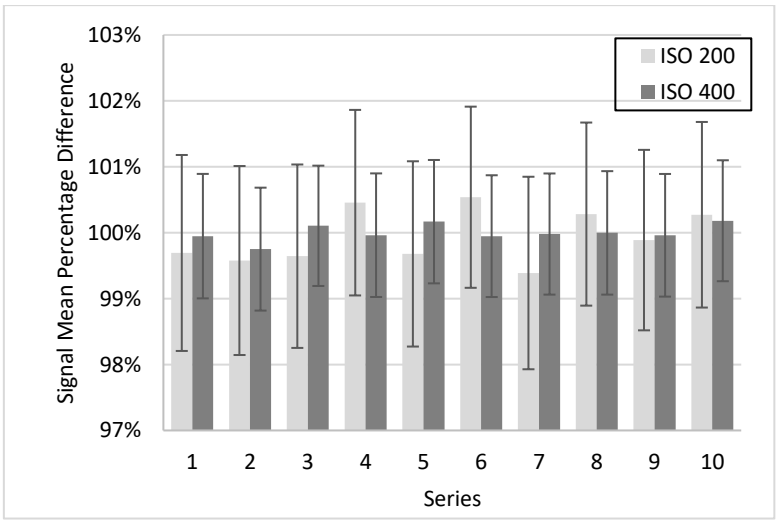

Figure 29. Repeatability measurements at ISO 200 and 400 as percentage differences to average results from all series. The standard deviation (SD) of each signal value is imposed on bar graph. The average SD for ISO 200 and 400 is 1.41% and 0.93% respectively. The lower SD for ISO 400 is due to the higher signal, while the noise is comparable for both setups [51].

Relative signal for each energy ranged between 99.45-100.37% (SD=0.23%). For individual energies, 6 MV FF and 10 MV FFF range from 99.22-100.93% (SD=0.34%) and 99.86-100.09% (SD=0.10%), respectively. The mean SDs for single measurements are 0.42% for 6 MV FF and 2.46% for 10 MV FFF. The lower SD for 6MV FF is due to a smaller field size and higher signal compared to 10 MV FFF, resulting in less stray radiation.

Dose dependency

The dose–response function f of the detector was investigated by delivering different doses to the scintillator. Sample images are shown in Figure 8. Doses were delivered for ISO 100 and 400 in the same setup, while ISO 200 used a different geometry. Using the fitting software, more than 400 curves of 2 and 3 parameters were tested for the best fit. The curve $\frac{x}{\left(a+\frac{x}{b}\right)}$ normalised for dose between different ISO settings is shown in Figure 30. The following parameters were fitted to all data with 95% confidence bounds: a = 139.8 (135.6, 143.9), b = 556.2 (535.9, 576.4), R^2 = 0.999.

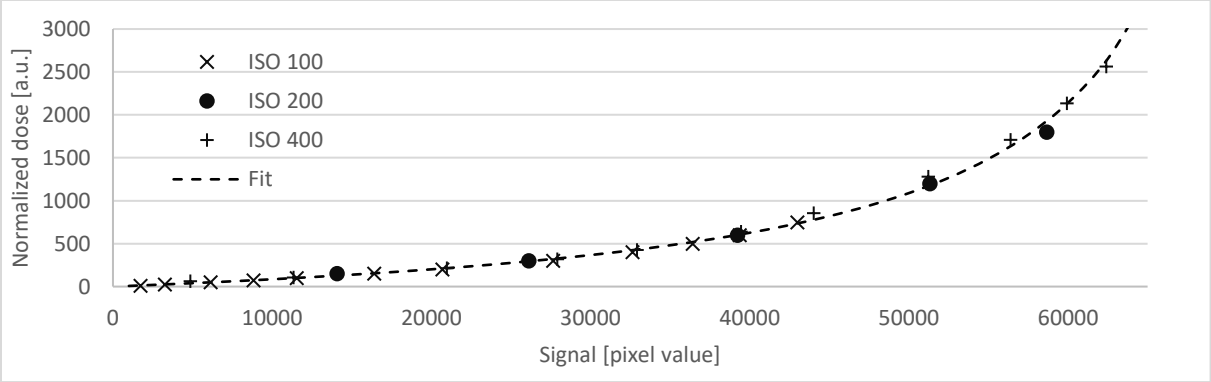

Figure 30. The signal versus normalised dose (arbitrary units).

The observation indicates that when the signal values exceed half of the sensor's maximum capacity, the relative increase in signal corresponds to a more significant change in dose. Consequently, the system exhibits reduced sensitivity to variations in relative dose at elevated signal levels. For this reason, exposures for which the CMOS matrix response exceeds 80% of the maximum value should be avoided.

ISO

Measurements were performed for ISO values 100, 200, 400, and 800 to obtain signal-ISO dependence. The resulting signal was compared with ISO 100 and dose calculations were made for each ISO setting using the signal-dose equation. Considering that ISO have only few values, a look-up table for is preferable to calculate ISO correction factor. Results were presented in Table 4.

Table 4 Camera ISO, the measured signal, the signal converted to the dose [cGy] and calculated ISO correction factor [108].

ISO	Measured Signal [pixels value]	Calculated dose response [cGy]	ISO correction fact
100	11488	95	0.990
200	20914	202	2.117
400	33113	410	4.301
800	44451	742	7.853

Presented results show that system sensitivity can be altered with ISO settings up to 7.9 times comparing ISO 100 to ISO 800.

Camera aperture

In theory, the quantity of light that a lens captures is linked to the area of the aperture, which is proportional to the inverse square of the *F*-number. Experiments were performed at ISO 200 and ISO 400, with the signal being converted into dose using the signal-dose function. More than 400 curves were examined, and the best fit was found with the function $\frac{x}{a+\frac{x}{b}}$ (with R^2 = 0.999), yielding the coefficients a = 9162 (7724, 1060) and b = -2.819 (-2.909, -2.729). Resulting fit was depicted in Figure 31.

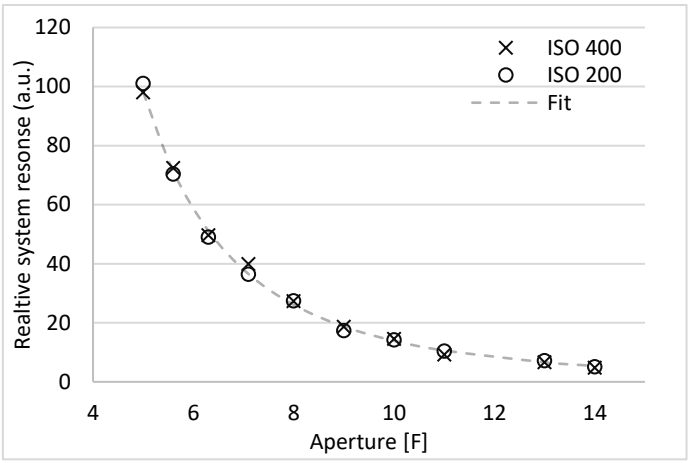

Figure 31 Dose vs. the camera aperture F curve. Fit using $\frac{x}{\left(a+\frac{x}{b}\right)}$ function [108].

The results showed that the system sensitivity could be reduced by a factor of 20 by changing the aperture in the range 5.6 to 14.

Energy dependency

For all accessible photon beam energies, measurements were taken. The signal was then recalculated into a relative dose and rescaled using the signal-to-dose coefficient (Dcf) to derive the absolute dose for comparison with the results from the treatment planning system. The computed Dcf value for the specified geometry was 1.304, which closely aligned with the dose delivered by the 6 MV beam. The dose value from the TPS was 131.1 cGy for 100 MU, with an average variance of 1.1% between the TPS and the measured dose across all energies. Results are presented in Figure 32.

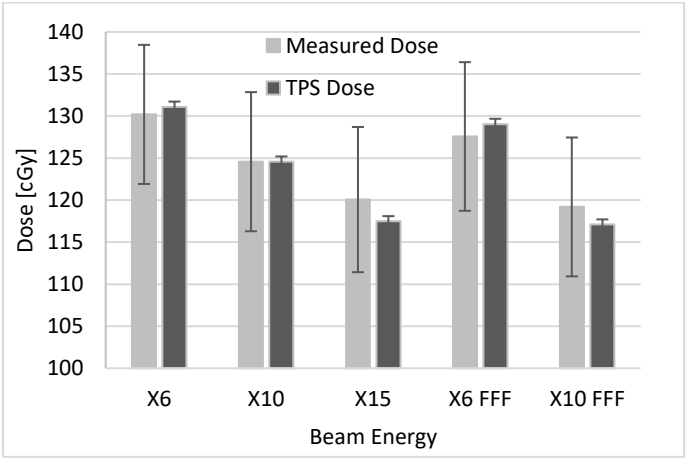

Figure 32 Measured signal versus dose from TPS for different photon energies. Signal was converted to dose and rescaled to the absolute value. The standard deviation plotted on the bar graph [108].

The differences varied from -2.2% to 0.7%, with the maximum discrepancy noted for the 15 MV beam.

Spatial resolution

Images from each scintillator detector were denoised, corrected for vignetting, and tilted. Gafchromic films were irradiated using the same setup, and results were compared with treatment planning system calculations. Two methods were used to calculate field size for the scintillator detector: physical measurement and linear regression. The average differences between film and scintillator were 0.27 mm (first method) and 0.28 mm (second method), with relative differences of 0.91% and 0.94%, respectively. Notably, scintillator results were closer to film measurements than TPS model results.

The Modulation Transfer Function (MTF) for both a dosimetry film and a Plastic Scintillation Detector (PSD) was computed under identical geometry for a field size of 5×5 cm². The corresponding results are tabulated in Table 5.

Table 5 MTF [mm] for a film and PSD

MTF_{50} film	MTF_{50} PSD	MTF_{10} film	MTF_{10} PSD
3.20	3.77	1.26	1.36

The distance corresponding to the spatial frequency at which the MTF is 50% of its maximum value (MTF50) indicates that the blur introduced by the PSD is greater by 0.57 mm, and the minimum discernible detail size is larger by 0.1 mm for the PSD.

5.2 NUMBER OF ANALYSED POINTS

In the experiment, one of the measurement systems used was the SRS MapCHECK matrix. This matrix has 1,013 diodes on a $77 \times 77 mm^2$ surface. The distance between detectors on the matrix is 2.47 mm.

Gafchromic films have a theoretical limit to the number of measurement points related to the multiplicity of the molecule in the radiation-sensitive layer, but practically this multiplicity is limited by the resolution of the scanner. The standard scanning resolution is 72 dpi.

The resolution of the plastic scintillator is theoretically unlimited, but as with films, the limiting parameter is the resolution of the scanner. For the plastic scintillator used in the experiment, it is the resolution of the CMOS matrix, optical settings, and experiment geometry. In this case, the theoretical resolution of the system with the scintillator was 0.09 mm.

During the gamma analysis, these results were first compared with the treatment planning system, which exports the dose plane to a $1 \times 1mm^2$ grid for analysis. Therefore, data for Gafchromic films and the plastic scintillator were scaled from the matrix resolution using the bilinear function. Despite reducing the resolution of the films and scintillator to that of the TPS computational grid, the number of points taken for analysis was still higher than the number of points analysed for the SRS array due to its lower spatial resolution. The average number of analysed points on film and plastic scintillators compared to SRS matrix was 5.76±0.80 and 5.81±0.53 times larger respectively. In theory this ratio should be 6.10 (2.47^2) but for films and scintillator only gamma above 10% dose was exported while for SRS matrix data were not cutoff. Finally, the number of points analysed for SRS was significantly lower than for the other methods. Furthermore, SRS gamma analysis did not require any change in data resolution. This is one possible reason for the differences in the results obtained.

5.3 TPS VS. PLASTIC SCINTILLATOR

An analysis of the agreement between the dose distribution measured with a plastic scintillator and the dose distribution calculated in the treatment planning system was performed. Table 6 represents gamma index for different dose difference and DTA settings when comparing results from SRS PSD to distribution obtained from TPS Monaco. Table cell colour from green to red is related to value. Green cells have higher values.

Table 6 Gamma index analysis for plastic scintillator. Different DD and DTA were tested. Threshold was set to 10%.

	3%/3mm	3%/2mm	3%/1mm	2%/3mm	2%/2mm	2%/1mm	1%/3mm	1%/2mm	1%/1mm
A081451-3.1	98.4	98.2	97.2	98.1	97.9	96.2	97.8	97.2	98.4
M172343-4.1	100.0	100.0	100.0	99.9	99.8	99.7	99.6	99.5	100.0
M172343-4.2	100.0	99.7	96.6	100.0	99.5	93.2	100.0	99.1	100.0
M172525-1.1	100.0	100.0	100.0	100.0	100.0	100.0	100.0	99.9	100.0
M191092-2.1	100.0	100.0	100.0	100.0	100.0	99.3	100.0	99.9	100.0
M191092-2.2	100.0	99.9	97.9	100.0	99.9	97.2	100.0	99.6	100.0
M191395-1	100.0	100.0	100.0	100.0	100.0	100.0	100.0	100.0	100.0
M200021-1	100.0	100.0	100.0	100.0	100.0	100.0	99.8	99.6	100.0
M200021-2	100.0	100.0	100.0	100.0	100.0	100.0	100.0	100.0	100.0
M200349-1.1	99.4	99.4	98.9	99.3	99.0	98.0	98.3	96.3	99.4
M200349-1.2	100.0	100.0	99.9	99.9	99.7	99.0	99.0	97.9	100.0
M212554-3.1	100.0	99.8	99.2	99.9	99.4	97.0	99.7	98.9	100.0
M212554-3.2	96.1	93.3	86.6	96.0	92.7	83.7	95.7	91.9	96.1
M230270-2.1	100.0	100.0	100.0	100.0	100.0	100.0	100.0	100.0	100.0
M230270-2.2	100.0	100.0	100.0	100.0	100.0	99.9	100.0	100.0	100.0
M230418-2.1	100.0	100.0	100.0	100.0	100.0	99.9	100.0	99.6	100.0
M230418-2.2	100.0	100.0	99.9	100.0	99.9	99.6	99.7	99.4	100.0
M230520-1.1	100.0	100.0	99.9	100.0	100.0	98.6	100.0	100.0	100.0
M230520-1.3	100.0	99.8	98.3	99.9	98.7	95.5	98.4	95.8	100.0
M230520-1.4	100.0	100.0	100.0	99.9	99.8	99.7	99.7	99.6	100.0
M230520-1.5	100.0	100.0	100.0	100.0	100.0	99.7	99.9	99.9	100.0
M230520-1.6	100.0	100.0	100.0	100.0	100.0	100.0	100.0	100.0	100.0
M230520 -1.2	99.9	99.3	97.2	99.8	98.7	93.2	99.5	95.8	99.9
M230541-1.1	100.0	100.0	100.0	100.0	100.0	99.6	100.0	99.9	100.0
M230688-1.1	100.0	100.0	100.0	100.0	100.0	99.3	100.0	100.0	100.0
M230688-1.2	98.1	97.5	96.7	97.3	96.1	92.2	96.4	93.0	98.1
M230704-1.1	100.0	97.8	92.6	100.0	97.3	90.1	100.0	97.2	100.0
M230704-1.2	100.0	100.0	99.5	100.0	100.0	98.4	100.0	100.0	100.0
M231052-1.1	100.0	100.0	99.4	99.8	99.7	99.0	99.5	99.4	100.0
M231118-1.1	100.0	99.7	99.0	99.8	99.1	97.9	99.8	98.9	100.0
M231118-1.2	98.1	96.6	94.7	96.0	94.3	90.7	94.6	92.5	98.1
M231118-1.3	100.0	100.0	100.0	100.0	100.0	100.0	100.0	100.0	100.0
M231118-1.4	80.3	70.2	49.8	80.2	67.0	47.8	80.0	66.5	80.3
M231213-1.1	83.6	70.9	56.9	80.8	66.6	51.4	78.5	63.5	83.6
M231213-1.2	76.8	66.0	48.4	75.1	63.9	43.7	73.7	62.0	76.8
M231248-1.1	100.0	100.0	100.0	100.0	100.0	99.6	99.6	99.1	100.0
M231248-1.2	99.2	99.0	97.8	99.1	99.0	97.0	98.8	98.5	99.2
M232066-1	90.2	86.5	79.5	88.1	81.9	72.2	84.6	77.4	90.2
M232191-1	100.0	99.9	98.5	100.0	99.2	96.4	100.0	98.5	100.0
M232191-2	92.7	86.9	71.4	91.0	84.1	66.2	88.3	80.5	92.7
M232213-1.1	100.0	100.0	99.9	100.0	100.0	97.4	100.0	98.4	100.0
M232213-1.2	100.0	100.0	99.9	99.9	99.4	98.8	98.4	97.2	100.0

Summary table with the number of cases for Gamma Index tolerance limit 90% and 95% are presented in Table 7.

Table 7 Gamma index analysis summary for plastic scintillator for different passing rates.

Pass rate	3%/3mm	3%/2mm	3%/1mm	2%/3mm	2%/2mm	2%/1mm	1%/3mm	1%/2mm	1%/1mm
95%	37	36	35	37	35	31	37	34	23
90%	39	37	36	38	37	36	37	37	32

As shown in Table 7, more than three quarters of the plans met the verification criteria for various gamma parameters except 1%/1 mm. When comparing the results for a mirrored DD/DTA parameters (e.g. 2%/1 mm vs. 1%/2 mm), it was noticed that more fields met the criteria with the looser DTA criterion than with DD.

General statistics for each gamma setting for PSD are presented in Table 8.

Table 8 General statistics for different gamma results for plastic scintillator. Both parametric and nonparametric statistics are presented. Q25 and Q75 stands for quantile 0.25 and 0.75 respectively.

	3%/3mm	3%/2mm	3%/1mm	2%/3mm	2%/2mm	2%/1mm	1%/3mm	1%/2mm	1%/1mm
Average	97.9%	96.7%	94.2%	97.6%	96.0%	92.5%	97.1%	95.1%	89.5%
Standard deviation	5.4%	8.3%	13.2%	5.9%	9.3%	14.4%	6.4%	9.9%	15.6%
Median	100.0%	100.0%	99.7%	100.0%	99.7%	98.5%	99.7%	99.1%	95.7%
Q25	99.6%	99.1%	97.2%	99.4%	98.7%	93.8%	98.4%	96.5%	89.9%
Q75	100.0%	100.0%	100.0%	100.0%	100.0%	99.7%	100.0%	99.9%	98.3%

The results presented in Table 8 include both parametric and non-parametric measures. It's clearly seen that DTA parameter was more challenging for PSD system.

5.4 TPS VS. SRS MATRIX

To compare the developed plastic scintillator system to SRS matrix method gamma analysis has been performed.

Table 9 represent gamma index for different DD and DTA settings when comparing results from SRS MapCHECK to distribution obtained from TPS Monaco. Table cell colour from green to red is related to value. Green cells have higher values.

Table 9 Gamma index analyses for SunNuclear SRSMapCHECK. Different DD and DTA were tested. The threshold was set to 10%.

	3%/3mm	3%/2mm	3%/1mm	2%/3mm	2%/2mm	2%/1mm	1%/3mm	1%/2mm	1%/1mm
A081451-3.1	98.0	97.7	96.2	97.0	96.7	94.4	96.0	95.5	98.0
M172343-4.1	100.0	100.0	97.8	100.0	98.9	96.2	97.8	94.9	100.0
M172343-4.2	100.0	100.0	99.8	99.8	99.8	97.5	99.8	99.3	100.0
M172525-1.1	100.0	100.0	98.4	100.0	100.0	96.4	99.8	99.5	100.0
M191092-2.1	99.5	99.2	96.2	98.6	97.5	95.1	97.8	97.3	99.5
M191092-2.2	100.0	100.0	99.6	100.0	99.8	97.8	99.2	97.8	100.0
M191395-1	100.0	100.0	100.0	100.0	100.0	100.0	100.0	100.0	100.0
M200021-1	99.3	99.3	97.9	97.9	97.2	95.7	97.2	95.7	99.3
M200021-2	100.0	100.0	100.0	100.0	100.0	100.0	100.0	100.0	100.0
M200349-1.1	99.0	98.7	98.0	98.7	98.3	95.1	98.0	96.8	99.0
M200349-1.2	99.9	99.7	99.3	99.9	99.3	97.2	98.5	93.9	99.9
M212554-3.1	100.0	99.8	98.8	99.8	99.8	98.1	99.8	99.2	100.0
M212554-3.2	99.6	99.3	99.3	99.6	99.6	98.5	99.6	99.4	99.6
M230270-2.1	96.5	92.4	85.4	93.4	88.9	78.8	91.9	86.9	96.5
M230270-2.2	99.5	98.4	94.5	98.9	94.5	85.2	96.7	92.9	99.5
M230418-2.1	98.4	98.0	97.6	98.0	98.0	97.1	98.0	96.9	98.4
M230418-2.2	100.0	99.5	98.9	96.7	92.9	86.3	92.1	84.9	100.0
M230520-1.1	100.0	99.8	99.5	99.7	99.5	98.3	99.5	98.8	100.0
M230520-1.3	100.0	100.0	99.6	99.6	99.6	97.1	99.4	98.6	100.0
M230520-1.4	100.0	100.0	100.0	100.0	100.0	100.0	99.6	98.5	100.0
M230520-1.5	99.7	99.5	98.1	98.1	99.5	98.4	98.9	97.8	99.7
M230520-1.6	100.0	100.0	100.0	100.0	100.0	99.2	99.5	99.2	100.0
M230520 -1.2	100.0	100.0	100.0	100.0	100.0	99.8	99.5	99.3	100.0
M230541-1.1	95.7	89.3	79.0	91.4	82.5	71.4	88.9	80.8	95.7
M230688-1.1	100.0	100.0	99.5	99.3	99.5	97.3	99.1	98.6	100.0
M230688-1.2	99.8	99.8	99.8	98.9	98.3	96.4	97.2	95.9	99.8
M230704-1.1	100.0	100.0	100.0	100.0	100.0	100.0	100.0	100.0	100.0
M230704-1.2	100.0	100.0	100.0	100.0	100.0	100.0	100.0	100.0	100.0
M231052-1.1	98.9	98.6	98.3	98.9	98.3	98.3	98.1	97.7	98.9
M231118-1.1	99.3	99.1	96.7	99.1	99.1	98.7	98.9	98.2	99.3
M231118-1.2	99.0	98.0	93.5	98.3	96.3	89.3	96.1	93.5	99.0
M231118-1.3	100.0	100.0	97.0	98.8	98.8	95.3	98.2	98.2	100.0
M231118-1.4	98.7	97.3	93.8	98.2	96.9	91.1	98.2	96.9	98.7
M231213-1.1	98.4	98.4	97.1	98.3	97.3	94.8	96.8	95.9	98.4
M231213-1.2	99.8	99.8	99.7	99.7	99.5	99.2	99.4	98.7	99.8
M231248-1.1	97.7	97.7	96.4	97.4	97.2	94.8	97.2	95.9	97.7
M231248-1.2	97.8	97.8	96.1	97.6	96.8	92.4	95.6	94.4	97.8
M232066-1	100.0	99.8	99.5	99.1	98.8	98.6	98.6	98.2	100.0
M232191-1	99.7	99.3	97.4	98.7	98.4	94.1	97.7	96.4	99.7
M232191-2	100.0	99.7	98.3	99.0	99.0	96.0	98.3	96.6	100.0
M232213-1.1	99.2	96.9	95.6	97.6	93.5	85.8	95.0	87.7	99.2
M232213-1.2	98.0	96.8	93.0	95.3	92.7	84.8	92.7	87.1	98.0

The number of cases for GI passing the passing rate 90% and 95% are presented in Table 10.

Table 10 Gamma index analysis summary for SunNuclear SRS MapCHECK for different passing rates.

Pass rate	3%/3mm	3%/2mm	3%/1mm	2%/3mm	2%/2mm	2%/1mm	1%/3mm	1%/2mm	1%/1mm
95%	42	40	36	40	36	31	38	33	16
90%	42	41	40	42	40	35	41	37	32

As shown in Table 7, more than three quarters of the plans met the verification criteria for various gamma parameters except 1%/1mm for pass rate 95%. When comparing the results for a mirrored DD/DTA parameters (e.g. 2%/1mm vs. 1%/2mm), it was noticed that more fields met the criteria with the looser DTA criterion than with DD. The results were similar to PSD.

General statistics for each gamma setting for SRS MapCHECK are presented in Table 11.

Table 11 General statistics for different gamma results for SRS MapCHECK. Both parametric and nonparametric statistics are presented. Q25 and Q75 stands for quantile 0.25 and 0.75 respectively.

	3%/3mm	3%/2mm	3%/1mm	2%/3mm	2%/2mm	2%/1mm	1%/3mm	1%/2mm	1%/1mm
Average	99.3%	98.8%	97.3%	98.6%	97.7%	94.8%	97.7%	96.0%	91.1%
Standard deviation	1.0%	2.1%	4.0%	1.8%	3.4%	6.1%	2.5%	4.4%	7.0%
Median	99.8%	99.6%	98.3%	99.0%	98.9%	96.8%	98.3%	97.5%	92.5%
Q25	99.0%	98.4%	96.5%	98.1%	97.2%	94.5%	97.2%	95.6%	90.2%
Q75	100.0%	100.0%	99.6%	99.9%	99.8%	98.5%	99.5%	98.8%	95.6%

Obtained results were consistent with the literature:

- Xu et al. reported average passing rate for 3%/ 1mm $99.3 \pm 1.5\%$ and 2%/1 mm is $97.3 \pm 3.2\%$ [117],
- Stedem et al. reported median passing rate dependent for two plan target volumes (3.2 and 35.0 cm^3). Results were presented in Table 12 [118].

Table 12 Reported by Stedem et al. [118] SRS MapCHECK median performance depended on target volume [118]

Target Volume	3%/3mm	3%/2mm	3%/1mm	2%/3mm	2%/2mm	2%/1mm	1%/3mm	1%/2mm	1%/1mm
3.2 cm^3	100	99.7	97.4	100	99.7	95.5	99.4	99.4	91.7
35.0 cm^3	99.7	99.6	98.9	98.9	98.5	95.5	97.5	95.3	89.5

Date presented in Table 11 were consistent with literature except results for DTA=1mm.

5.5 TPS VS. RADIOCHROMIC FILMS

Gafchromic EBT-3 films were used as one of referenced method. Gamma Index results are presented in Table 13. Table cell colour from green to red is related to value. Green cells have higher values.

Table 13 Gamma index analysis for Gafchromic ETB3. Different DD and DTA were tested. The threshold was set to 10%.

	3%/3mm	3%/2mm	3%/1mm	2%/3mm	2%/2mm	2%/1mm	1%/3mm	1%/2mm	1%/1mm
A081451-3.1	82.5	78.8	70.8	79.3	75.5	66.1	77.3	72.9	62.4
M172343-4.1	99.5	99.1	95.9	98.7	97.3	90.4	97.3	94.8	83.0
M172343-4.2	100.0	96.5	71.2	99.9	95.1	65.7	99.9	94.4	62.4
M172525-1.1	97.7	93.8	82.4	93.9	88.4	73.6	91.1	84.2	66.9
M191092-2.1	99.7	99.1	79.6	99.4	98.4	71.9	99.2	97.7	64.2
M191092-2.2	98.9	97.6	91.5	97.4	95.5	86.9	96.0	93.3	81.2
M191395-1	99.9	99.5	98.9	99.1	97.7	95.7	97.2	95.4	90.0
M200021-1	99.0	98.3	97.7	98.5	97.9	96.6	97.8	95.9	93.0
M200021-2	100.0	100.0	100.0	100.0	100.0	99.3	100.0	100.0	95.6
M200349-1.1	99.2	98.2	97.0	96.8	95.3	92.6	94.1	89.8	80.0
M200349-1.2	99.8	98.7	90.9	98.8	97.1	85.4	97.4	93.8	74.4
M212554-3.1	99.5	99.1	98.1	98.8	97.9	94.3	98.4	96.6	90.0
M212554-3.2	99.1	98.6	97.1	98.4	97.8	95.2	97.9	96.8	91.0
M230270-2.1	99.5	98.8	97.5	99.4	98.1	93.7	98.5	95.9	86.9
M230270-2.2	100.0	99.9	99.8	99.7	99.4	96.2	99.2	98.8	89.8
M230418-2.1	98.4	97.9	95.3	97.5	95.7	89.0	95.5	91.2	77.3
M230418-2.2	99.9	98.2	91.9	99.5	95.8	82.7	97.1	90.0	71.1
M230520-1.1	99.5	99.3	95.1	98.4	97.8	89.2	97.9	96.7	83.0
M230520-1.3	99.3	98.4	94.1	98.2	95.7	88.8	96.3	92.2	81.1
M230520-1.4	99.6	99.6	94.3	99.4	99.2	90.2	98.4	97.7	84.2
M230520-1.5	98.5	97.2	95.2	98.0	95.7	91.1	97.2	94.7	86.2
M230520-1.6	99.9	99.8	95.8	99.6	99.5	88.1	99.3	98.5	81.5
M230520-1.2	98.2	96.9	92.0	96.9	95.2	89.1	95.3	92.1	86.2
M230541-1.1	99.0	98.6	97.7	98.8	97.9	95.7	98.5	95.2	87.1
M230688-1.1	98.6	97.0	83.3	97.7	95.3	77.1	96.6	92.7	69.7
M230688-1.2	99.8	98.5	89.0	98.4	95.0	82.5	95.6	90.1	74.7
M230704-1.1	97.9	96.0	91.6	96.9	95.0	88.0	96.2	93.5	84.0
M230704-1.2	99.5	99.1	96.1	99.2	98.6	94.3	99.1	98.2	92.9
M231052-1.1	99.9	99.1	97.0	98.3	95.2	90.0	93.7	89.1	79.0
M231118-1.1	98.3	97.0	93.3	97.8	95.6	88.3	96.9	93.6	81.0
M231118-1.2	100.0	99.9	99.3	99.5	99.0	96.8	98.4	97.4	91.2
M231118-1.3	100.0	100.0	99.2	100.0	100.0	98.5	99.4	99.0	95.9
M231118-1.4	98.6	96.3	90.4	98.4	95.7	89.4	98.3	95.4	88.5
M231213-1.1	99.3	97.3	88.6	98.3	95.1	82.7	96.5	92.3	75.6
M231213-1.2	99.6	97.5	90.7	99.1	95.2	83.8	98.5	92.7	76.3
M231248-1.1	98.4	98.1	93.1	97.7	96.3	89.1	95.2	93.1	81.0
M231248-1.2	97.8	97.0	94.3	97.5	95.8	91.1	95.7	92.6	84.0
M232066-1	84.1	82.4	80.6	80.2	77.7	75.2	56.6	51.3	47.1
M232191-1	99.6	98.6	93.9	98.9	96.3	86.3	96.9	92.1	78.6
M232191-2	99.7	99.1	97.0	98.6	97.5	92.3	95.9	93.0	85.3
M232213-1.1	98.8	98.1	95.6	96.9	95.4	90.4	94.5	92.1	83.0
M232213-1.2	99.9	99.5	98.9	99.0	98.1	95.6	95.7	93.0	85.9

The number of cases for Gamma Index passing rate 90% and 95% are presented in Table 14.

Table 14 Gamma index analysis summary for Gafchromic EBT-3 films for different passing rates.

Pass rate	3%/3mm	3%/2mm	3%/1mm	2%/3mm	2%/2mm	2%/1mm	1%/3mm	1%/2mm	1%/1mm
95%	40	39	21	38	39	9	36	18	2
90%	40	40	34	40	39	20	40	38	9

As shown in Table 14, more than three quarters of the plans met the verification criteria for various gamma parameters except DTA =1 mm. When comparing the results for a mirrored DD/DTA parameters (e.g. 2%/1 mm vs. 1%/2 mm), it was noticed that more fields met the criteria with the looser DTA criterion than with DD. Those difference is much larger than for PSD and SRS.

General statistics for each gamma setting for films are presented in Table 15.

Table 15 General statistics for different gamma results for EBT-3 films. Both parametric and nonparametric statistics are presented. Q25 and Q75 stands for quantile 0.25 and 0.75 respectively.

	3%/3mm	3%/2mm	3%/1mm	2%/3mm	2%/2mm	2%/1mm	1%/3mm	1%/2mm	1%/1mm
Average	98.5%	97.4%	92.7%	97.5%	95.7%	88.1%	95.6%	92.6%	81.0%
Standard deviation	3.5%	4.0%	7.0%	4.2%	4.8%	8.2%	7.1%	7.9%	10.0%
Median	99.5%	98.5%	94.7%	98.5%	96.0%	89.3%	97.2%	93.5%	83.0%
Q25	98.6%	97.2%	91.0%	97.7%	95.3%	85.6%	95.7%	92.2%	76.5%
Q75	99.8%	99.1%	97.1%	99.2%	97.9%	94.2%	98.4%	96.4%	87.0%

The results obtained agree with the values reported in the following publications:

- Kazuki et al. reported 3%/3 mm and 2%/2 mm, median GI 99.3% and 96.4%, respectively [124],
- Chan et al. reported 3%/3 mm and 2%/2 mm average GI 99.3% and 96.4%, respectively [125],
- Saito et al. [126] reported 3%/2 mm average GI 96.6% .

The results presented in Table 15 are consistent with literature data.

5.6 OUTLIERS ANALYSIS

Outlier analysis was performed prior to further analysis. *Outliers* are data observations that fall outside the usual conditional ranges of the response data. Reviewing acquired data from plastic scintillator it is clearly visible that fields plastic scintillator *M232066-1*, *M231118-1.4*, *M231213-1.1* and *M231213-1.2*.

M232066-1

It has been determined that a source of error was the sensor saturation. Raw pixel value was close to its maximum (65,535). Cross section of raw image was presented in Figure 33.

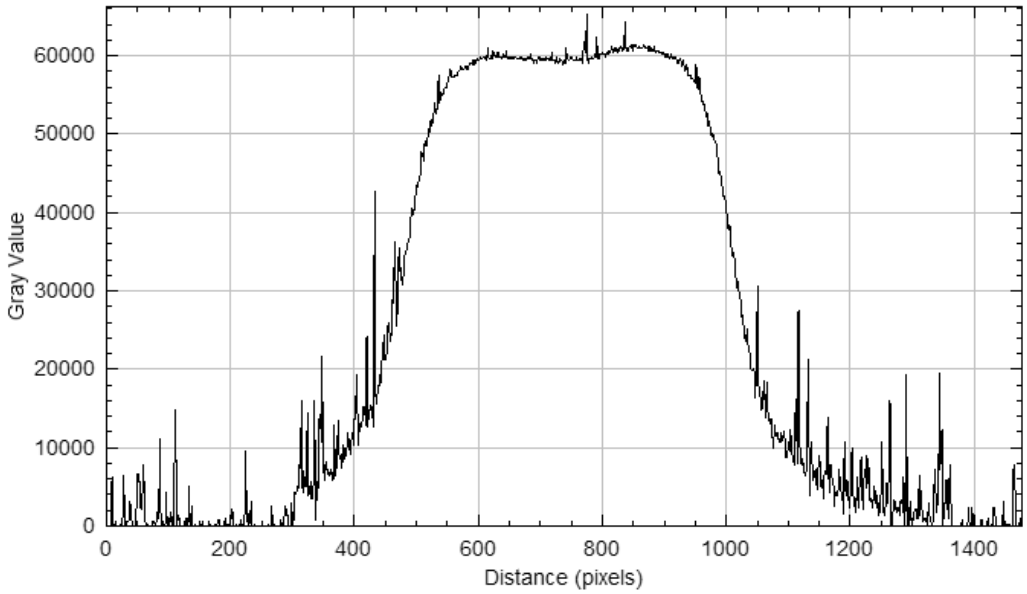

Figure 33 Cross section of plastic scintillator acquired raw image field "M232066-1".

When the pixels reach their maximum value, new scintillations cannot be recorded. This results in the loss of information on the dose delivered to the scintillator. Also, in preliminary results it has been established that sensor readout should be keep at below 80% of its maximum value for better pixel value to dose dependence. For that reason, filed *M232066-1* was excluded from further analysis.

To avoid this situation, the camera's aperture F could be increased from 7.1 to 9. This would allow less light to reach the CMOS sensor without saturating it. A second option would be to reduce the sensitivity, but this was already at the minimum ISO 200 setting.

For film dosimetry the same field was also excluded from further analysis since, according to treatment planning system results, the estimated dose was above 34 Gy which exceeds Gafchromic EBT-3 limits even for a dynamic dose (20 Gy)

M231118-1.4, M231213-1.1 and M231213-1.2

After thorough investigation no reason for gamma result was found. Data was not collected in raw (one by one), camera collection time corresponded to irradiation time, no incidents were noticed during data collection, the sensor was not saturated and images were registered correctly. Data were included in processing.

5.7 GI NORMAL DISTRIBUTION VERIFICATION

In order to choose the correct statistical test, it is necessary to determine whether the data comes from a normal distribution. For this purpose, the Shapiro-Wilk test was used at the significance level of 0.05. Table 16 presents the Shapiro-Wilk test results for EBT-3 film Gamma Index.

Table 16 Test of normality for gamma results for EBT-3 films.

	3%/3mm	3%/2mm	3%/1mm	2%/3mm	2%/2mm	2%/1mm	1%/3mm	1%/2mm	1%/1mm
p Value	0.000	0.000	0.000	0.000	0.000	0.003	0.000	0.000	0.012
W statistic	0.388	0.510	0.819	0.467	0.604	0.904	0.435	0.585	0.927
Hypothesis (α=0.05)	1	1	1	1	1	1	1	1	1

The results showed that the distribution of Gamma Index for PSD departed significantly from normality. Table 17 presents Shapiro-Wilk test results for SRS MapCHECK gamma value.

Table 17 Test of normality for gamma results for SRS MapCHECK.

	3%/3mm	3%/2mm	3%/1mm	2%/3mm	2%/2mm	2%/1mm	1%/3mm	1%/2mm	1%/1mm
p Value	0.000	0.000	0.000	0.000	0.000	0.000	0.000	0.000	0.000
W statistic	0.721	0.585	0.629	0.730	0.659	0.750	0.794	0.764	0.849
Hypothesis (α=0.05)	1	1	1	1	1	1	1	1	1

The results showed that the distribution of Gamma Index for SRS matrix departed significantly from normality.

Table 18 shows Shapiro-Wilk gamma test of the plastic scintillator.

Table 18 Test of normality for gamma results for PSD films.

	3%/3mm	3%/2mm	3%/1mm	2%/3mm	2%/2mm	2%/1mm	1%/3mm	1%/2mm	1%/1mm
p Value	0.000	0.000	0.000	0.000	0.000	0.000	0.000	0.000	0.000
W statistic	0.439	0.441	0.474	0.464	0.469	0.537	0.508	0.533	0.625
Hypothesis (α=0.05)	1	1	1	1	1	1	1	1	1

The results show that the distribution of Gamma Index for PSD departed significantly from normality.

Presented results show that the value of the gamma parameter for the test sample does not come from a normal distribution. Based on this outcome, non-parametric methods were used for the analysis. Based on this outcome, a non-parametric test was used, and the median with the interquartile range were used to summarize the Gamma Index

For better gamma result visualisation in Figure 34 presents a boxplot for each evaluated gamma setting. Due to the lack of normality in gamma distribution median, 25^{th} and 75^{th} quantiles were presented.

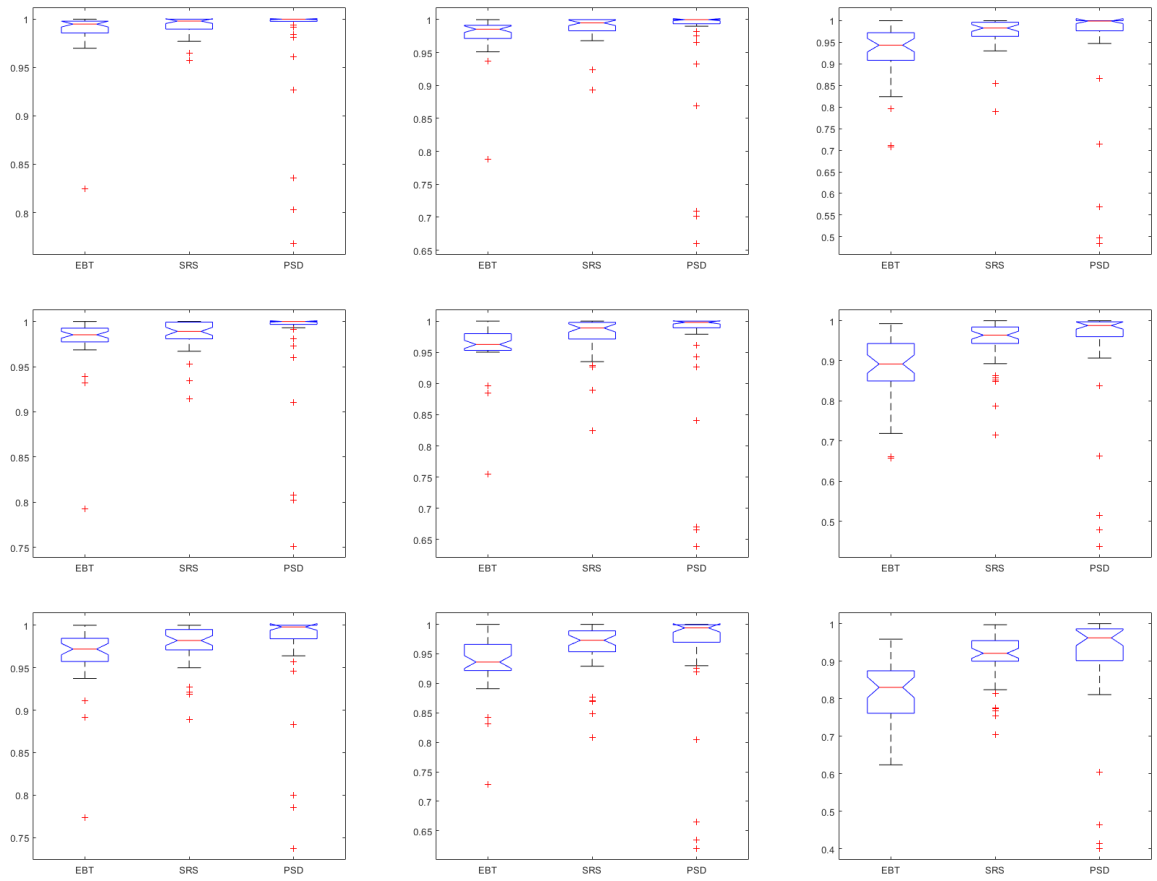

Figure 34 Boxplot for gamma distribution of Gafchromic (EBT), SRS MapCHECK (SRS) and plastic scintillator (PSD) for different gamma setup: left to right DD 1-3%, top to bottom 1-3 mm. Passing rate 95%, threshold 10%. On each plot first result is for Gafchromic EBT-3 film (EBT), second for SMS MapCHECK (SRS) and third for experimental plastic scintillator setup (PSD). On each box, the central mark indicates the median, and the bottom and top edges of the box indicate the 25th and 75th percentiles, respectively. The whiskers extend to the most extreme data points not considered outliers, and the outliers are plotted individually using the '+' marker symbol.

The results visually presented in Figure 34 show the highest number of results not corresponding to the median and 25th and 75th quantities. The largest spread between quantities and extremes was always for EBT.

5.8 INTER METHOD RESULT COMPARISON

All gamma results for each field, for each patient, were binarized based on a tolerance limit equal to 90% and 95%. Compiled results were presented in Table 19 and Table 20 for pass rate 90% and 95%, respectively.

Table 19 Compiled verification output for all methods for tolerance limit 90%.

Method	3%/3mm	3%/2mm	3%/1mm	2%/3mm	2%/2mm	2%/1mm	1%/3mm	1%/2mm	1%/1mm
PSD	39	37	36	38	37	36	37	37	32

SRS	42	41	40	42	40	35	41	37	32
EBT	40	40	34	40	39	20	40	38	9

As it is presented in Table 19 only result for 1%/1 mm are outstanding for all methods. The results for EBT-3 films yields lower number of accepted verifications for DTA=1 mm compared to other methods. PSD results are consistent with SRS.

Table 20 Compiled verification output for all methods for tolerance limit 95%.

Method	3%/3mm	3%/2mm	3%/1mm	2%/3mm	2%/2mm	2%/1mm	1%/3mm	1%/2mm	1%/1mm
PSD	37	36	35	37	35	31	37	34	23
SRS	42	40	36	40	36	31	38	33	16
EBT	40	39	21	38	39	9	36	18	2

As it is presented in Table 20 result for DTA=1 mm are clearly outstanding for all methods. The results for EBT-3 films yields lower number of accepted verifications for DTA=1 mm. PSD results are consistent with SRS across all range of gamma settings.

The first analysis was to check if and for which gamma parameters the results between the three methods did not have a statistically significant difference in results. For this purpose, the Cochran's Q test was applied for dependent variables.

Table 21 Cochran's Q test results for different methods for different gamma parameters for gamma pass rate 90%.

	3%/3mm	3%/2mm	3%/1mm	2%/3mm	2%/2mm	2%/1mm	1%/3mm	1%/2mm	1%/1mm
p Value	0.174	0.223	0.232	0.174	0.607	0.000	0.368	0.926	0.000
Q statistics	3.5	3.0	2.9	3.5	1.0	17.3	2.0	0.2	30.4
Hypothesis (α=0.05)	0	0	0	0	0	1	0	0	1
Pass EBT	40	40	34	40	39	19	39	37	9
Pass SRS	41	40	39	41	39	34	40	36	31
Pass PSD	38	37	36	38	37	36	37	37	33

For the pass rate 90% (Table 21) can be seen from the Cochran's Q test at significance level of α=0.05, the results for all three methods are consistent for all gamma parameters except 2%/1 mm and 1%/1 mm.

Table 22 Cochran's Q test results for different methods for different gamma parameters for gamma pass rate 95%.

	3%/3mm	3%/2mm	3%/1mm	2%/3mm	2%/2mm	2%/1mm	1%/3mm	1%/2mm	1%/1mm
p-Value	0.074	0.368	0.000	0.717	0.549	0.000	0.926	0.000	0.000
Q statistics	5.2	2.0	17.8	0.7	1.2	27.1	0.2	15.7	26.2

Hypothesis (α=0.05)	0	0	1	0	0	1	0	1	1
Pass EBT	40	39	20	38	38	9	36	18	2
Pass SRS	41	39	35	39	35	30	37	32	15
Pass PSD	37	36	36	37	35	32	37	34	24

For a tolerance limit 95% (Table 22) can be seen from the Cochran's Q test at significance level of α=0.05, the results for all three methods are consistent for all gamma parameters except results for DTA equal 1 mm and 1%/2 mm.

Post hoc McNemar test was performed for statistical significance results for post hoc group comparison. Significant post hoc tests will provide evidence of significant differences across methods. McNemar's test by the Chi-squared and corrected for discontinuity were as follows:

For gamma tolerance limit 90%:

- 1%/1 mm
  - EBT-SRS difference with $\chi2(2) = 16.9615$, $p<0.001$,
  - EBT-PSD difference with $\chi2(2) = 18.8929$, $p<0.001$,
- 2%/1 mm
  - EBT-PSD difference with $\chi2(2) = 12.1905$, $p<0.001$,
  - EBT-SRS difference with $\chi2(2) = 7.2593$, $p=0.007$.

For gamma tolerance limit 95%:

- 1%/1 mm
  - EBT-PSD difference with $\chi2(2) = 20.0455$, $p<0.001$,
  - EBT-SRS difference with $\chi2(2) = 9.6$, $p=0.002$,
- 1%/2 mm
  - EBT-PSD difference with $\chi2(2) = 10.2273$, $p=0.001$,
  - EBT-SRS difference with $\chi2(2) = 7.6818$, $p=0.005$,
- 2%/ 1mm
  - EBT-PSD difference with $\chi2(2) = 17.9259$, $p<0.001$,
  - EBT-SRS difference with $\chi2(2) = 13.7931$, $p<0.001$,
- 3%/1 mm
  - EBT-PSD difference with $\chi2(2) = 11.25$, $p=0.001$,
  - EBT-SRS difference with $\chi2(2) = 7.84$, $p=0.005$.

Based on the presented results it was shown that Gafchromic results were statistically significantly different compared to other methods. The presented results allow us to conclude that the gamma analysis for the plastic scintillators is consistent with the results for the SRS MapCHECK matrix for each tested combination of gamma parameters (1-3% and 1-3 mm) and different thresholds: 90% and 95%.

5.9 GI DISTRIBUTION ANALYSIS

The Kruskal-Wallis non-parametric test was used to verify the statistical significance of differences between methods in terms of resulting gamma value. The Post-Hoc Dunn's test using a Bonferroni corrected alpha of 0.017 indicated that the mean ranks of the following pairs are significantly different pairs. Test results for each gamma parameters are presents below. Table 23 present the summary for the Kruskal-Wallis test.

Table 23 Kruskal-Wallis test result summary for gamma value results between different methods.

	3%/3mm	3%/2mm	3%/1mm	2%/3mm	2%/2mm	2%/1mm	1%/3mm	1%/2mm	1%/1mm
p-value	0.068	0.000	0.000	0.000	0.000	0.000	0.000	0.000	0.000
Hypothesis (α=0.05)	1	0	0	0	0	0	0	0	0
Post-Hoc Dunn's significantly different pairs		EBT-PSD	EBT-SRS EBT-PSD	EBT-PSD SRS-PSD	EBT-SRS EBT-PSD	EBT-SRS EBT-PSD	EBT-PSD SRS-PSD	EBT-SRS EBT-PSD	EBT-SRS EBT-PSD

As can be seen based on the Kruskal-Wallis test result, only for the 3%/3 mm gamma parameters can we not reject the null hypothesis that the results come from the same distributions. Based on Dunn's Post Hock test, the results between method EBT and PSD pairs were statistically significant different between for all gamma parameters except 3%/3 mm. The difference between SRS and PSD was statistically significant only for 2%/3 mm and 1%/3 mm.

Based on presented the results it can be concluded that there is no agreement between all three methods. In other words, the difference between the mean ranks of some groups is big enough to be statistically significant. When selecting a value from each of the groups, there are some groups with a higher probability of containing the highest value than others.

Comparing the results presented in Table 24, Table 25 and Table 26, it was noticed that the GI for PSD are closely between the results obtained for EBT and SRS. On the basis of these results it was hypothesised that the absolute difference between PSD to EBT and PSD to SRS is smaller than the difference between EBT and PSD. The null hypothesis H_0 can be written as:

$$H_0: \max\big(abs(PSD - EBT), abs(PSD - SRS)\big) < abs(EBT - SRS). \quad (19)$$

A Wilcoxon signed-rank test was used to verify this hypothesis. Results were presented in Table 27.

Table 27 Wilcoxon signed-rank results to verify hypothesis that GI results for PSD is between EBT and SRS.

	3%/3mm	3%/2mm	3%/1mm	2%/3mm	2%/2mm	2%/1mm	1%/3mm	1%/2mm	1%/1mm
p-value	1.000	1.000	0.999	1.000	1.000	1.000	1.000	1.000	1.000
Hypothesis (α=0.05)	0	0	0	0	0	0	0	0	0
z-val	-4.229	-4.300	-3.166	-4.741	-4.092	-3.503	-4.800	-4.239	-4.186
rank	2.5	24.0	132.0	11.0	52.0	139.5	28.0	71.0	108.0

Results indicated that we cannot reject null hypothesis that the difference between PSD and any referenced methods is smaller than the difference between two EBT and SRS. This would mean that the difference between two referenced methods is larger than the difference between PSD and any of this method.

5.10 POTENTIAL FALSE POSITIVE RESULTS

A false positive result is when a test incorrectly indicates the presence of a condition or attribute that is not actually present. False positives are important because they can skew results and lead to incorrect conclusions. Therefore, it's crucial for methods, tests, or procedures to be designed and implemented in a way that minimises the likelihood of producing false positive results. This is particularly important in radiotherapy where the dose given to the patient cannot be 'undone'. A false positive verification of the patient's plan could lead to an injury.

With the two methods considered as references, the quantitative check for each combination of gamma index parameters and in how many cases the results from the plastic detector are positive while the results from the two reference methods are negative. The results could be treated as a potentially false positive.

Table 28 : The number of potentially false positive results for plastic scintillators. A potentially false positive event is counted when verification with two reference methods is negative while the plastic scintillator is positive.

	3%/3mm	3%/2mm	3%/1mm	2%/3mm	2%/2mm	2%/1mm	1%/3mm	1%/2mm	1%/1mm
Number of potentially false positive results	0	0	0	0	0	6	0	5	13

As shown in Table 28, the developed plastic scintillator system has potential false positive results only for the gamma index analysis with the following parameters: 2%/1 mm, 1%/2 mm and 1%/1 mm. The results indicates applicability limit for PSD.

Table 29 presents result for potentially false negative result for PSD.

Table 29 Number of potentially false negative results for plastic scintillator. Potentially false negative event is counted when verification with two reference methods is positive while plastic scintillator is negative.

	3%/3mm	3%/2mm	3%/1mm	2%/3mm	2%/2mm	2%/1mm	1%/3mm	1%/2mm	1%/1mm
Number of potentially false positive results	0	2	5	2	6	10	4	9	14

The results of the analysis for potential false positives and false negatives show that the use of the PSD for the analysis for 3%/3 mm gamma parameters never gives a potentially false result. For the other parameters, the measurement result of the plastic scintillator is conservative and would lead to a false rejection of the plan rather than a false acceptance.

5.11 GAMMA HISTOGRAM ANALYSIS

One of the disadvantages of the Gamma Index is that when the value of all points under analysis is lower than the tolerance threshold, the gamma value will always be 100%. As a result of such a definition of the coefficient, comparative analysis of two methods using the gamma index is difficult.

The idea of using cumulative gamma histograms (GH) to evaluate plans was presented by Spezi E. and Lewis DG (2006) [127]. One of the examples of the use was the possibility of comparing treatment plans made using different TPS algorithms against the measured dose distribution. The original idea of the authors can also be extended and reversed, i.e. to compare different measurement methods against the treatment planning system.

One of the advantages of GH is that it makes it easy to assess whether the verification of a plan is accepted. The definition of plan acceptance based on the gamma index analysis for a given pass rate P is identical to meeting the condition for the gamma cumulative histogram above P for gamma equal to 1.

Unfortunately, although the article was cited over 50 times, the analysis of gamma histograms did not become common, so it is difficult to compare the obtained GH data with the literature.

For this reason, a GH analysis was performed only for gamma parameters of 2%/2 mm. The results for all tested fields were averaged. For all plans, a cumulative histogram was generated for gamma values for each method. The median and the 25th and 75th quantiles were calculated for each histogram interval over 41 analysed histograms. Resulting histogram was presented in Figure 35.

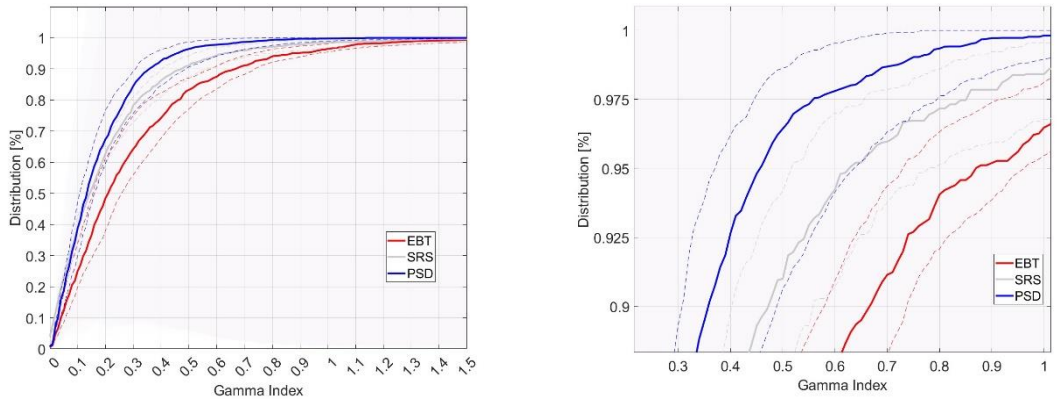

Figure 35 Median cumulative histogram of gamma index for 41 cases analysed with 2%/2 mm. On the right site zoom in for better view on region of interest. Blue colour represents PSD, grey colour SRS MapCHECK and red EBT-3 Gafchromic films. Dashed lines represent 25th and 75th quantiles.

In Figure 35, the y-axis represents the cumulative probability, x-axis the percentile of Gamma Index distribution. The dashed lines represent the 25th and 75th quantiles.

For comparison the results of the GI values for the same analysis are shown in Table 30.

Table 30 Median, 25th and 75th quantiles for gamma index for different methods for DD=2% and DTA=2 mm.

	EBT	SRS	PSD
Median	96.3%	98.4%	99.8%
Q25	95.3%	96.7%	98.9%
Q75	98.1%	99.6%	100.0%

The data presented in Table 30 corresponds to the values of the cumulative gamma index histogram for gamma index values equal to 1 in Figure 35. The results presented in Figure 35 can be interpreted in such a way that statistically the value of the gamma index for the PSD method is lower than for other methods. This means that statistically the PSD method has more points with higher compliance (lower gamma value). The short “tail” for the median above 1 also means a small number of gamma points with values significantly exceeding 1, i.e. strongly inconsistent with the treatment plan.

A two-sample Kolmogorov-Smirnov test was performed to verify the hypothesis that the median cumulative histogram of GI for PSD is higher than for other methods. The results of the Kolmogorov-Smirnov test for PSD vs. EBT and PSD vs. SRS indicated that the PSD results were significantly greater than both EBT ($D^+(300,300) = 0.2400$, $p < 0.0001$) and SRS ($D^+(300,300) = 0.3200$, $p < 0.0001$). These results confirmed the statistical significance of the PSD data presented in Figure 35.

5.12 COST OF EXPERIMENTAL SET-UP

One important but often overlooked aspect of the methods for verifying patients' treatment plans in radiotherapy is the cost. Even the most perfect method with no drawbacks will not be successfully implemented on a large scale if the costs are too high, especially if other methods already exist on the market.

It is a well-known fact that the cost of 2D dosimetry is high. Active electronic systems cost, depending on the manufacturer and equipment, approximately €200,000. These systems, due to their miniaturisation and manufacturing process, require repairs that can cost half the value of a new device in the event of failure.

Much cheaper to purchase are solutions based on Gafchromic films. The cost of a single pack containing 25 sheets of 8" × 10" (20.3 cm × 25.4 cm) film is several thousand Euros plus shipping costs. In addition, a scanner and film analysis software have to be purchased. A package of such a solution costs €20,000-25,000. A single sheet is divided into 4 parts for the exposure of 4 fields. The annual cost of using such a system, assuming the verification of 200 patients, two fields per patient, is approximately €10,000 per year. To compare this with an active matrix and assuming a matrix life of 7 years with intensive use, the total cost of

a film-based solution would be approximately €90,000 compared to approximately €200,000 for a matrix-based solution.

One of the aims of this research was to reduce costs to make it economically viable. The breakdown of costs for building the experimental setup is as follows:

- Camera: €200,
- Scintillator: €1,000,
- Aluminium phantom frame: €250,
- Camera holder: €30,
- PVC foam covers: €100,
- Black paint: €30,
- Acrylic mirror: €20,
- Hinges, glue, and other accessories: €20.

Costs that are not counted include the shielding, since weights were used for this purpose, which are supplied in excess to the accelerator. The total cost was €1,650.

The cost of the scintillator, which is the most expensive component, is the price per 10 sheets. This is due to the fact that the scintillator is made to order and the minimum quantity is exactly €1,000, regardless of the size of the order. For large orders or in-house production, the cost of 1 cm^3 of scintillator is about €1 [128]. The stability of plastic scintillation detectors, understood as the decrease in response with absorbed dose, is about 2%/ kGy. This means that for 200 patients per year with 2 fields per patient at a dose of 2 Gy, the response of the system will decrease by 2% after about 1.5 years.

Camera lifetime exposed to ionizing radiation is unknown. It can be assumed based on lifetime of other electronics that it should be in range 2-5 years. A pessimistic assumption can be made that the camera should be replaced by 3 years.

From economical point of view Capital Expenditure s(CAPEX), Operating Expenses (OPEX) and Total Cost of Ownership (TCO) are commonly used from an economical evaluation.

Table 31 presented summary for those parameters with following assumption:

- Cost was calculated for 10 years period for all three methods. 10 years is an average lifetime linac in Poland. Older linacs are qualified for replacement.

- Current power used by those devices neglectable.
- No warranty and active maintenance.
- OPEX do not include first year costs.
- No computer and license cost is included.

Table 31 Total cost of ownership, operating expense. Prices in euro.

	PSD	**SRS**	**EBT**
TCO	2,050	400,000 (single replacement for 10 years period)	120,000
CAPEX	1,650	200,000	30,000
OPEX	200/ every 3 years	200,000 (single replacement for 10 years period)	10,000 per year

Presented results show excellent price performance of PSD system.

6 DISCUSSION

In radiotherapy, an essential part of the treatment quality control programme is the verification of treatment plans before they are delivered. This involves performing dose measurements in conditions that simulate the actual radiotherapy environment. Such a process provides valuable insight into the question whether the dose has been delivered accurately in terms of dose value and location.

Patient-specific quality assurance requires the development of an appropriate measurement methodology. This involves the use of a practical detector that has been thoroughly tested in various aspects. The suitability of the detector to perform these measurements is also a critical factor to be considered.

The aim of these verification measures is to enable access of any errors in delivery the planned therapy. This ensures that the treatment plan is not only effective, but also safe for the patient. By identifying and correcting potential problems early, healthcare professionals can ensure the highest quality of care for their patients. This comprehensive approach underscores the importance of careful planning and rigorous testing in radiotherapy. It underlines the commitment to patient safety and the pursuit of excellence in treatment outcomes.

Dose distribution gamma index analysis is a critical component of radiotherapy. It provides essential information about the adherence to the planned dose within the intended treatment regimen. This data is twofold, focusing on both the accuracy of the dose delivered and the specific location where that dose is delivered.

Dosimetric verification of patient plans is a standard procedure in the radiotherapy process, as is well documented in medical literature. This routine activity involves a thorough comparison between the dose planned for the patient and the dose actually delivered.

This process ensures that the treatment delivered is exactly what was originally planned, thereby increasing the effectiveness of the therapy and minimising potential risks. By continuously monitoring and verifying dose distribution, healthcare professionals can make necessary adjustments to ensure optimal patient outcomes. This underscores the importance of precision and accuracy in radiotherapy, contributing to the overall success of the treatment programme. This comprehensive approach to patient care underscores the commitment to safety and the pursuit of excellence in therapeutic outcomes in the field of radiotherapy.

From May 2021, experiments dedicated to plastic scintillation detectors were conducted by a PhD candidate at the Radiotherapy Department of the Katowice Oncology Centre. As the

research was conducted at the intersection of many fields, it was preceded by two years of theoretical preparation, which assured the author that the goal of his work would be achieved.

In the first part of the research, components and configurations were experimentally selected and tested to confirm theoretical assumptions and optimise the system. In the second part of the work, the author independently designed and constructed a phantom for research using plastic scintillation detectors and a commercial CMOS camera to verify dynamic stereotactic treatment plans.

This work, in its introduction, stresses the importance of verifying treatment plans and the difficulties associated with it. Particular attention is paid to the verification of dynamic stereotactic plans where, in IMRT or VMAT techniques, a small treatment area receives high doses.

In the second chapter, the main objectives of this work were presented along with detailed objectives, i.e., characterisation of the owned plastic scintillator, examination of the influence of the camera and image processing on the results, and quality control of dynamic stereotactic plans using two methods: reference and the tested system.

The third chapter contains a theoretical discussion. Since the work is at the intersection of many fields, topics such as the basics of radiotherapy, the interaction of ionising photon radiation with matter, the construction of a medical linear accelerator along with a description of dynamic techniques, basic problems, and standards used in the dosimetry of small fields and dynamic fields were discussed. Then, commonly used methods of planar dosimetry, the basics of the operation of the treatment planning system, and individual dosimetric control of plans were presented. The last point of the third chapter gives a description of the gamma index used in PSQA.

The fourth chapter provides a detailed description of the materials and methods used to obtain results and their analysis. Preliminary results of the system were shown, which allowed us to determine the feasibility of the assumed goal. Then, a phantom built for research purposes was discussed in detail, along with its components, i.e., the used CMOS camera, selected plastic scintillator, and shields. Then, reference methods and parameters for which data were collected for these methods were briefly presented. In addition, the selected fields that will be verified by all methods were presented and which will serve to assess whether the tested PSD method gives results that can be considered consistent. The parameters at which the verification plans were recalculated in the treatment planning system were also presented. The last two points of the fourth chapter concerned the tools used to analyse the obtained results.

The research results are presented in the fifth chapter. In the first part, the results of preliminary system tests are explained, which were conducted before the construction of the phantom and were published in the "Polish Journal of Medical Physics and Engineering".

Background and artefacts were thoroughly analysed in the investigated system. Measurement results for different exposure times showed that the system was well isolated from light, with negligible residual light and minimal electronic noise from the camera, ranging from 0.3% to 0.7% of the maximum signal. Higher ISO settings resulted in higher signal background, with electronic noise increasing proportionally with sensitivity changes. At ISO values below 800, background noise was about 1% of the maximum signal.

The signal-to-noise ratio for long exposures remained unaffected by exposure time, with the lowest possible ISO setting recommended. Figure 26 shows no significant difference between the signal below 500 MU and the background, but a clear correlation between dose and signal value for doses equal to or greater than 500 MU, with an R^2 of 0.997. Above 400 MU, an increase in noise of 1.2% of the maximum signal for every 1000 MU was observed.

Stray radiation noise increased rapidly for fields larger than 10×10 cm², while remaining constant for smaller fields. The tested system, equipped with a 10×10 cm² scintillator, showed that noise does not depend on field size for fields smaller than the PSD. For fields larger than 20×20 cm² at ISO 400, signal noise and its standard deviation were 3.7% and 2.7% of the maximum signal, respectively.

Repeatability was high, with normalised mean values ranging from 99.39% to 100.58% and a standard deviation of 0.32% over ten measurements. Single measurement standard deviation averaged 1.18%, attributed to CMOS matrix characteristics. Variations in signal could also be due to plastic film thickness.

For PSD irradiated at different dose rates, the pixel value normalised to the average ranged between 99.45% - 100.37% with a standard deviation of 0.23%. For 6 MV FF and 10 MV FFF beam energies, the values ranged between 99.22% - 100.93% and 99.86% - 100.09% with standard deviations of 0.34% and 0.10%, respectively. The lower standard deviation for 6 MV FF is due to the use of a 5×5 cm² field compared to a 15×15 cm² field for 10 MV FFF.

The signal versus dose response was nonlinear with a higher dose resolution below 50% of the maximum signal. The CMOS sensor's characteristics allowed adjusting light reaching the sensor, optimising the signal-to-noise ratio.

Signal increased with higher ISO value, showing that the system is less sensitive to dose changes at high signal levels. Signal could be multiplied up to 7.9 times comparing ISO 100 to ISO 800 or decreased by up to 20 times comparing aperture *F* 5.6 to *F* 14.

Irradiation of PSDs with different photon energies resulted in different doses due to varying percentage depth dose (PDD) curves. Measurement results maintained dose relationships for different energies, with higher energies delivering lower doses at 2 cm depth. Differences between measured doses and TPS data averaged 0.4%, with a standard deviation of 1.5%, indicating high measurement accuracy.

Comparing MTF50 and MTF10 for Gafchromic film and PSD, films showed 0.6 mm higher resolution and 0.1 mm smaller minimum distinguishable object size. The greater thickness of the plastic detector contributed to its higher beam image blurring. Additional blur was due to optics inaccuracies, image filtering, scintillator surface imperfections, and variations in scintillator thickness.

Obtained preliminary results allowed us to conduct quality assurance for clinical treatment plans in small fields using plastic scintillators, Gafchromic films and SRS 2D matrix detector and compare the results.

In section 5.2 to 5.11, the results for measurements of 42 VMAT fields with all methods and results analysis were presented. Average field size was 55x49 mm^2 and a median dose of 752.9 cGy. Measured doses for all methods were compared with dose plan previously prepared in treatment planning system. Gamma Index analysis for the dose difference in a range 1-3%, a distance-to-agreement in a range 1-3 mm, the threshold set to 10% and the gamma tolerance limit of 90% and 95% was conducted and results were presented.

In Section 5.2, the obtained results were discussed in terms of the number of measurement points. As shown, both for films and plastic scintillators, the average number of points that were compared with the dose distribution from the treatment planning system was about 5.8 times higher. This may worsen the results for these methods due to the need for interpolation and the resulting filtering of results due to the reduction in the size of the analysed images.

In Sections 5.3 to 5.5, the results of the gamma analysis by all methods for all fields in all tested combinations of the gamma parameter were presented. One of the fundamental findings was that the obtained results for films and the SRS matrix were consistent with literature reports. It is crucial to consider the results for these methods used in the study as a reference. This also confirmed that Gamma Index results from SRS MapCHECK and EBT-3 do not have systematic errors introduced either by research or equipment.

Section 5.6 presented outliers analysis for PSD shown that one of the fields has to be rejected because of CMOS matrix saturation.

Gamma Index normality results were presented in section 5.7. Statistical analyses reject hypothesis for GI normality for all groups for all GI settings.

In section 5.8 a non-parametric Cochran Q test was used to answer the question whether the passing rate of examined fields for each method had a statistically significant difference. An additional post hoc McNemar test was performed for statistical significance results for post hoc pair comparison. The results show that for a tolerance limit of 90% all gamma parameters except 2%/1 mm and 1%/1 mm where there are statistically significant differences between groups. For a 95% tolerance limit the Cochran Q test results all use DTA = 1 mm and 1%/2 mm showed statistically significant differences within the group.

Post hoc tests revealed that for both pass rates outstanding pairs were always EBT-PSD and EBT-SRS. This leads to the conclusions that there were statistically significant differences between EBT and two other methods. At the same time the test results show insignificant differences in results for SRS and PSD for all gamma settings.

In section 5.9 GI distribution analyses using the Kursk-Wallis test were presented. The test indicated statistical significance of differences in GI values between all methods except for 3%/3 mm gamma parameters. The post hoc Dunn test revealed that PSD-SRS results were statistically different only for 2%/3 mm and 1%/2 mm. Additionally, Wilcoxon signed rank test showed that GI for the PSD result was statistically between the results for SRS and EBT.

Section 5.10 presented results for potential false positives and false negative results for PSD. Data presented that the PSD results are consecutive and if the PSD yields a result that deviates from the reference methods, then it is a negative result. This is crucial from the clinical point of view. It is significantly safer to erroneously assert that a satisfactory plan does not pass verification than to affirmatively validate an unsatisfactory plan.

GI histogram analysis results for 2%/2 mm gamma settings are presented in section 5.11. Results showed that gamma histogram of median GI for PSD over all cases was statistically “above” other methods. The results presented in Figure 35 were confirmed by the Kolmogorov-Smirnov test. It confirmed that obtained histogram values were greater than for other methods.

In the last section of chapter 5 the total construction costs of the system under study were presented. The PSD system provides exceptional value compared to commercial solutions on all aspects: CAPEX, OPEX and TCO.

Possible improvements

The experimental phantom built was of a proof-of-concept nature, and some of its elements were not optimised. During the experiment with the phantom, certain features were revealed that could be improved upon further development. Potential improvements can be divided into the phantom and the detection system.

Phantom design

The phantom, which is the device used in the experiment could have had its aluminium profiles painted black. This modification would have reduced the amount of scattered light, potentially improving the accuracy of the measurements by minimising reflections of scintillated light.

The mirror could have been reinforced to increase its mechanical stiffness. This improvement would have reduced geometric distortion, thereby improving the accuracy of the reflected images. A stronger mirror is less prone to warping or bending, which can distort the reflected light and affect the quality of the image.

The use of surface mirrors has been considered to eliminate Cherenkov radiation generated in the mirror. By using a surface mirror, the Cherenkov radiation would not be generated in the mirror, thereby improving the quality and accuracy of the measurements.

A certain disadvantage of the applied set is the lack of tissue-like material below the scintillator. On the one hand this causes a lack of dose from backscattered photons, and also it does not block scattered radiation that reaches the scintillator. These geometric conditions were taken into account by the treatment planning system in the scanned phantom geometry, but they introduced unnecessary uncertainty. This was done to reduce elements that could affect the amount of light collected by the system originating from the scintillator and which could affect the geometry. In the further development of the method, tests are considered with the use of transparent acrylic plates or other tissue-like materials placed under the scintillator. The thicknesses of such plates would have to be at least 2 cm. The expected negative effects would be an increase in the signal from Cherenkov radiation, a decrease in signal intensity, additional image blurring, and additional scattering and geometric aberrations associated with a greater number of transitions between media of different optical densities.

Another approach to improve spatial resolution would be to decrease the thickness of the scintillation sheet. A thinner plate would result in less internal scattering and a shorter path for photons to travel, thereby causing ionisation.

In the future, it is also possible to improve radiation shielding to reduce the impact of scattered radiation on the camera electronics, including the CMOS sensor. The following scenarios were considered:

- adding a mobile rear cover to the set – it would protect experiments, but it was not provided due to the need for frequent access to the camera,
- producing custom shields with more conformal geometry and closer to the camera,
- adding a mirror or a system of mirrors resembling a periscope on the camera side so that scattered radiation could not directly hit the camera.

Tests of these modifications and their impact are necessary before their application.

Detection system

The theoretical spatial resolution of the constructed system was 1,160 pixels per 10 cm, resulting in an image resolution distance below 0.1 mm. However, due to noise reduction, including the application of averaging filters, geometric distortions, light scattering within the phantom, and the thickness of the plastic scintillator sheet in which scintillation light is generated, the useful resolution is lower. Considering ways to improve spatial resolution, the first option would be to increase the resolution of the matrix itself. The applied matrix had 12.4 megapixels, while new DSLR camera products have resolutions of 24-36 and in the most expensive models over 50 megapixels (Mpx). This would increase the pixel density by 50-100%, which, without changing the rest of the system, would increase the theoretical resolution to even 0.05 mm. The downside of this solution is higher costs and probably higher noise associated with an increased density of photosensitive elements on the CMOS matrix which is associated with the generation of higher temperature. This is mainly related to the size of the detector used and the physical size of a single pixel on the matrix. In the camera used, the CMOS chip had dimensions of 23.6 × 15.8 mm (APS-C standard). In more expensive models, the matrix is in the "full frame" standard, i.e., 36 × 24 mm like the Nikon D6. This translates into a larger number of pixels on the surface of the CMOS matrix (21.3 vs. 12.4 megapixels), a larger size of a single pixel (41 vs. 30µm), and a reduction in pixel density (2.42 vs. 3.32 Mpx/cm^2). Effectively, cameras with bigger CMOS sensors have fewer problems with the temperature generated by the sensor. Also high-end cameras are designed to handle professional cases, including long exposure times that can last for hours. This is in contrast to a typical Volumetric Modulated Arc Therapy field, which is delivered in less than 5 minutes. These high-end models have advanced features and technologies that effectively manage and

reduce noise, making them suitable for such demanding applications. This is why noise is not a significant issue in these models. Another option would be to use a lens with a larger zoom that could enhance the ratio of the scintillation sheet image. In the existing system, the linear ratio is approximately 1:2.5, a result of minimising lens-induced distortions and maintaining greater lens brightness at a smaller focus parameter. Employing different lenses that could provide a higher focus level of 1:1.5 without diminishing brightness could potentially increase spatial resolution by roughly 70%. The effect mentioned here when changing the lens to a higher model would be greater lens brightness, allowing for a reduction in aperture or measurements with lower ISO, ensuring less thermal noise of the matrix. The lens used in the experiment in the applied system gave a minimum aperture value at the level of f/5.6. Professional lenses such as the 85mm Nikkor Z have brightness levels of f/1.2, which would translate into more than a 4-fold increase in the amount of light reaching the matrix, which would allow for increased sensitivity for short exposures and increased aperture for long exposures, eliminating some lens distortions.

Another possible modification that can be seen is the improvement of the reading system. In the experiment carried out, the data was stored on an SDHC card in the camera, and in order to read the collected images, the card had to be removed from the camera. This required entering the bunker and fiddling with the camera, which could potentially affect its positioning or lens alignment. If a fixed cable or wireless connection had been used, this would not have been necessary and the collected images could have been analysed and evaluated immediately after irradiation.

The final modification would be to connect a permanent power supply to the camera. This would not directly affect the quality of the results, but not having to remove the camera from the tripod to change the battery would minimise the risk of misalignment when reassembled.

These modifications could significantly enhance the system’s performance and resolution capabilities. The cost of such modifications, although they would significantly increase the cost of the system, would still be incomparably lower than commercial solutions.

7 CONCLUSIONS

Quality assurance is pivotal in the implementation of advanced radiotherapy techniques such as IMRT, VMAT, and stereotactic radiation therapy (SBRT/SRS/SART/SRT). The detection of errors at various stages of treatment is crucial to prevent harm to patients. Patient-specific quality assurance, PSQA, plays a vital role in ensuring the accuracy and safety of the treatment process.

The thesis resulted in the construction of a cost-effective system designed to validate dynamic treatment plans for small areas. Analysis of the results revealed that the Gamma Index values for the investigated PSD statistically fell within the range of the results obtained with the reference methods. Importantly, no potential false positives, which could pose a significant clinical risk, were detected. The GI analysis for a distance-to-agreement of 1 mm was identified as the limit of the method's applicability. In this context, the results were statistically significant relative to and between the reference methods. However, it remained undetermined which method more accurately reflected the actual dose distribution relative to the treatment planning system.

The developed plastic scintillator detector, PSD, maintained an accuracy comparable to radiochromic films and high-resolution active detector matrices, making it suitable for verifying dynamic, high-dose plans typically used for stereotactic treatments. The results obtained, coupled with the low cost and simplicity of the system, suggest that the proposed system with the use of a plastic scintillator is a potential solution for PSQA in radiotherapy. This solution yields results comparable to those of radiochromic films and active detector arrays.

8 REFERENCES

[1] H. Sung, J. Ferlay, R. Siegel, M. Laversanne, I. Soerjomataram, A. Jemal and F. Bray, "Global Cancer Statistics 2020: GLOBOCAN Estimates of Incidence and Mortality Worldwide for 36 Cancers in 185 Countries," *CA: a cancer journal for clinicians,* vol. 71, no. 3, pp. 209-249, 2021.

[2] R. Baskar, K. A. Lee, R. Yeo and K. W. Yeoh, "Cancer and radiation therapy: current advances and future directions," *International Journal of Medical Sciences,* vol. 9, no. 3, pp. 193-9, 2012.

[3] K. Składowski, "Raport na temat stanu radioterapii w Polsce na dzień 31.12.2022 r.," Gliwice, 2023.

[4] U. Ringborg, D. Bergqvist, B. Brorsson, E. Cavallin-Ståhl, J. Ceberg, N. Einhorn, J. E. Frödin, J. Järhult, G. Lamnevik, C. Lindholm, B. Littbrand, A. Norlund, U. Nylén, M. Rosén, H. Svensson and T. Möller, "The Swedish Council on Technology Assessment in Health Care (SBU) systematic overview of radiotherapy for cancer including a prospective survey of radiotherapy practice in Sweden 2001-summary and conclusions," *Acta oncologica,* vol. 42, no. 5-6, pp. 357-365, 2003.

[5] A. C. Begg, F. A. Stewart and C. Vens, "Strategies to improve radiotherapy with targeted drugs," *Nature Reviews Cancer,* vol. 11, no. 11, p. 239–253, 2011.

[6] G. C. Barnett, C. M. West, A. . Dunning, R. M. Elliott, C. E. Coles, P. D. Pharoah and N. G. Burnet, "Normal tissue reactions to radiotherapy: towards tailoring treatment dose by genotype," *Nature Reviews Cancer,* vol. 9, no. 2, p. 134–142, 2009.

[7] S. D. McGrath, M. M. Matuszak, D. Yan, L. L. Kestin, A. A. Martinez and I. S. Grills, "Volumetric modulated arc therapy for delivery of hypofractionated stereotactic lung radiotherapy: A dosimetric and treatment efficiency analysis," *Radiotherapy and Oncology,* pp. Vol. 95, I.2, 153-157, 2010.

[8] P. Navarria, A. M. Ascolese, P. Mancosu, F. Alongi, E. Clerici, A. Tozzi, C. Iftode, G. Reggiori, S. Tomatis, M. Infante, M. Alloisio, A. Testori, A. Fogliata, L. Cozzi, E. Morenghi and M, "Volumetric modulated arc therapy with flattening filter free (FFF) beams for stereotactic body radiation therapy (SBRT) in patients with medically

inoperable early stage non small cell lung cancer (NSCLC)," *Radiotherapy and Oncology*, vol. 107, no. 3, pp. 414-418, 2013.

[9] J. E. Niederhuber, J. O. Armitage, J. H. Doroshow, M. B. Kastan and J. E. Tepper, Abeloff's Clinical Oncology, Elsevier, 2020.

[10] I. J. Das, G. X. Ding and A. Ahnesjö, "Small fields: Nonequilibrium radiation dosimetry," *Medical Physics,* vol. 35, no. 1, p. 206–215, 2008.

[11] A. J. D. Scott, A. E. Nahum and J. Fenwick, "Using a Monte Carlo model to predict dosimetric properties of small radiotherapy photon fields," *Medical physics,* vol. 35, no. 10, p. 4671–84, 2008.

[12] A. Mack, S. G. Scheib, J. Major, S. Gianolini, G. Pazmandi and H. Feist, "Precision dosimetry for narrow photon beams used in radiosurgery-determination of Gamma Knife output factors," *Medical Physics,* vol. 29, no. 9, p. 2080–9, 2002.

[13] F. Sánchez-Doblado, P. Andreo, R. Capote, A. Leal, M. Perucha and A. R. , "Ionization chamber dosimetry of small photon fields: A Monte Carlo study on stopping-power ratios for radiosurgery and IMRT beams," *Physics in medicine and biology,* vol. 48, no. 14, p. 2081–99, 2003.

[14] C. S. Calcina, L. N. de Oliveira, C. E. de Almeida and A. de Almeida, "Dosimetric parameters for small field sizes using Fricke xylenol gel, thermoluminescent and film dosimeters, and an ionization chamber," *Physics in medicine and biology,* vol. 52, no. 5, p. 1431–9, 2007.

[15] G. X. Ding, D. M. Duggan and C. W. Coffey, "Commissioning stereotactic radiosurgery beams using both experimental and theoretical methods," *Physics in Medicine and Biology,* no. 2549–66, p. 51, 2006.

[16] M. Westermark, J. Arndt, B. Nilsson and A. Brahme, "Comparative dosimetry in narrow high-energy photon beams," *Physics in medicine and biology,* vol. 45, no. 3, p. 685–702, 2000.

[17] N. C. Ikoro, D. A. Johnson and P. P. Antich, "Characteristics of the 6-MV photon beam produced by a dual energy linear accelerator," *Medical physics,* vol. 14, no. 1, p. 93–7, 1987.

[18] D. O. Findley, B. W. Forell and P. S. Wong, “Dosimetry of a dual photon energy linear accelerator,” *Medical Physics,* vol. 14, p. 270–3, 1987.

[19] I. Griessbach, M. Lapp, J. Bohsung, G. Gademann and D. Harder, “Dosimetric characteristics of a new unshielded silicon diode and its application in clinical photon and electron beams,” *Medical physics,* vol. 32, no. 13, p. 3750–4, 2005.

[20] C. McKerracher and D. Thwaites, “Assessment of new small-field detectors against standard-field detectors for practical stereotactic beam data acquisition,” *Physics in medicine and biology,* vol. 44, no. 9, p. 2143–60, 1999.

[21] W. T. Laub WU, “The volume effect of detectors in the dosimetry of small fields used in IMRT,” *Medical Physics,* no. 30, p. 341–7, 2003.

[22] C. H. Sibata, H. C. Mota, A. S. Beddar, P. D. Higgins and K. H. Shin, “Influence of detector size in photon beam profile measurements,” *Physics in Medicine & Biology,* vol. 36, no. 5, p. 621–31, 1991.

[23] W. Parwaie, S. Refahi, M. A. Ardekani and B. Farhood, "Different Dosimeters/Detectors Used in Small-Field Dosimetry: Pros and Cons," *Journal of medical signals and sensors,* vol. 8, no. 3, p. 195–203, 2018.

[24] P. Olko, . Marczewska, L. Czopyk, M. A. Czermak , M. Kłosowski and M. P. R. Waligórski, “New 2-D dosimetric technique for radiotherapy based on planar thermoluminescent detectors,” *Radiation Protection Dosimetry,* vol. 118, no. 2, p. 213–218, 2006.

[25] A. L. Palmer, A. Dimitriadis, A. Nisbet and C. H. Clark, “Evaluation of gafchromic EBT-XD film, with comparison to EBT3 film, and application in high dose radiotherapy verification,” *Physics in medicine and biology,* vol. 60, no. 22, p. 8741–52, 2015.

[26] E. Infusino, A. Ianiro, S. Luppino, S. Nocentini, C. Pugliatti and A. Soriani, “Evaluation of a planar diode matrix for SRS patient-specific QA in comparison with Gafchromic films,” *Journal of Applied Clinical Medical Physics,* vol. 24, no. 8, p. e13947, 2023.

[27] D. A. Low, J. M. Moran, J. F. Dempsey, L. Dong and M. Oldham, “Dosimetry tools and techniques for IMRT,” *Medical Physics,* vol. 38, no. 3, pp. 1313-38, 2011.

[28] D. A. Low, W. B. Harms, S. Mutic and J. A. Purdy, “A technique for the quantitative evaluation of dose distributions,” *Medicla Physics,* vol. 25, no. 5, pp. 656-61, 1998.

[29] J. M. Park, J. Kim, S. Y. Park, D. H. Oh and S. T. Kim, “Reliability of the gamma index analysis as a verification method of volumetric modulated arc therapy plans,” *Radiat Oncol 13*, vol. 13, no. 175, p. 175, 2018.

[30] S. Devic, N. Tomic and D. Lewis, “Reference radiochromic film dosimetry: Review of technical aspects,” *Phys Med,* vol. 32, p. 541–556, 2016.

[31] H. L. Yu-hao, N. Hardcastle, M. Bailey, S. Siva, A. Seeley, T. Barry, J. Booth, L. Lao, M. Roach, S. Buxton, D. Thwaites and M. Foote, “Guidelines for safe practice of stereotactic body (ablative) radiation therapy,” *Journal of Medical Imaging and Radiation Oncology,* vol. 59, no. 5, pp. 646-653, 2015.

[32] A. Sahgal, D. Roberge, D. Schellenberg, T. G. Purdie, A. Swaminath, J. Pantarotto, E. Filion, Z. Gabos, J. Butler, D. Letourneau, G. L. Masucci, L. Mulroy, A. Bezjak, L. A. Dawson and P. M, “The Canadian association of radiation oncology scope of practice guidelines for lung, liver and spine stereotactic body radiotherapy,” *Clin Oncol (R Coll Radiol),* vol. 24, no. 9, pp. 629-639, 2012.

[33] P. H. Halvorsen, E. Cirino, I. J. Das, J. A. Garrett, J. Yang, F. F. Yin and L. A. Fairobent, “AAPM-RSS Medical Physics Practice Guideline 9.a. for SRS-SBRT,” *Journal of Applied Clinical Medical Physics,* vol. 18, no. 5, pp. 10-21, 2017.

[34] M. D. M. P. J. Abramoff and S. J. Ram, “Image Processing with ImageJ,” vol. 11, no. 7, pp. 36-42, 2004.

[35] K. Kostrzewska, K. Labunets, R. Plisko, M. Libura and A. Chrobak, "Dostęp pacjentów onklogicznych do terapii lekowych," ALIVIA Fundacja Onkologiczna, Kraków, 2023.

[36] K. Herman, “Chirurgiczne leczenie nowotworów w Polsce: dziś i jutro,” *Onkologia w Praktyce Klinicznej,* vol. 7, no. 6, pp. 311-320, 2011.

[37] R. Baskar, K. A. Lee, R. Yeo and K.-W. Yeoh, “Cancer and Radiation Therapy: Current Advances and Future Directions,” *International Journal of Medical Sciences,* vol. 9, no. 3, p. 193–199, 27 Feb 2012.

[38] I. El Naqa, J. Bradley, A. I. Blanco, P. E. Lindsay, M. Vicic, A. Hope and J. O. Deasy, "Multivariable modeling of radiotherapy outcomes, including dose-volume and clinical factors," *International journal of radiation oncology, biology, physics,* vol. 64, no. 4, pp. 1275-86, 15 March 2006.

[39] J. Rigley, P. Robertson and L. Scattergood, "Radiotherapy without tattoos: Could this work?," *Radiography,* vol. 26, no. 4, pp. 288-293, 2020.

[40] E. B. Podgorsak, Radiation Oncology Physics: A Handbook for Teachers and Students, Viena: International Atomic Energy Agency, 2005.

[41] "General principles for the radiation protection of workers," *Annals of the ICRP,* vol. 27, no. 1, pp. 1-60, 1997.

[42] "Tissue substitutes in radiation dosimetry and measurement," *International Commission on Radiation Units and Measurements ICRU,* vol. 44, 1989.

[43] C. A. Jayachandran, "Calculated effective atomic number and kerma values for tissue-equivalent and dosimetry materials," *Physics in Medicine & Biology,* vol. 16, no. 4, pp. 17-23, 1971.

[44] IAEA, Absorbed Dose Determination in External Beam Radiotherapy, Technical Reports Series No. 398 (Rev.1), Viena: IAEA, 2024.

[45] C. X. Yu, "Intensity-modulated arc therapy with dynamic multileaf collimation: an alternative to tomotherapy," *Physics in medicine and biology,* vol. 40, no. 9, pp. 1435-49, Sep 1995.

[46] S. K. Das Majumdar, A. Amritt, S. S. Dhar, S. Barik, S. S. Beura, T. Mishra, D. K. Muduly, A. Dash and D. K. Parida, "A Dosimetric Study Comparing 3D-CRT vs. IMRT vs. VMAT in Left-Sided Breast Cancer Patients After Mastectomy at a Tertiary Care Centre in Eastern India," *Cureus,* vol. 14, no. 3, p. e23568, Mar 2022.

[47] J. L. Bedford, "Treatment planning for volumetric modulated arc therapy," *Medical Physics,* vol. 36, no. 11, pp. 5128-38, Nov 2009.

[48] A. Holt, D. V. Gestel, M. P. Arends, E. W. Korevaar, D. Schuring, M. C. Kunze-Busch, R. J. Louwe and C. van Vliet-Vroegindeweij, "Multi-institutional comparison of volumetric modulated arc therapy vs. intensity-modulated radiation therapy for head-and-neck cancer: a planning study," *Radiation Oncology,* vol. 8, no. 26, pp. 8-26, 31 January 2013.

[49] D. A. Low, J. M. Moran, J. F. Dempsey, L. Dong and M. Oldham, "Dosimetry tools and techniques for IMRT," *Medical Physics,* vol. 38, pp. 1313-1338, 2011.

[50] M. Alber, S. Broggi, C. D. De Wagter, I. Eichwurzel, P. Engström and C. Fiorino, ESTRO Booklet 9: Guidelines for the Verification of IMRT, Brussels: ESTRO Publications, 2008.

[51] K. Woźniak, “Dosimetric verification of dynamic radiotherapy treatment planning VMAT,” *Inżynier i Fizyk Medyczny,* vol. 4, no. 3, pp. 147-152, 2015.

[52] M. J. Butson, P. K. Yu, T. Cheung and P. Metcalfe, “Radiochromic film for medical radiation dosimetry,” *Materials Science and Engineering,* pp. 61-120, 2003.

[53] C. G. Soares, “Radiochromic film dosimetry,” *Radiation Measurements,* vol. 41, no. 1, pp. S100-S116, 2006.

[54] I. J. Das, Radiochromic Film: Role and Applications in Radiation Dosimetry, CRC Press, 2018.

[55] S. Pai, I. J. Das, J. F. Dempsey, K. L. Lam, T. J. LoSasso, A. J. Olch, J. R. Palta, L. E. Reinstein, D. Ritt and E. E. Wilcox, “TG-69: Radiographic film for megavoltage beam dosimetry,” *Medical Physics,* vol. 34, pp. 2228-2258, 2007.

[56] B. Mijnheer, Clinical 3D Dosimetry in Modern Radiation Therapy, CRC Press, 2018.

[57] “Gafchromic EBT-3,” [Online]. Available: http://www.gafchromic.com/documents/EBT3_Specifications.pdf.

[58] M. Diaz, M. Rogelio, D. Venencia, E. Garrigo and Y. Pipman, "A method to enhance 2D ion chamber array patient specific quality assurance for IMRT," *Australasian physical & engineering sciences in medicine,* vol. 41, no. 4, pp. 145-151, Mar 2017.

[59] A. Bruschi, Esposito, M, S. Pini, A. Ghirelli, G. Zatelli and S. Russo, "How the detector resolution affects the clinical significance of SBRT pre-treatment quality assurance results," *Physica medica,* vol. 49, pp. 129-134, May 2018.

[60] L. D. Wolfsberger, M. Wagar, P. Nitsch, M. S. Bhagwat and P. Zygmanski, “Angular dose dependence of MatriXX TM and its calibration,” *Journal of Applied Clinical Medical Physics,* vol. 11, no. 1, p. 241–51, 2010.

[61] Y. Shimohigashi, F. Araki, H. Tominaga, J. Sakata, K. Kawasaki, N. Kanetake, Y. Iwashita, S. Yoshimura, T. Kawakami, T. Ishihara, T. Okuda and K. Kogo, “Angular dependence correction of MatriXX and its application to composite dose verification,” *Journal of Applied Clinical Medical Physics,* vol. 13, no. 5, pp. 198-214, 2012.

[62] Q. Xu, K. Huynh, W. Nie, M. S. Rose, A. K. Chawla, K. S. Choe, S. Kanani, G. J. Kubicek and F. J, “Implementing and evaluating a high-resolution diode array for patient-specific quality assurance of robotic brain stereotactic radiosurgery/radiotherapy,” *Radiation Oncology Physics,* vol. 23, no. 5, p. e13569, 2024.

[63] E. Seravalli, A. C. Houweling, L. V. Battum, T. A. Raaben, M. Kuik, J. A. d. Pooter, M. P. V. Gellekom, J. Kaas, W. d. Vries, E. A. Loeff and J. B. V. d. Kamer, "Auditing local methods for quality assurance in radiotherapy using the same set of predefined treatment plans," *Physics and Imaging in Radiation Oncology,* vol. 5, pp. 19-25, 2018.

[64] A. Mans, D. Schuring, M. P. Arends, C. A. J. M. Vugts, J. W. H. Wolthaus, H. T. Lotz, M. Admiraa, R. J. W. Louwe, M. C. Öllers and J. B. v. d. Kamer, "The NCS code of practice for the quality assurance and control for volumetric modulated arc therapy," *Physics in Medicine & Biology,* vol. 61, no. 19, pp. 7221-7235, 2015.

[65] J. Winiecki, Graficzna weryfikacja radioterapii IMRT na podstawie współczynnika gamma, Gliwice: Centrum Onkologii - Instytut im. Marii Skłodowskiej-Curie Oddział w Gliwicach, 2012.

[66] S. Das, V. Kharade, V. P. Pandey, A. Kv, R. K. Pasricha and M. Gupta, "Gamma Index Analysis as a Patient-Specific Quality Assurance Tool for High-Precision Radiotherapy: A Clinical Perspective of Single Institute Experience," *Cureus,* vol. 14, no. 10, 2022.

[67] A. Yusuke, S. Iori, K. Yu, K. Satoshi, K. Masahiko, U. Yoshihiro, O. Yuki, N. Yuichiro, K. Ryu, A. Kazuhiko, K. Takahiro and N. Mitsuhiro, "Assessment of using a gamma index analysis for patient-specific quality assurance in Japan," *Journal of applied clinical medical physics,* vol. 23, no. 10, p. e13745, 2022.

[68] D. A. Low and J. F. Dempsey, “Evaluation of the gamma dose distribution comparison method,” *Medical Physiscs,* vol. 30, no. 9, pp. 2455-64, 2003.

[69] M. Isa Khan, M. Shakil, , M. B. . Tahir, M. Rafique, T. Iqbal, A. Zahoor, J. ur Rehman, I. Iqbal and J. L. Chow, "Selection of Gamma Analysis Acceptance Criteria in IMRT QA Using Gafchromic EBT3 Film Dosimetry," *Journal of Radiotherapy in Practice,* vol. 18, no. 2, p. 127–31, 2019.

[70] M. Atiq, A. Atiq, K. Iqbal, Q. a. Shamsi, F. Andleeb and S. A. Buzdar, “Interpretation of Gamma Index for Quality Assurance of Simultaneously Integrated Boost (SIB) IMRT

Plans for Head and Neck Carcinoma," *Polish Journal of Medical Physics and Engineering,* vol. 23, no. 4, pp. 93-97, 2017.

[71] G. A. Ezzell, J. W. Burmeister, N. Dogan, T. J. LoSasso, J. G. Mechalakos, D. Mihailidis, A. Molineu, J. R. Palta, C. R. Ramsey, B. J. Salter, J. Shi, P. Xia, N. Yue and Y. Xiao, "IMRT commissioning: multiple institution planning and dosimetry comparisons, a report from AAPM Task Group 119," *Medical physics,* vol. 36, p. 5359–5373, 2009.

[72] M. Miften, A. Olch, D. Mihailidis, J. Moran, T. Pawlicki, A. Molineu, H. Li, K. Wijesooriya, J. Shi, P. Xia and N. a. L. D. Papanikolaou, "Tolerance limits and methodologies for IMRT measurement-based verification QA: Recommendations of AAPM Task Group No. 218," *Medical Physics,* vol. 45, no. 4, pp. e53-e83, April 2018.

[73] A. Fredh, J. B. Scherman, L. S. Fog and P. . Munck af Rosenschöld, "Patient QA systems for rotational radiation therapy: a comparative experimental study with intentional errors," *Medical Physics,* vol. 40, no. 3, 2013.

[74] G. Heilemann, B. Poppe and W. Laub, "On the sensitivity of common gamma-index evaluation methods to MLC misalignments in Rapidarc quality assurance," *Medical Physics,* vol. 40, no. 3, p. 031702, 2013.

[75] S. Beddar and L. Beaulieu, Scintillation Dosimetry, CRC Press, 2016.

[76] W. L. Buck, "The origin of scintillations in organic materials," *IRE Transactions on Nuclear Science,* p. 11–16, 1960.

[77] J. B. Birks, "The Theory and Practice of Scintillation Counting," 1964.

[78] J. B. Birks, "Scintillation Efficiency of Anthracene Crystals," *Proceedings of the Physical Society,* vol. 63, no. 11, p. 1294, 1950.

[79] J. B. Birks and M. E. Szendrei, "The Absolute Scintillation Efficiency of Anthracene," *Physical Review,* 1953.

[80] R. L. Craun and D. L. Smith, "Analysis of response data for several organic scintillators," *Nuclear Instruments and Methods,* vol. 80, no. 2, pp. 239-244, 1970.

[81] D. L. Smith, R. G. Polk and T. G. Miller, "Measurement of the response of several organic scintillators to electrons, protons, and deuterons," *Nuclear Instruments & Methods,* vol. 64, no. 2, pp. 157-166, 1968.

[82] A. Jirasek and C. Duzenli, "Relative effectiveness of polyacrylamide gel dosimeters applied to proton beams: Fourier transform Raman observations and track structure calculations," *Medical Physics,* vol. 29, no. 4, pp. 569-577, 2002.

[83] T. Pöschl, D. Greenwald, M. J. Losekamm and S. Paul, "Measurement of ionization quenching in plastic scintillators," *Nuclear Instruments and Methods in Physics Research,* vol. 988, 2021.

[84] H. Palmans, P. Andreo, M. S. Huq, J. Seuntjens, K. E. Christaki and A. Meghzifene, "Dosimetry of small static fields used in external photon beam radiotherapy: Summary of TRS-483, the IAEA-AAPM international Code of Practice for reference and relative dose determination," *Medical physics,* vol. 45, no. 11, p. e1123–e1145, 2018.

[85] G. Valdes Santurio and C. Andersen, "Quantifying the ionization quenching effect in organic plastic scintillators used in MV photon dosimetry," *Radiation Measurements,* 10 2019.

[86] A. S. Beddar, "Water-equivalent plastic scintillation detectors for high-energy beam dosimetry: I. Physical characteristics and theoretical considerations," *Physics in Medicine & Biology,* vol. 37, no. 10, p. 1883, 1992.

[87] H. E. Johns and J. R. Cunningham, The Physics of Radiology. 4 Edition, Springfield, 1983.

[88] A.-M. Frelin, J.-M. Fontbonne, G. Ban, J. Colin and M. Labalme, “Comparative Study of Plastic Scintillators for Dosimetric Applications,” *Nuclear Science, IEEE Transactions on. 55,* pp. 2749-2756, 2008.

[89] J. F. Williamson, J. F. Dempsey, A. S. Kirov, J. I. Monroe, W. R. Binns and H. Hedtjärn, “Plastic scintillator response to low-energy photons,” *Physics in Medicine & Biology,* vol. 44, no. 4, p. 857, 1999.

[90] M. A. Clift, R. A. Sutton and W. D. V, “Dealing with Cerenkov radiation generated in organic scintillator dosimeters by bremsstrahlung beams,” *Physics in Medicine & Biology,* vol. 45, no. 5, p. 1165, 2000.

[91] S. A. Beddar, T. M. Briere, F. A. Mourtada, O. N. Vassiliev, L. H. H and M. Radhe, “Monte Carlo calculations of the absorbed dose and energy dependence of plastic

scintillators," *American Association of Physicists in Medicine,* vol. 32, no. 5, pp. 1265-1269, 2005.

[92] J. Lambert, T. Nakano, S. Law, J. Elsey, D. McKenzie and N. Suchowerska, "In vivo dosimeters for HDR brachytherapy: a comparison of a diamond detector, MOSFET, TLD, and scintillation detector," *Medical Physics,* vol. 34, no. 5, pp. 1759-65, 2007.

[93] W. Busjan, K. Wick and T. Zoufal, "Shortlived absorption centers in plastic scintillators and their inuence on the fluorescence light yield," *Nuclear Instruments and Methods in Physics Research Section B: Beam Interactions with Materials and Atoms,* vol. 152, no. 1, pp. 89-104, 1999.

[94] M. M. Aspradakis, J. P. Byrne, H. Palmans, S. Duane, J. Conway, A. P. Warrington and K. Rosser, IPEM report 103: Small field MV photon dosimetry, International Atomic Energy Agency, 2010.

[95] L. E. Cartwright, J. Lambert, D. R. McKenzie and N. Suchowerska, "The angular dependence and effective point of measurement of a cylindrical scintillation dosimeter with and without a radio-opaque marker for brachytherapy," *Physics in Medicine & Biology,* vol. 54, no. 7, p. 2217, 2009.

[96] L. Archambault, A. Beddar, L. Gingras, F. Lacroix, R. Roy and L. Beaulieu, "Water-equivalent dosimeter array for small-field external beam radiotherapy," *Medical physics,* vol. 34, pp. 1583-92, 2007.

[97] J. V. Jelley, Cerenkov Radiation And Its Applications, Pergamon Press, 1958.

[98] S. F. Boer, A. S. Beddar and J. A. Rawlinson, "Optical filtering and spectral measurements of radiation-induced light in plastic scintillation dosimetry," *Physics in Medicine & Biology,* vol. 28, no. 7, p. 945, 1993.

[99] A. Hoffman, M. Loose and V. Suntharalingam, "CMOS Detector Technology," *Experimental Astronomy,* vol. 19, no. 1-3, p. 111–134, 29 June 2006.

[100] J. W. Park, Photodiodes - World Activities in 2011; CMOS Photodetectors, InTech, 2011.

[101] B. Razavi, Design of Analog CMOS. Second Edition, New York: McGraw-Hill Education, 2015.

[102] P. R. Gray, P. J. Hurst, S. H. Lewis and R. G. Meyer, Analysis and desing of analog integrated circuits, Wiley, 2009.

[103] "Luxium Solutions," [Online]. Available: https://www.luxiumsolutions.com/radiation-detection-scintillators/plastic-scintillators/bc400-bc404-bc408-bc412-bc416.

[104] "Digital Camera Database," [Online]. Available: www.digicamdb.com/specs/pentax_k-x/.

[105] "Optyczne.pl," [Online]. Available: https://www.optyczne.pl/119.4-Test_aparatu-Pentax_K-x_Rozdzielczo%C5%9B%C4%87.htm.

[106] "Fotopolis.pl," [Online]. Available: www.fotopolis.pl/testy/aparaty/9218-pentax-k-x-test/strona/6.

[107] "Optyczne.pl," [Online]. Available: www.optyczne.pl/119.9-Test_aparatu-Pentax_K-x_Podsumowanie.html.

[108] G. Woźniak and B. Kozłowska, "High resolution 2D plastic scintillator detectors for radiotherapy departments," *Polish Journal of Medical Physics and Engineering*, vol. 29, no. 2, pp. 92-103, 2023.

[109] "Aluxprofile," [Online]. Available: https://www.aluxprofile.pl/profil-aluminiowy-2020-v-slot/a3663.

[110] I. P. Nogueira and P. J. Biggs, "Measurement of TVLs in lead for 4, 6 and 10 MV bremsstrahlung x-ray beams at scattering angles between 30 degrees and 135 degrees," *Health physics*, vol. 83, no. 2, pp. 255-260, 2002.

[111] A. Niroomand-Rad, C. R. Blackwell, B. M. Coursey, K. P. Gall, J. M. Galvin, W. L. McLaughlin, A. S. Meigooni, R. Nath, J. E. Rodgers and C. G. Soares, "Radiochromic film dosimetry: Recommendations of AAPM Radiation Therapy Committee Task Group 55," *Medical Physics*, vol. 25, pp. 2093-2115, 1998.

[112] R. Alfonso, P. Andreo, R. Capote, M. S. Huq, W. Kilby, P. Kjäll, T. Mackie, H. Palmans, K. Rosser, J. Seuntjens, W. Ullrich and S. Vatnitsky, "A new formalism for reference dosimetry of small and nonstandard fields," *Medical Physics*, vol. 35, no. 11, pp. 5179-86, 2008.

[113] A. Micke, D. F. Lewis and X. Yu, "Multichannel film dosimetry with nonuniformity correction," *Medical Physics*, vol. 38, no. 5, pp. 2523-34, 2011.

[114] R. Dąbrowski, I. Drozdyk and P. Kukołowicz, “High accuracy dosimetry with small pieces of Gafchromic films,” *Reports of Practical Oncology & Radiotherapy,* vol. 23, no. 2, pp. 114-120, 2018.

[115] K. M. Holm, E. G. Yukihara, M. F. Ahmed, S. Greilich and O. Jäkel, “Triple channel analysis of Gafchromic EBT3 irradiated with clinical carbon-ion beams,” *Physica Medica,* vol. 87, pp. 123-130, 2021.

[116] “Sun Nuclear,” [Online]. Available: www.sunnuclear.com/products/srs-mapcheck.

[117] Q. Xu, K. Huynh, W. Nie, M. S. Rose, A. K. Chawla, K. S. Choe, S. Kanani, G. J. Kubicek and J. Fan, “Implementing and evaluating a high-resolution diode array for patient-specific quality assurance of robotic brain stereotactic radiosurgery/radiotherapy,” *Journal of applied clinical medical physics,* vol. 23, no. 5, p. e13569, 2022.

[118] A. K. Stedem, M. Tutty, N. Chofor, M. Langhans, C. Kleefeld and A. A. Schönfeld, “Systematic evaluation of spatial resolution and gamma criteria for quality assurance with detector arrays in stereotactic radiosurgery,” *Journal of applied clinical medical physics,* vol. 2, p. 25, 2024.

[119] Z. Yang, L. Yimei, C. Meining, F. Jianlan, X. Liangjie, H. Shaomin, Q. Zhenyu, D. Xiaowu, Z. Jun and P. Yinglin, “Commissioning and clinical evaluation of a novel high-resolution quality assurance digital detector array for SRS and SBRT,” *Journal of Applied Clinical Medical Physics,* vol. 25, no. 4, p. e14258, 2024.

[120] S. Dieterich, C. Cavedon, C. Chuang, A. Cohen, J. Garrett, C. Lee, J. Lowenstein, M. d'Souza, D. Taylor, X. Wu and C. Yu, “Report of AAPM TG 135: Quality assurance for robotic radiosurgery,” *Medical physics,* vol. 38, pp. 2914-36, 2011.

[121] M. F. Triola, Elementary Statistics, Pearson Education, 2006.

[122] “MathWorks,” [Online]. Available: https://www.mathworks.com/.

[123] M. Hollander, D. A. Wolfe and E. Chicken, Nonparametric Statistical Methods, Wiley, 2014.

[124] K. Kubo, H. Monzen, K. Shimomura, K. Matsumoto, T. Sato, M. Tamura, K. Nakamatsu, K. Ishii and R. Kawamoritab, “Comparison of patient-specific intensity modulated radiation therapy quality assurance for the prostate across multiple

institutions," *Reports of practical oncology and radiotherapy,* vol. 24, no. 6, pp. 600-605, 2019.

[125] M. Chan, C. Chin-Cheng, C. Shi, J. Li, X. Tang, X. Li and D. Mah, "Patient-Specific QA of Spot-Scanning Proton Beams Using Radiochromic," *International Journal of Medical Physics, Clinical Engineering and Radiation Oncology,* vol. 6, pp. 111-123, 2017.

[126] M. Saito, N. Sano, Y. Shibata, K. Kuriyama, T. Komiyama, K. Marino, S. Aoki, K. Ashizawa, K. Yoshizawa and H. Onishi, "Comparison of MLC error sensitivity of various commercial devices for VMAT pre-treatment quality assurance," *Journal of Applied Clinical Medical Physics,* vol. 19, no. 3, pp. 87-93, 2018.

[127] E. Spezi and D. G. Lewis, "Gamma histograms for radiotherapy plan evaluation," *Radiotherapy and oncology : journal of the European Society for Therapeutic Radiology and Oncology,* vol. 79, no. 2, pp. 224-230, 2006.

[128] A. Wieczorek, Development of novel plastic scintillators based on polyvinyltoluene for the hybrid J-PET/MR tomograph, Doctoral Dissertation, 2017.

[129] R. D. Evans, The Atomic Nucleus, New York: McGraw-Hill Publishing, 1955.

[130] "Electrical Engineering News and Resources," [Online]. Available: https://www.eeweb.com/radiotherapy/.